Surface structure and dynamics of supercooled polymer melts and metal-polymer nanocomposites

Simone Streit

A thesis submitted to the Department of Physics
in fulfillment of the requirements for the degree of
Doctor of Natural Sciences

Fachbereich Physik
Universität Dortmund

May 2007

Abstract

The focus of this work is the investigation of the surface properties of supercooled liquids and metal-polymer nanocomposites around the glass transition temperature T_G at nanometer length scales. This thesis provides two major contributions in the field of surface sensitive x-ray scattering techniques employed to characterize the behavior of surface fluctuations in polymeric liquids around T_G and the nanoparticle dynamics in out-of-equilibrium systems.

The research topic of the first part of this thesis consists in the determination of the cooling rate dependent freezing of capillary waves on the glass forming liquid poly(propylene glycol) by means of in-situ cooling x-ray reflectivity measurements. The freezing in of density fluctuations while approaching the glass transition has been known in the bulk for a long time, but it has not been determined until now whether an analogous effect also occurs at the free surface. Above T_G the surface roughness σ can be described by the standard capillary wave model for simple liquids, whereas the surface fluctuations are frozen in at temperatures below T_G. As the state of a glass forming liquid strongly depends on its thermal history, for fast cooling rates this effect occurs at higher temperatures than for slow cooling. Large shifts of T_G to 240 K compared to the bulk value of 196 K have been observed. This represents a significant difference to the bulk where the dependence of T_G on the cooling rate is typically weak.

The temporal evolution of gold nanoparticles moving on the surface of thin polystyrene films is investigated in the second part of this work. As the measurements are performed around the glass transition of the polymer, the metal-polymer system is out of equilibrium and therefore exhibits interesting dynamics. The dynamic structure factor $f(q_{||}, \tau)$ of the gold clusters with the lateral wavevector transfer $q_{||}$ and the relaxation time τ is measured with two-dimensional x-ray photon correlation spectroscopy. There is currently extensive interest in bulk soft matter systems where a similar behavior of the dynamic structure factor and aging phenomena are observed. Above the glass transition of the polymer the peculiar modified exponential form $f(q_{||}, \tau) \propto \exp[-(\Gamma\tau)^\alpha]$ is found with $0.7 < \alpha < 1.9$, depending on sample age and temperature. The relaxation rates Γ scale linearly with $q_{||}$, excluding a simple Brownian diffusive motion. This type of behavior, already observed in aging bulk soft matter systems, is explained by a power law distribution of particle velocities due to ballistic motion.

Contents

1 Introduction

The behavior of supercooled liquids around the glass transition is of great importance in nature and technology. The glassy state is essential for the preservation of microorganisms during cold or dehydration [1], which has been copied by industry to protect and preserve drugs or to preserve food [2]. The most prominent example for amorphous materials is window glass. Amorphous materials also occur in most engineering plastics, photovoltaic cells, and optical fibres. Furthermore, it is speculated that most of the water in the universe occurs in a glassy form [3].

Recently, the combination of metal nanoparticles in polymer matrices has gained great technological relevance. There exist manifold applications of metal nanoparticles combined with polymer matrices, as they can be deeply embedded in the polymer or act as a buried interface between different polymer layers [4]. The advantages of polymers like, e.g., simple production, low weight and high ductility can be combined with high strength typical for metals or ceramics by embedding inclusions like fibers or particles into a polymer matrix. Such reinforcements by nanoscale particles also cause new mechanical and viscoelastic properties in the materials which constitutes a current topic of research [4, 5]. An interesting discovery is the similarity of thermomechanical properties between regularly spaced nanoparticles on polymers with thin polymer films due to their confined geometry. The glass transition in such systems seems to be affected by the interaction of near-surface regions with modified mobility compared to the bulk [6].

Surface phenomena investigated in this work are of special interest in fundamental research as well as in industrial applications. Wetting and adhesion effects occur at the surface and play an important role in technical processes like printing, varnishing or bonding. The knowledge and control of the interface structure is crucial in the semiconductor industry. A good example for surface effects in everyday life is the impregnation of raincoats to prevent wetting. On liquid surfaces, thermally excited capillary waves are restored by the surface tension in order to minimize the surface energy. The surface tension allowing water striders to walk on water can be reduced by adding soap or detergent to the water, enabling it to form a mixture with the pollution which can then be easier removed.

The aims and objectives of this thesis are to study the behavior of liquid surfaces around the glass transition at molecular length scales. Within the scope of this work, two different approaches are pursued. One aspect consists in examining how the surface of a polymer melt behaves when the liquid is cooled to the glass transition, with special regards to the freezing in of certain surface wave modes. It has been known in the bulk for a long time that the glass forming process strongly depends on the thermal history. However, the influence of the cooling rate on the glass transition temperature at the surface has not been examined yet and will therefore be discussed in this work. The second major contribution of this thesis is the investigation of the motion of nanometer sized metal clusters on thin polymer films heated up above the glass transition temperature of the polymer. As the samples are prepared out of equilibrium, stress is induced in the polymer matrix which is afterwards released by relaxation processes. Here a matter of particular interest consists in studying aging effects as typical in out-of-equilibrium systems and explaining the nature of the particle motion.

In order to determine the structural and dynamical properties of liquid surfaces x-ray scattering methods are employed within the scope of this work. The advantage of such methods consists on the one hand in the surface sensitivity, but on the other hand in the possibility to characterize buried layers in opaque materials, because depending on the incidence angle the probed depth of the sample can be varied. X-rays can be applied in various complex environments ranging from ultra-high vacuum to gas atmospheres, high pressures and in-situ temperature-variation measurements for monitoring dynamics in real time. Furthermore, specific information about chemical elements can be obtained by anomalous x-ray scattering near absorption edges, and it is possible to probe magnetic properties with polarized x-rays. Moreover, x-rays provide averaged statistical information over the whole sample surface. This inherently obtained ensemble average is essential for the analysis of aging effects, which is very difficult with direct methods, as it is necessary to track several hundred clusters in order to obtain a good average.

In the last decade, due to the high brilliance of third generation synchrotron sources, coherent x-ray scattering has become possible with the novel technique of x-ray photon correlation spectroscopy (XPCS), allowing to examine temporal and lateral correlation properties of liquid surfaces. This topic has been discussed in previous works in our group, e.g., by T. Ghaderi who investigated resolution effects and the influence of partial coherence to explain discrepancies between theoretical predictions and experimental results [7], and by R. Fendt who successfully analyzed different liquids by taking into account a finite experimental resolution [8]. In the present work, the technique of XPCS will be further discussed.

This thesis is structured as follows: The basic principles of the surface sensitive x-ray scattering techniques applied in the experiments are introduced in chapter 2. This includes x-ray reflectivity (section 2.2) which is sensitive to the electron density profile perpendicular to the surface, diffuse scattering measurements (section 2.3) allowing the study of lateral surface effects, and XPCS (section 2.4) which is uniquely suited to investigate slow dynamics of soft matter systems on nanometer length scales.

The analysis of the experimental data concerning the glass transition at surfaces of polymer melts is presented in chapter 3, employing the polymeric liquid poly(propylene glycol) (PPG) as an example for a typical glass former. After a theoretical introduction in section 3.1 on glass transition and capillary waves, a detailed description of the experimental setup is presented in section 3.2. The description and interpretation of the reflectivity measurements used to determine the cooling rate dependent freezing in of capillary waves on the surface of PPG are presented in section 3.3, and the chapter ends with a conclusion.

In chapter 4, the topic of 2D dynamics of nanometer sized gold clusters on the surface of thin polystyrene films is discussed. The method of XPCS enables to measure directly the dispersion relation of the fluctuations of the gold particles on the polymer surface. The theoretical background of polymer properties and aging phenomena is discussed in section 4.1, and the experimental details are described in section 4.2. The static and dynamic measurement results are discussed in section 4.3, and a comparison between low and high gold coverage and polymer weight is drawn. The last section summarizes the results.

The thesis concludes with a summary and an outlook on future research in chapter 5.

2 Surface sensitive x-ray scattering techniques

In this thesis, the experimental techniques of x-ray reflectivity measurements (XRR) and x-ray photon correlation spectroscopy (XPCS) in grazing incident small angle x-ray scattering geometry (GISAXS) were utilized. In the following sections, these techniques will therefore be explained in detail.

2.1 Basic principles and scattering geometry

In x-ray scattering experiments the incident wave with the electric field strength $\vec{E}(\vec{r},t) = \vec{E_0} \cdot \exp[i(\vec{k}\cdot\vec{r}-\omega t)]$ is scattered by a sample characterized by the index of refraction n. $\vec{E_0}$ denotes the amplitude, $\vec{k}$ the wavevector ($|\vec{k}| = \omega/c = 2\pi/\lambda$ with the frequency ω, the speed of light c and the wavelength λ), $\vec{r}$ the position and t the time. In this work only elastic x-ray scattering techniques are used, i.e. the energy $E = \hbar\omega$ remains constant. A wave impinging on a surface is partly reflected and partly transmitted into the medium. In the medium, it propagates according to the Helmholtz equation [9]

$$\vec{\nabla}^2\vec{E}(\vec{r},t) + k^2 n^2(\vec{r})\vec{E}(\vec{r},t) = 0. \tag{2.1}$$

In a medium with N atoms per unit cell, which can be considered as harmonical oscillators with resonance frequencies ω_j, the index of refraction can be written as [9]

$$n^2(\vec{r}) = 1 + N\frac{e^2}{\epsilon_0 m}\sum_{j=1}^{N}\frac{f_j(\vec{q},E)}{\omega_j^2 - \omega^2 - 2i\omega\eta_j}, \tag{2.2}$$

with the elementary charge e, the electron mass m_e, the dielectric coefficient ϵ_0, the forced oscillator strength of the electrons of the j-th atom f_j, and the damping constant η_j of the j-th atom. $f_j(\vec{q},E) = f_j^0(\vec{q}) + f_j'(E) + \mathrm{i}f_j''(E)$ consists of the wavevector dependent atomic form factor $f_j^0(\vec{q})$ - with the wavevector transfer $\vec{q} = \vec{k}_f - \vec{k}_i$ given by the incident ($\vec{k}_i$) and the scattered wave ($\vec{k}_f$) - and the energy dependent dispersion and

absorption corrections $f_j'(E)$ and $f_j''(E)$ [10]. For hard x-rays (1 keV$\lesssim E \lesssim$100 keV) $\omega \gg \omega_j$, and Eq. 2.2 can be replaced by [9, 10]

$$n(\vec{r}) = 1 - \delta(\vec{r}) + \mathrm{i}\beta(\vec{r}) \tag{2.3}$$

with the so-called dispersion

$$\delta(\vec{r}) = \frac{\lambda^2}{2\pi} r_\mathrm{e} \rho(\vec{r}) \sum_{j=1}^{N} \frac{f_j^0 + f_j'(E)}{Z} \tag{2.4}$$

and the absorption

$$\beta(\vec{r}) = \frac{\lambda^2}{2\pi} r_\mathrm{e} \rho(\vec{r}) \sum_{j=1}^{N} \frac{f_j''(E)}{Z}. \tag{2.5}$$

$r_\mathrm{e} = e^2/(4\pi\epsilon_0 m_\mathrm{e} c^2) \approx 2.82 \cdot 10^{-5}$ Å denotes the classical electron radius, $Z = \sum_j Z_j$ the total number of electrons and $\rho(\vec{r})$ the electron density. For small angles f_j^0 can be approximated as $f_j^0 \approx Z_j$. For a homogeneous medium and excitation frequencies of the incident x-ray far away from the resonance frequencies of the inner-shell electrons of the atom, Eqs. 2.4 and 2.5 can be simplified as

$$\delta(\vec{r}) = \frac{\lambda^2}{2\pi} r_\mathrm{e} \rho(\vec{r}) \qquad \text{and} \qquad \beta(\vec{r}) = \frac{\lambda}{4\pi} \mu(\vec{r}), \tag{2.6}$$

with the linear absorption coefficient $\mu(\vec{r})$. Contrary to visible light, the dispersion for x-rays is positive in a medium and on the order of 10^{-6} for most materials investigated in this work. Hence, for x-rays hitting a sample from vacuum or air, the sample represents the optical thinner medium, thus allowing for total external reflection if the incident wave impinges underneath a critical angle of total external reflection α_c. Table 2.1 shows δ, β, $\alpha_\mathrm{c} \approx \sqrt{2\delta}$ and the penetration depth Λ as a function of the x-ray energy for the materials investigated in this work (the data are taken from [11]). Λ is defined as the 1/e decrease of the incoming intensity and can be approximated below α_c as $\Lambda \approx \lambda/(2\pi\alpha_\mathrm{c}) = (4\pi r_\mathrm{e}\rho)^{-1/2}$ [12]. In the case of total external reflection the x-rays only penetrate several nm into the material. X-ray measurements under grazing incidence are therefore well suited for the investigation of surface phenomena.

The scattering geometry for x-rays is depicted in Fig. 2.1. A plane electromagnetic wave impinges onto the sample surface at the incidence angle α_i and is scattered at the angles α_f in the plane of incidence and ϕ out of the plane of incidence. The plane of incidence is defined by a plane perpendicular to the sample surface including the incident beam. A part of the wave is refracted into the material at the angle α_t. With $n = 1$ in

Material	E [keV] (λ [Å])	$\delta\,[10^{-6}]$	$\beta\,[10^{-8}]$	α_c [°]	Λ [nm]
gold	8.048 (1.54)	47.15	485.5	0.556	2.53
(Au)	10.64 (1.16)	26.12	176.5	0.414	2.55
silicon	8.048 (1.54)	7.58	17.31	0.223	6.29
(Si)	10.64 (1.16)	4.31	5.78	0.168	6.29
quartz	8.048 (1.54)	6.8 - 7.4	8.8 - 9.6	0.21 - 0.22	6.4 - 6.7
(SiO_2)	10.64 (1.16)	3.9 - 4.2	2.9 - 3.2	0.16 - 0.17	6.3 - 6.6
PPG-400	8.048 (1.54)	3.58	0.737	0.153	9.16
($C_{21}H_{44}O_8$)	8.000 (1.55)	3.62	0.755	0.154	9.16
polystyrene	8.048 (1.54)	3.49	0.495	0.151	9.28
(C_8H_8)	10.64 (1.16)	1.99	0.160	0.114	9.24

Table 2.1: Dispersion δ, absorption β, critical angle α_c and penetration depth Λ for several materials at room temperature and different photon energies. PPG-400 stands for poly(propylene glycol) with a molecular weight of 400 g/mol.

vacuum and $n < 1$ in the medium the critical angle of total external reflection ($\alpha_t = 0$) can be approximated for small angles as $\alpha_c \approx \sqrt{2\delta}$ from the Snellius law

$$\cos\alpha_i = n\cos\alpha_t. \tag{2.7}$$

The scattered intensity is expressed as a function of the wavevector transfer $\vec{q} = \vec{k}_f - \vec{k}_i$ with $|\vec{k}_i| = |\vec{k}_f| = 2\pi/\lambda$ which is calculated according to Fig. 2.1 as follows:

$$\vec{q} = \begin{pmatrix} q_x \\ q_y \\ q_z \end{pmatrix} = |\vec{k}_i| \begin{pmatrix} \cos\alpha_f\cos\phi - \cos\alpha_i \\ \cos\alpha_f\sin\phi \\ \sin\alpha_i + \sin\alpha_f \end{pmatrix}. \tag{2.8}$$

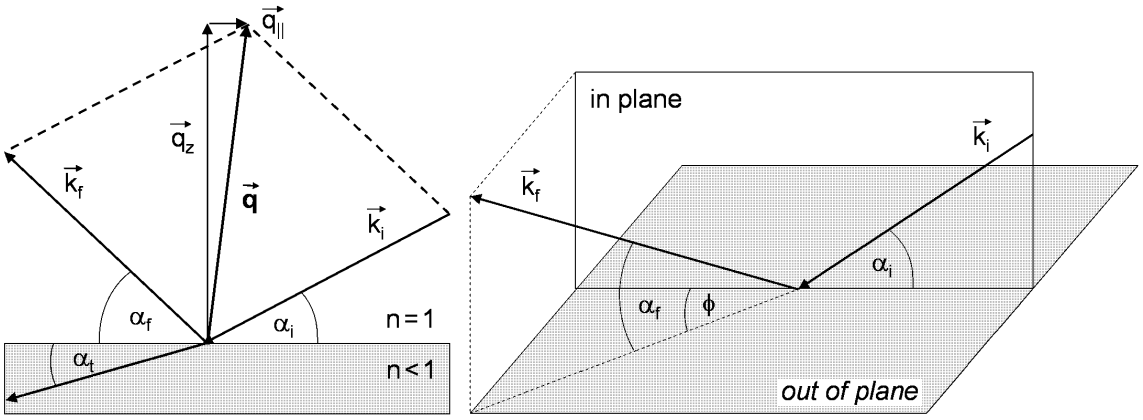

Figure 2.1: Scattering geometry for x-ray measurements.

In the special case of x-ray reflectivity measurements, $\alpha_i = \alpha_f$ and $\phi = 0$, therefore $q_{||} = (q_x^2 + q_y^2)^{1/2} = 0$ and $q_z = 4\pi/\lambda \cdot \sin\alpha_i$. Another specific case are out-of-plane scans under grazing incidence and exit, i.e., $\alpha_i \approx \alpha_f \approx 0$ and $\phi \neq 0$. Here $q_x = 2\pi/\lambda \cdot (\cos\phi - 1)$, $q_y = 2\pi/\lambda \cdot \sin\phi$, and $q_z = 0$. Therefore, reflectivity scans provide information about the electron density profile perpendicular to the surface, whereas grazing incidence and exit scans out of plane yield information about the lateral structure of the sample.

2.2 X-ray reflectivity measurements

In this section, the basic equations for x-ray scattering in specular geometry as used in optics will be derived. In the subsequent section, x-ray scattering will be treated in a more general form of scattering cross sections.

2.2.1 Scattering from smooth surfaces

The reflectivity of an ideal smooth surface can be expressed in terms of the Fresnel coefficients [13]. The amplitudes of the reflected and transmitted waves are $|\vec{E}_{0,r}| = r \cdot |\vec{E}_{0,i}|$ and $|\vec{E}_{0,t}| = t \cdot |\vec{E}_{0,i}|$, respectively, with the amplitude $|\vec{E}_{0,i}|$ of the incident wave. The reflection and transmission coefficients

$$r = \frac{k_{i,z} - k_{t,z}}{k_{i,z} + k_{t,z}} \quad \text{and} \quad t = \frac{2k_{i,z}}{k_{i,z} + k_{t,z}} \tag{2.9}$$

are obtained from the condition that the electromagnetic fields have to be continuous at the interface. $k_{i,z} = k\sin\alpha_i$ and $k_{t,z} = nk\sin\alpha_t = k(n^2 - \cos^2\alpha_i)^{1/2}$ denote the z components of the incident and transmitted wavevectors. The Fresnel coefficients depend on the polarization by a factor of n^2 for s and p polarization. With $n \approx 1$ for x-rays, this dependence can be neglected. For small angles the Fresnel reflectivity of a smooth surface is calculated by [9]

$$R_F = |r|^2 = \frac{(\alpha_i - p_+)^2 + p_-^2}{(\alpha_i + p_+)^2 + p_-^2} \tag{2.10}$$

with the real and imaginary part of the transmission angle $\alpha_t = p_+ + ip_-$

$$p_{+/-}^2 = \frac{1}{2}\left[\sqrt{(\alpha_i^2 - \alpha_c^2)^2 + 4\beta^2} \pm (\alpha_i^2 - \alpha_c^2)\right]. \tag{2.11}$$

For $\alpha_i > 3\alpha_c$ Eq. 2.10 can be approximated as $R_F \approx (\alpha_c/(2\alpha_i))^4$. Inserting Eq. 2.3 into Eq. 2.7, for small angles (i.e. $\cos\alpha \approx 1 - \alpha^2/2$) the transmission angle can be approximated as

$$\alpha_t^2 \approx \alpha_i^2 - 2\delta + 2i\beta. \tag{2.12}$$

Thus, for $\beta = 0$, α_t becomes zero for $\alpha_i = \alpha_c$, and it becomes complex for $\alpha_i < \alpha_c$. Therefore, even without absorption, the transmitted wave perpendicular to the surface $E_t(z) = E_{0,t}\exp(ik_t z) \approx E_{0,t}\exp(ink\alpha_t z)$ is damped exponentially. The penetration depth of the transmitted wave Λ (which is listed in Tab. 2.1 for small angles below α_c) is defined as $\Lambda = 1/(kp_-)$ [9]. Taking a finite absorption into account ensures that Λ is limited for $\alpha_i > \alpha_c$. The maximal value $\Lambda_{max} = \lambda/(4\beta)$ is in the micrometer region for most materials for perpendicular incidence at 8 keV [9].

The Fresnel transmission can be approximated for small angles by

$$T_F = |t|^2 = \frac{4\alpha_i^2}{2p_+(p_+ + \alpha_i) + \alpha_c^2}. \tag{2.13}$$

For $\alpha_i = \alpha_c$ one obtains the expression $T_F = 4\alpha_i^2/[(\alpha_i + \sqrt{\beta})^2 + \beta]$, therefore the maximal value of T_F is four when the absorption is neglected. In Fig. 2.2 the Fresnel reflectivity and transmission for an ideally smooth PPG-400 surface are shown. The values for δ and β are taken from Tab. 2.1. Below α_c the reflected intensity is equal to one, then it decreases fast with α_i^4. As the ratio of $\beta/\delta \approx 0.002$ is very small for PPG, the maximum of the transmission function is well pronounced. For a larger absorption like e.g., in gold, the peak would be more damped. For larger angles than α_c the transmission function decreases to the constant value of one. The angular dependence of T_F is the origin of maxima in the scattered intensity, in a surface scattering experiment the so-called Yoneda peaks [14].

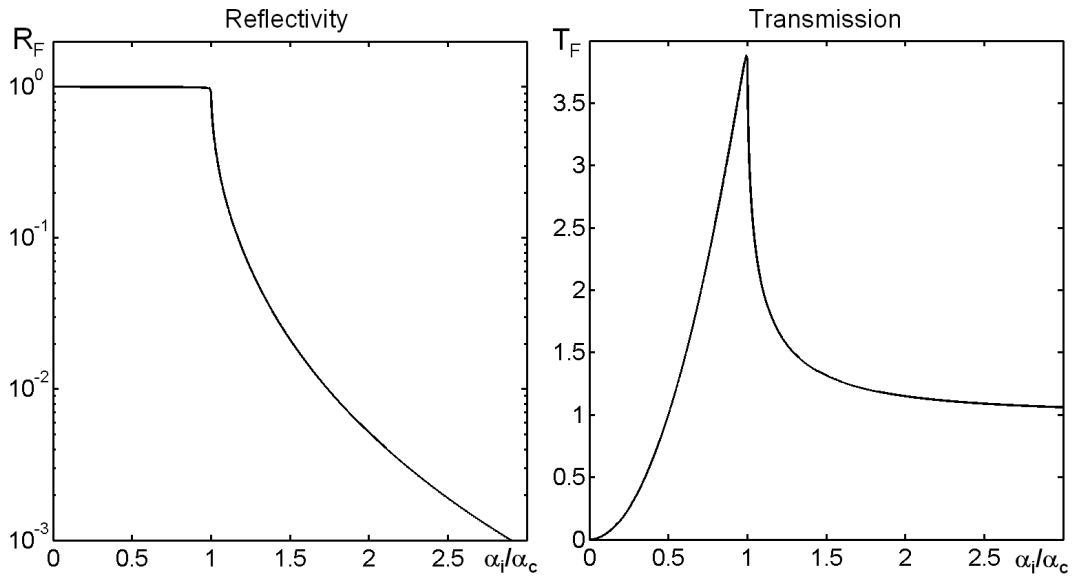

Figure 2.2: Fresnel reflectivity and transmission calculated for PPG-400 for 8.048 keV. The incident angle α_i is normalized by the critical angle α_c.

2.2.2 Scattering from multiple layers

Until now, only scattering from a single surface has been considered. However, more complex (real) systems typically consist of several layers contributing to the scattering signal. Thus, multiple layer systems will be discussed in the following.

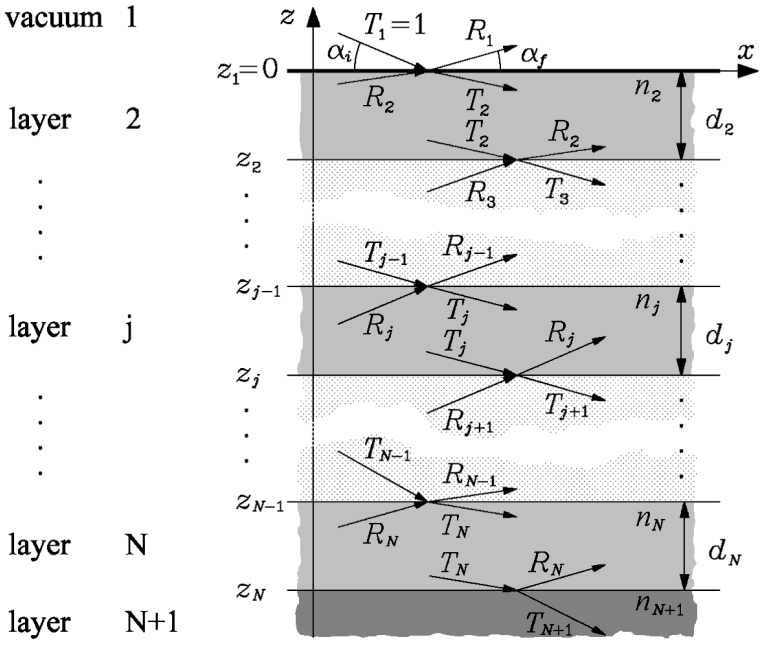

Figure 2.3: System of multiple layers with different indices of refraction. For each interface the amplitudes of the transmitted and reflected beams are plotted [9].

Fig. 2.3 is a schematical representation of a sample consisting of several smooth layers with different indices of refraction n and thicknesses d separated by N interfaces. The vacuum and the substrate (layer $N+1$) are assumed to be of infinite thickness. The amplitude R_1 of the reflected wave from the top layer can be calculated if one considers that according to Maxwell's theory the tangential components of the electrical and magnetic field vectors $\vec{E}$ and $\vec{H}$ have to be continuous at the interfaces. Hence, the reflected intensities of all interfaces have to be summed up considering the appropriate phases. This problem was first treated by Abelès who introduced transfer matrices for each layer [15]. Nowadays in most applications the recursive Parratt algorithm is used which is simple to implement [16]. For the analysis of the reflectivities in this work the fitting routine LSFIT is used [17] which is based on the Parratt algorithm.

In Fig. 2.4 an example for a multilayer system can be seen, consisting of a polystyrene film on top of a silicon substrate, decorated with gold clusters. One can clearly distinguish the critical angles of the different materials as shown in the inset. For larger angles

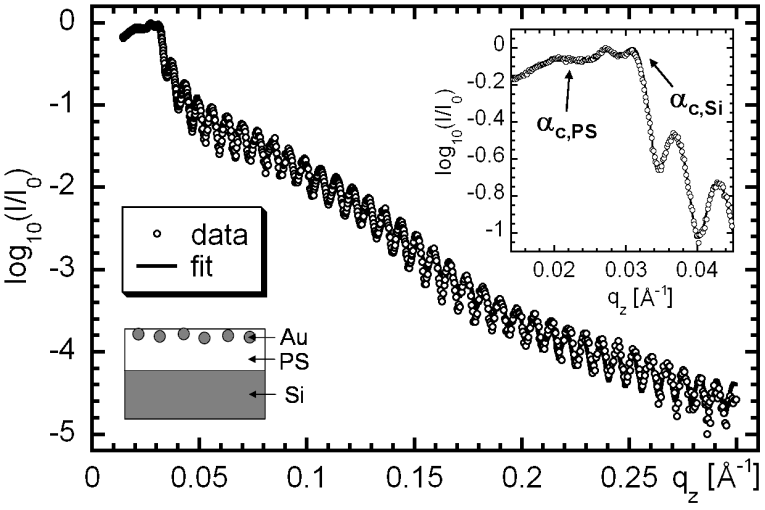

Figure 2.4: Reflectivity from an 800 Å polystyrene (PS) film on a silicon substrate, decorated with a gold layer of 8 Å nominal thickness. The inset on the right shows the increased region around the critical angle of total external reflection. At the bottom, the investigated sample system is sketched.

of incidence the reflected intensity decreases according to α_i^{-4}. This decrease is superposed by oscillations, the so-called Kiessig fringes [18] which are created by interference from the x-rays reflected from the top and bottom interface of a layer. According to $d = 2\pi/\Delta q_z$ with the distance Δq_z between two maxima the period of the oscillations is inversely proportional to the layer thickness d. In Fig. 2.4 the short-period oscillations are due to the interference of the reflected x-rays from the silicon substrate and the polystyrene layer. One can also observe a long-period superimposed oscillation with a minimum at around 0.19 Å^{-1} which is caused by the thin gold layer on top of the polymer film. Reflectivity measurements are therefore well suited to measure layer thicknesses. Moreover, the roughness of each layer can be determined as will be shown in the next subsection.

2.2.3 Influence of the roughness

Real surfaces are never perfectly smooth. Fig. 2.5 shows that for q_z smaller than 0.15 Å^{-1} a good correlation between the model and the experiment is obtained, but for larger q_z values or after about five orders of magnitude of the intensity deviations between the reflected intensity from a water surface and the Fresnel reflectivity occur. Due to the roughness σ the measured intensity is lower. As the scattering amplitude is proportional to the Fourier transform of the electron density, the formula for the reflected intensity

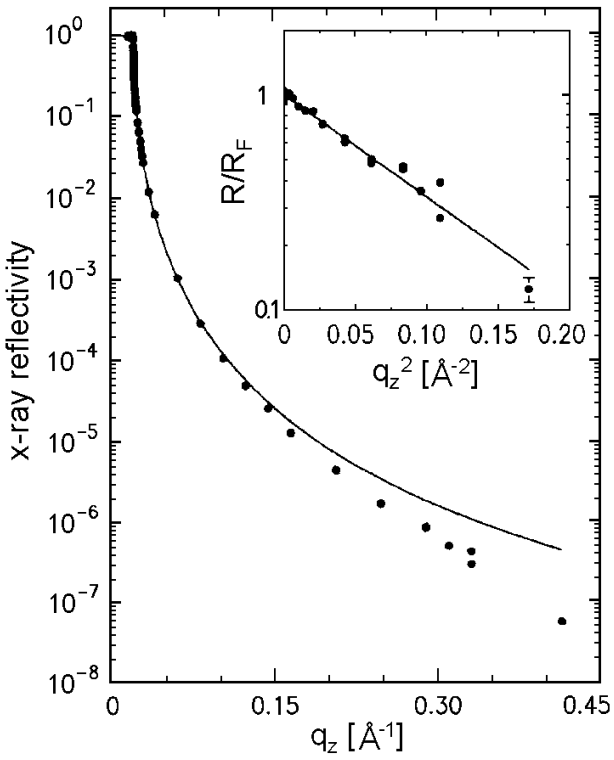

Figure 2.5: Reflectivity from a water surface [19]. The normalized intensity is plotted as a function of the wavevector transfer perpendicular to the surface q_z. The solid line is the calculated Fresnel reflectivity for an ideally smooth surface. The inset shows the same data in a logarithmic plot of R/R_{F} as a function of q_z^2, and the slope of the line is equal to $-\sigma^2$.

from a rough interface is given by [9, 10]

$$\frac{R(q_z)}{R_{\mathrm{F}}(q_z)} = \left| \frac{1}{\rho_\infty} \int_0^\infty \left(\frac{d\rho(z)}{dz} \right) e^{iq_z z} dz \right|^2 , \tag{2.14}$$

where $\rho(z)$ denotes the electron density profile as a function of the height z perpendicular to the surface and ρ_∞ is the average density of the entire sample. Therefore, the ratio between the measured reflectivity and the Fresnel reflectivity for an ideally smooth surface is given by the absolute square of the Fourier transform of the electron density gradient. The electron density is often expressed by an error function $\rho(z) = \mathrm{erf}(z/(\sqrt{2}\sigma))$[1] where σ describes the width of the roughness region as shown in Fig. 2.6. As the derivative of the error function is a Gaussian

$$\frac{d\rho(z)}{dz} = \frac{1}{\sqrt{2\pi}\sigma} \exp\left(-\frac{z^2}{2\sigma^2} \right) , \tag{2.15}$$

[1]The error function is defined as $\mathrm{erf}(x) = \frac{2}{\sqrt{\pi}} \int_0^x \exp(-t^2)\, dt$.

and the Fourier transform of a Gaussian is another Gaussian, the reflected intensity can be expressed with a Debye-Waller like roughness term

$$R(q_z) = R_{\mathrm{F}}(q_z)\exp(-\sigma^2 q_z^2). \tag{2.16}$$

Contrary to an ideally smooth interface where the index of refraction n changes according to a step function but remains constant within a layer, for a rough interface n seems to change continuously and does not only depend on the height z anymore, but also on the lateral distances x and y of the interface. Hence, $z = z(x, y)$, and the averaging over the sample surface in x-ray reflectivity measurements yields the impression of a continuous change. This is due to the fact that for reflectivity measurements only a component of the wavevector transfer perpendicular to the surface q_z exists, and because of the large footprint of the beam on the sample all contributions from the x and y directions are summed up. The footprint is defined as the illuminated area by the beam on the sample.

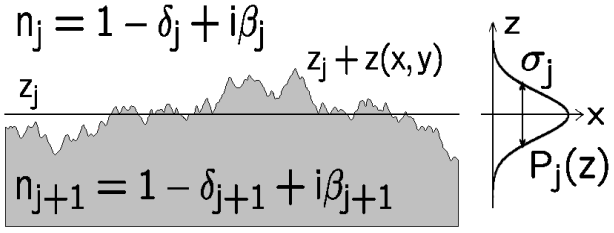

Figure 2.6: Sketch of a rough interface with a probability distribution $P_j(z)$ for the position of the j-th interface [9].

Fig. 2.6 shows a rough interface with the mean height z_j positioned between the j-th layer with the index of refraction n_j and the $(j+1)$-th layer with n_{j+1}. One can divide the transition from the layer j to the next layer $j+1$ into several thin smooth layers, positioned at the corresponding coordinates z_j and weighted with the probability function $P_j(z')$. Adding z_j to the relative layer coordinates z' yields the absolute z values $z = z_j + z'$. With the probability $P_j(z')\,dz'$ to find the interface j in the interval $[z_j + z', z_j + z' + dz']$ and the mean value $\int z' P_j(z')\,dz' = 0$ the root-mean-square (rms) roughness of the j-th layer is defined as

$$\sigma_j^2 = \int z'^2 P_j(z')\,dz'. \tag{2.17}$$

The continuous index of refraction n is then expressed as

$$n_j(z') = \int_{-\infty}^{\infty} \left[n_j + (n_{j+1} - n_j)\Theta(z' - \zeta)\right] P_j(\zeta)\,d\zeta \tag{2.18}$$

$$= n_j + (n_{j+1} - n_j)\int_{-\infty}^{z'} P_j(\zeta)\,d\zeta, \tag{2.19}$$

where Θ denotes the Heavyside step function. This ansatz yields modified Fresnel coefficients which allow to calculate the layer system as if it consisted of smooth interfaces [9]:

$$\tilde{r}_{j+1,j} = \frac{f_j(k_{z,j+1}+k_{z,j})}{f_j(k_{z,j+1}-k_{z,j})} r_{j+1,j} \tag{2.20}$$

$$\tilde{t}_{j+1,j} = \frac{1}{f_j(k_{z,j+1}-k_{z,j})} t_{j+1,j} \tag{2.21}$$

$$\text{with } f_j(k) = \exp(ik\mu_j) \int \exp(-ikz) P_j(z)\, dz, \tag{2.22}$$

where $r_{j+1,j}$ and $t_{j+1,j}$ denote the Fresnel coefficients of a smooth interface between the j-th and $(j+1)$-th layer as calculated in Eq. 2.9. $\mu_j = \int z P_j(z)\, dz$ denotes the mean value of the probability density $P_j(z)$ as depicted in Fig. 2.6. Assuming the following profile for the index of refraction

$$n_j^{\text{erf}}(z) = \frac{n_j + n_{j+1}}{2} - \frac{n_j - n_{j+1}}{2} \operatorname{erf}\left(\frac{z-z_j}{\sqrt{2}\sigma_j}\right), \tag{2.23}$$

one obtains a Gaussian profile for $P_j(z)$:

$$P_j^{\text{erf}}(z) = \frac{1}{\sqrt{2\pi}\sigma_j} \exp\left(-\frac{z^2}{2\sigma_j^2}\right). \tag{2.24}$$

The modified Fresnel coefficients are then given by

$$\tilde{r}_{j+1,j}^{\text{erf}} = \exp(-2k_{z,j}k_{z,j+1}\sigma_j^2)\, r_{j+1,j} \tag{2.25}$$

$$\text{and } \tilde{t}_{j+1,j}^{\text{erf}} = \exp\left[\frac{(k_{z,j}-k_{z,j+1})^2\sigma_j^2}{2}\right] t_{j+1,j}. \tag{2.26}$$

Another profile for the index of refraction also often used in literature is the tanh-profile, but the differences to the erf-profile are less than 5%. However, it should be mentioned here because the reflectivities presented in chapter 3 are fitted with a tanh-profile. The accordant results are then as follows:

$$n_j^{\tanh}(z) = \frac{n_j + n_{j+1}}{2} - \frac{n_j - n_{j+1}}{2} \tanh\left(\frac{\pi}{2\sqrt{3}} \cdot \frac{z-z_j}{\sigma_j}\right) \tag{2.27}$$

$$P_j^{\tanh}(z) = \frac{\pi}{4\sqrt{3}\sigma_j} \cosh^{-2}\left(\frac{\pi}{2\sqrt{3}} \cdot \frac{z}{\sigma_j}\right) \tag{2.28}$$

$$\tilde{r}_{j+1,j}^{\tanh} = \frac{\sinh[\sqrt{3}\sigma_j(k_{z,j}-k_{z,j+1})]}{\sinh[\sqrt{3}\sigma_j(k_{z,j}+k_{z,j+1})]}\, r_{j+1,j} \tag{2.29}$$

$$\tilde{t}_{j+1,j}^{\tanh} = \frac{\sinh[\sqrt{3}\sigma_j(k_{z,j}-k_{z,j+1})]}{\sqrt{3}\sigma_j(k_{z,j}-k_{z,j+1})}\, t_{j+1,j}. \tag{2.30}$$

2.3 Diffuse scattering from liquid surfaces

Contrary to specular reflectivity measurements which are sensitive to the vertical electron density profile, in this section diffuse scattered x-rays will be treated, which provide information about the lateral surface structure.

2.3.1 Scattering in the Born approximation

Although the relations obtained from Fresnel optics in the previous section are quite simple and of great practical value, e.g., for calculating the reflectivity with the Parratt formalism, x-ray scattering is more clearly treated by another description which allows to draw more general conclusions: Usually the measured intensity in an x-ray scattering experiment is described within the kinematical or (first order) Born approximation. This approach is valid for the scattering regime where only single scattering events have to be taken into account. Therefore, the Born approximation can be used for incident angles larger than the critical angle of total external reflection (except for the regions around Bragg peaks) where the intensity decreases so fast that multiple scattering events can be neglected. The scattering amplitude $A(\vec{q})$ which is proportional to the Fourier transform of the three dimensional electron density $\rho(\vec{r})$ of the scatterer can then be expressed as a volume integral [10]:

$$A(\vec{q}) = -r_{\mathrm{e}} \int_V \rho(\vec{r}) e^{i\vec{q}\cdot\vec{r}} d^3r \tag{2.31}$$

with the classical electron radius r_{e}, the volume V, the number of electrons $\rho(\vec{r})d^3r$ in a volume element located at the position $\vec{r}$ and the phase factor $\exp(i\vec{q}\cdot\vec{r})$.

In the following, the diffuse scattering is described for the special case of liquid surfaces. The surface or interface is hereby described by a statistical distribution. The following simplifications will be considered: (*i*) The electron density is constant above and below the rough interface, respectively. (*ii*) The x-rays are damped exponentially with increasing depth in the material. (*iii*) The surface fluctuations only consist of a vertical motion of the particles (the lateral motion is neglected) and are described by a height-height correlation function $C(\vec{r})$. However, these approximations are not valid anymore for diffuse scattering at large wavevector transfers [20].

With the theorem of Gauss, the volume integral in Eq. 2.31 can be transformed into a surface integral. Normally the entire surface surrounding the volume is needed, but in this case there are no scattering contributions from the lower interface due to absorption. Hence, the scattering amplitude becomes [10]

$$A(\vec{q}) = -r_0 \Delta\rho \frac{1}{iq_z} \int_S e^{i\vec{q}\cdot\vec{r}} d^2r, \tag{2.32}$$

where S denotes the illuminated surface and $\Delta\rho$ the electron density contrast at the interface between two media. Therefore, only a mathematical description of the surface is needed, whereas other layers beneath the surface do not contribute to the integral. The differential scattering cross section which describes the scattered intensity per solid angle $d\Omega$ is defined as the absolute square of the scattering amplitude:

$$\frac{d\sigma}{d\Omega} = \left(\frac{r_0\Delta\rho}{q_z}\right)^2 \iint \exp[i\vec{q}\cdot(\vec{r}-\vec{r}')]\, d^2r\, d^2r' \tag{2.33}$$

with $\vec{q}\cdot(\vec{r}-\vec{r}') = q_x x + q_y y + q_z(h(x,y)-h(x',y'))$. With the assumption that the height difference $h(x,y) - h(x',y')$ only depends on the relative difference in the positions $(x-x', y-y')$, this integral can then be expressed as a product of two two-dimensional integrals:

$$\frac{d\sigma}{d\Omega} = \left(\frac{r_0\Delta\rho}{q_z}\right)^2 \int dx'\, dy' \int \langle \exp[iq_z(h(0,0)-h(x,y))]\rangle \exp[i(q_x x + q_y y)]\, dx\, dy. \tag{2.34}$$

The brackets $\langle\rangle$ describe an ensemble average: For a fixed position (x', y') the average is calculated for all possible origins within the illuminated surface area $\int dx'\, dy' = A_0/\sin\alpha_i$. Under the assumption that the height variations are subject to Gaussian statistics, the Baker-Hausdorff theorem can be applied [10]:

$$\langle \exp[iq_z(h(0,0)-h(x,y))]\rangle = \exp[-q_z^2 \left\langle [h(0,0)-h(x,y)]^2 \right\rangle /2], \tag{2.35}$$

where $\langle [h(0,0)-h(x,y)]^2\rangle$ describes the ensemble average of the height differences. According to Sinha et al., the surface can be described by a height-height correlation function $C(\vec{r})$, and the scattering cross section can be expressed as [21]

$$\frac{d\sigma}{d\Omega} = \left(\frac{r_0\Delta\rho}{q_z}\right)^2 \frac{A_0}{\sin\alpha_i} e^{-q_z^2\sigma^2} \int \exp[C(\vec{r})q_z^2] \exp[i(q_x x + q_y y)]\, dx\, dy. \tag{2.36}$$

With $\eta = q_z^2\sigma^2/2$, $q_{||} = (q_x^2 + q_y^2)^{1/2}$ and the Gamma function $\Gamma(x)$[2] the scattering cross section is then be given by [21]

$$\frac{d\sigma}{d\Omega} = \left(\frac{r_0\Delta\rho}{q_z}\right)^2 \frac{A_0}{\sin\alpha_i}\, 2\pi e^{-q_z^2\sigma^2} \cdot 2^{1-\eta} q_{||}^{\eta-2} \frac{\Gamma(1-\eta/2)}{\Gamma(\eta/2)}. \tag{2.37}$$

For small η the scattered intensity as a function of the lateral wavevector transfer is given by $I(q_{||}) \propto 1/q_{||}^2$.

[2]The Gamma function is defined as $\Gamma(x) = \int_0^\infty t^{x-1}e^{-t}dt$ [23].

As $C(r)$ only describes the height-height correlations due to capillary waves at the surface, another contribution due to bulk scattering has to be added to the scattering cross section. It mainly depends on the penetration depth and is given by [24]

$$\left(\frac{d\sigma}{d\Omega}\right)_{\text{bulk}} \propto \frac{k_{\text{B}}T\kappa_T}{2\Im(q_z^t)}. \tag{2.38}$$

κ_T denotes the isothermal compressibility and $\Im(q_z^t)$ is the imaginary part of the vertical component of the transmitted wavevector transfer $q_z^t = k_{t,z} + k_{t,z,f} = k(n^2 - \cos^2\alpha_i)^{1/2} + k(n^2 - \cos^2\alpha_f)^{1/2}$ in the liquid determining the effective penetration depth of the x-rays.

Additional intensity maxima, so-called structure peaks, can occur if the wavevector transfer is equal to typical inverse length scales $q = 2\pi/r$ in the liquid, e.g., if r corresponds to the mean distance between molecules. To take the position and form of a structure peak into account, the electron density distribution has to be known, which can be derived from separate measurements of the bulk structure peak.

2.3.2 Distorted-Wave Born Approximation

As mentioned in the beginning of this section, the kinematical approximation is only valid if multiple scattering can be neglected. Hence, for small incident and exit angles the distorted-wave Born approximation (DWBA) has to be taken into account [25, 21]. In the first step of the DWBA, the scattering sample is replaced by a more simple electron distribution describing a homogeneous surface, and the field caused by an incident plane wave is calculated exactly. In a second step, the illumination of the real scatterer - taking into account the inhomogeneities in the electron density distribution - with this so-called distorted-wave field is considered. The interaction of the first wave field with the distorted-wave field describes the true scattering in a better way than the first order Born approximation [25]. The DWBA will not be discussed in detail here. The changes for the calculation of the scattering cross section due to the DWBA consist in two additional terms that have to be multiplied in Eq. 2.37, namely the transmission functions of the incident and exit beams, $\tilde{t}(\alpha_i) = 2k_{i,z}/(k_{i,z} + k_{t,z})$ and $\tilde{t}(\alpha_f) = 2k_{f,z}/(k_{f,z} + k_{t,z,f})$, respectively. Furthermore, q_z is replaced by the wavevector transfer in the medium q_z^t. The differential scattering cross section can then be summarized in the following form:

$$\frac{d\sigma}{d\Omega} = \left(|\tilde{t}(\alpha_i)||\tilde{t}(\alpha_f)|\frac{r_0\Delta\rho}{q_z^t}\right)^2 \frac{A_0}{\sin\alpha_i}\left[2\pi e^{-q_z^2\sigma^2}2^{1-\eta}q_{||}^{\eta-2}\frac{\Gamma(1-\eta/2)}{\Gamma(\eta/2)} + \frac{k_{\text{B}}T\kappa_T}{2\Im(q_z^t)}\right]. \tag{2.39}$$

2.4 Scattering with coherent x-rays

In this section, coherent scattering techniques with x-rays will be discussed. The main advantage of using coherent or partially coherent radiation consists in the fact that phase information is not lost as for normally used incoherent radiation. Therefore, a so-called speckle pattern can be measured which is directly sensitive to spatial or temporal changes in the electron configuration of the sample.

2.4.1 Basic features of coherent scattering

Two wavefronts are coherent when their phase difference is temporarily constant, allowing for constructive or destructive interference. A coherence time can then be defined as the maximal time interval during which the phase differences between all waves interfering at a certain point in space differ less than 2π. Analogous, a wave field is spatially coherent if the phase difference of any partial wave changes less than 2π during a certain observation period. Interference effects can only be observed within the coherence volume given by the longitudinal and transverse coherence lengths.

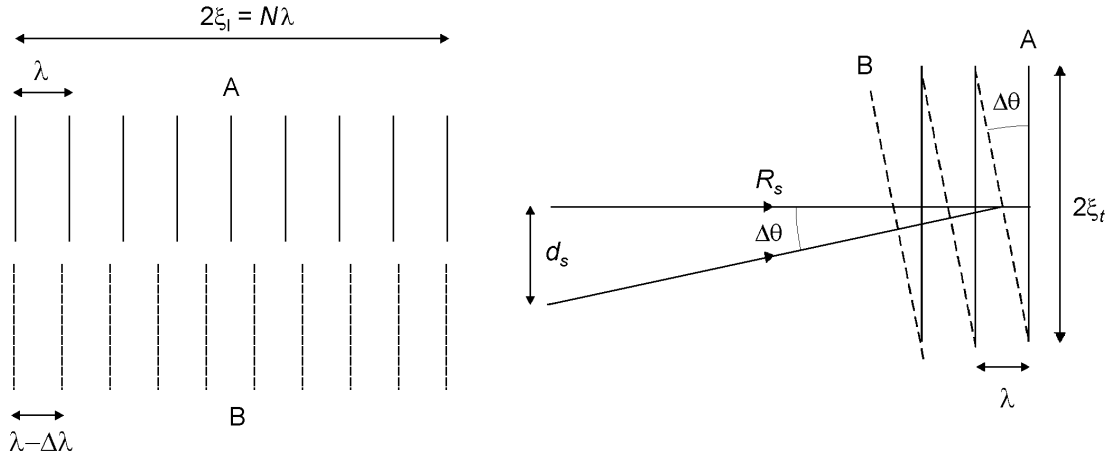

Figure 2.7: Longitudinal (left) and transverse coherence lengths (right). The slightly modified images are taken from [10].

A real x-ray beam deviates from a perfect plane wave, because it is not completely monochromatic and does not propagate in one perfectly well defined direction. This is due to the fact that each radiation source has a finite size and energy bandwidth, so that the sample is illuminated by many slightly different waves. Hence, a real beam can be described by coherence lengths as illustrated in Fig. 2.7. In the left part of the figure, two plane waves A and B with slightly different wavelengths λ and $\lambda - \Delta\lambda$, respectively, propagate in the same direction. After having traveled the longitudinal (or temporal)

coherence length ξ_l, they are completely out of phase, and in phase again after $2\xi_\mathrm{l}$. The second distance is equal to N wavelengths or $N+1$ wavelengths minus $\Delta\lambda$, therefore $\lambda = (N+1)\Delta\lambda \approx N\Delta\lambda$, and the longitudinal coherence length ξ_l follows as [10]

$$\xi_\mathrm{l} = \frac{\lambda}{2} \cdot \frac{\lambda}{\Delta\lambda}. \tag{2.40}$$

The right part of Fig. 2.7 shows the transverse (or spatial) coherence length ξ_t which is caused by two waves A and B with the same wavelength, but slightly different directions of propagation due to a finite source size d_s at a distance R_s from the sample. Again, the waves are completely out of phase after a distance ξ_t perpendicular to the direction of propagation, and in phase again after $2\xi_\mathrm{t}$. With the difference $\Delta\theta = D/R = \lambda/2\xi_\mathrm{t}$ between the directions of propagation, the transverse coherence length can be calculated as [10]

$$\xi_\mathrm{t} = \frac{\lambda}{2} \cdot \frac{R_\mathrm{s}}{d_\mathrm{s}}. \tag{2.41}$$

At the beamline ID10A of the European Synchrotron Radiation Facility (ESRF) typical values for the longitudinal and transverse coherence lengths at 8 keV are $\xi_\mathrm{l} \approx 1\mu$m and $\xi_\mathrm{t} \approx 10\mu$m. To resolve speckles, i.e. the graininess exhibited by reflected light from a (partially) coherent radiation source, the path difference of the beams scattered by different positions in the sample has to be smaller than ξ_l, and the incident beam size has to be smaller than ξ_t.

The coherent flux F_c at the sample depends on the bandwidth $\Delta\lambda/\lambda \approx 10^{-4}$ for the beamline ID10A which is a function of the monochromator bandpass, the wavelength λ and the brilliance B which is defined as the photon flux per area, per solid angle and per wavelength interval of 0.1%. B is typically given in units of photons per (s $\cdot$ 0.1% bandwidth $\cdot$ mm^2 $\cdot$ mrad^2). F_c can be calculated as [26]

$$F_\mathrm{c} = B \cdot \lambda^2 \cdot \frac{\Delta\lambda}{\lambda}, \tag{2.42}$$

so the coherent flux is mainly determined by the brilliance of the source. At the ESRF F_c is around 10^9 photons/s. The number of photons per coherence volume is then given by [27]

$$n_\mathrm{c} = F_\mathrm{c} \cdot \frac{\xi_\mathrm{l}}{c} = B \cdot \frac{\lambda^3}{2c}. \tag{2.43}$$

Due to the dependence on λ^3, compared to laser light scattering, coherent scattering experiments become much more difficult for small wavelengths typical for x-rays.

2.4.2 Effects of partial coherence

For illumination of a sample with visible laser light - where normally nearly complete coherence is available - the Fraunhofer limit is valid so that plane waves in the far field can be considered and large coherence lengths exist. This is generally not the case for x-rays, where the Fraunhofer limit is not necessarily satisfied - only partial coherence occurs - and the coherence lengths are smaller or equal to the illuminated sample size. Partial coherence can be produced for x-rays by positioning a pinhole in front of the sample which cuts out a more or less coherent part of the incoming beam.

According to Ref. [28] the Fraunhofer scattering regime can only be assumed if the Fresnel number F with the pinhole diameter a, the distance L between sample and detector and the wavelength λ is much smaller than unity:

$$F = \frac{a^2}{L\lambda} \ll 1. \tag{2.44}$$

However, for a typical x-ray setup with a photon energy of 10.64 keV, $a = 20$ μm, $L = 1.3$ m and $\lambda = 1.16$ Å (values taken from subsection 4.3.2), the Fresnel number is $F \approx 2.7$, so the Fraunhofer approximation is not a valid simplification.

The effects of partial coherence have to be considered in order to obtain quantitative results from experiments with coherent x-rays, e.g., partial coherence in x-ray photon correlation spectroscopy measurements has recently been found to reduce the q-resolution [7, 8]. Another important application is coherent diffractive imaging which is conventionally performed with an incident plane wave where perfect coherence is mandatory. However, in a recent work it has been shown that partially coherent illumination of a sample with a curved wave field produced by a lens is more likely to converge on a valid solution than illumination with partially coherent plane waves [29].

The propagation of coherence properties is usually described by a Gaussian Schell model. Schell-model sources are characterized by the property that the spectral degree of coherence or the coherence factor only depends on the difference between two positions in the source plane [30]. The following relations are expressed according to the considerations in [8, 9], and all fine details of the calculations are discussed in [7]. To calculate the wave propagation, the electrical field at a position $\vec{s}$ in the last aperture before the sample $\vec{E}(\vec{s},t) = \vec{A}(\vec{s},t)\exp(-i\omega t)$ is taken into account. ω denotes the average frequency of the radiation. The amplitude fluctuations due to the non-perfect monochromaticity $\vec{A}(\vec{s},t)$ are much slower than the period $T = 2\pi/\omega$ of the radiation. According to the Huygens-Fresnel principle, the electrical field in a second aperture after the sample and the intensity in the detector can be completely determined if the spatial and temporal behavior of the electric field in the first aperture and the electron density

in the sample are known [13]. One can then define the mutual coherence function of the radiation as [13, 30]

$$\Gamma(\vec{s},\vec{s}',\tau) = \left\langle \vec{A}(\vec{s},t)\vec{A}^*(\vec{s}',t+\tau)\right\rangle_t \tag{2.45}$$

which describes the correlation of the radiation between two different positions $\vec{s}$ and $\vec{s}'$ in the aperture at a time difference τ. $\vec{A}^*$ is the complex conjugate of $\vec{A}$ and the brackets $\langle\rangle_t$ indicate the average over all times t. According to [13, 30, 31] the following ansatz is performed, which is called the Schell form of the mutual coherence function:

$$\Gamma(\vec{s},\vec{s}',\tau) = \Psi(\vec{s})\Psi^*(\vec{s}')g(\vec{s}-\vec{s}')F(\tau)\frac{I}{A}. \tag{2.46}$$

$\Psi(\vec{s})$ denotes the amplitude factor, $g(\vec{s}-\vec{s}')$ the coherence factor with $g(0)=1$, $F(\tau)$ is the temporal autocorrelation function with $F(0)=1$ and $F(\infty)=0$, I describes the total intensity of the beam and A the aperture area. $F(\tau)$ is described as a simple exponential $F(\tau)=\exp(-\tau/\tau')$ with the characteristic decay time τ'. τ' can be interpreted as a coherence time with the corresponding longitudinal coherence length $\xi_\mathrm{l} = c\tau'$ where c denotes the velocity of light. The amplitude factor is normalized as $\int|\Psi|^2 dA = A$, and $|\Psi(\vec{s})|^2$ describes the density of the radiation flux at the position $\vec{s}$ in the aperture. Normally g is assumed to be of a Gaussian form: $g(\vec{s}-\vec{s}') \propto \exp[-(y^2/\xi_y^2 + z^2/\xi_z^2)/2]$, where ξ_y and ξ_z are transverse coherence lengths, y denotes the horizontal direction, i.e. the width of the aperture, and z indicates the vertical direction in which the height of the aperture is measured. When the amplitude distribution $\Psi(\vec{s})$ is also assumed to be Gaussian, this approximation is called the Gaussian Schell model.

The intensity in the detector positioned behind a second aperture which is placed behind the sample can be calculated in the kinematic approximation as [28]

$$I(\vec{q}) = \frac{r_e^2\omega}{2\pi\lambda^2}\cdot\frac{1}{L_1^2L_2^2}\cdot\frac{I}{A}\cdot S(\vec{q}) \tag{2.47}$$

with the distance L_1 between the first aperture and the sample, and the distance L_2 between the sample and the second aperture before the detector. The scattering function $S(\vec{q})$ which describes the scattered intensity is given as

$$S(\vec{q}) = \frac{q\xi_\mathrm{l}L_2^2}{ck^2}\int\frac{1}{\tilde{q}^2+(\tilde{q}k\xi_\mathrm{l}/q)^2(q-\tilde{q})^2}\left[\int_B \hat{S}_{\tilde{q}}\left(\vec{q}+\frac{k}{L_2}\vec{u}\right)d\vec{u}\right]d\tilde{q}, \tag{2.48}$$

where k denotes the mean wavevector of the incident radiation and $\tilde{q} = q(1+\Delta\lambda/\lambda) = q(1+\lambda/(2\xi_\mathrm{l}))$. The second integral with the integration constant $d\tilde{q}$ is taken over the area B of the detector aperture. It is interesting to note here that the effective coherence length in the experiment is ξ_l multiplied by a factor k/q which is rather large for surface

scattering experiments. The intensity recorded in the detector is therefore given by a Lorentzian resolution function which describes the longitudinal coherence projected into the sample plane convoluted with the function $\hat{S}_{\tilde{q}}(\vec{k})$ which is given by

$$\hat{S}_{\tilde{q}}(\vec{k}) = \iint \rho_{\mathrm{F}}(\vec{r})\rho_{\mathrm{F}}^{*}(\vec{r}\,')R(\vec{r}\,',\vec{r}) \exp\left[i\,\frac{\tilde{q}}{q}\,\vec{k}\cdot(\vec{r}\,'-\vec{r})\right] d\vec{r}\,'d\vec{r} \tag{2.49}$$

with the Fresnel electron density

$$\rho_{\mathrm{F}}(\vec{r}) = \rho(\vec{r}) \exp\left[i\,\frac{\tilde{q}k}{2q}\left(\frac{r_{\perp,1}^{2}}{L_1}+\frac{r_{\perp,2}^{2}}{L_2}\right)\right]. \tag{2.50}$$

$\vec{r}-\vec{r}\,'$ corresponds to the distance $\vec{s}-\vec{s}\,'$ of the positions in the aperture projected into the sample plane. $r_{\perp,1}$ and $r_{\perp,2}$ are the components of $\vec{r}$ perpendicular to the incident and exit wavevectors $\vec{k}_i$ and $\vec{k}_f$, respectively. In the Fraunhofer limit, i.e. the far field scattering case, L_1 and L_2 are very large and $\rho_{\mathrm{F}}(\vec{r})$ is reduced to the electron density $\rho(\vec{r})$. The second term in Eq. 2.49 can be calculated as

$$R(\vec{r}\,',\vec{r}) = \iint \Psi(\vec{s})\Psi^{*}(\vec{s}\,')g(\vec{s}-\vec{s}\,') \exp\left[i\,\frac{\tilde{q}k}{qL_1}\left(\frac{\vec{s}^{\,2}-\vec{s}\,'^{2}}{2}+\vec{s}\,'\cdot\vec{r}\,'-\vec{s}\cdot\vec{r}\right)\right] d\vec{s}\,d\vec{s}\,'. \tag{2.51}$$

In the incoherent case, the transverse coherence lengths ξ_y and ξ_z are zero, and the coherence factor is a delta distribution $g(\vec{s}-\vec{s}\,') = \delta(\vec{s}-\vec{s}\,')$. Then $R(\vec{r}\,',\vec{r})$ is only a function of the distance $\vec{r}\,'-\vec{r}$, namely the Fourier transform of $|\Psi|^2$ which is assumed to be Gaussian-shaped. The result which one obtains then for the detected intensity is the same as the conventional result calculated by convolution with a finite resolution function where $\rho_{\mathrm{F}}(\vec{r})$ is assumed as the electron density. However, this conventional procedure is only valid if either the sample is illuminated by a completely incoherent source, or in the far-field Fraunhofer diffraction regime for which in case of x-rays very large distances between the aperture and the sample are required [13].

An experimental example for the effects of partial coherence is presented in Fig. 2.8, showing so-called speckle patterns from a soft-matter thin film of polystyrene (PS) and polymethylmethacrylate (PMMA), coated with a 200 Å gold layer. The colors are inverted in the CCD pictures in the left part of the figure, and the low intensity in the center of each image is due to a beamstop. Speckles are created by illuminating a medium with a randomly varying refractive index with (partially) coherent light [32]. It is obvious that the pinhole size influences the degree of coherence, because a larger pinhole size increases the scattering volume. With increasing scattering volume compared to the coherence volume, the resulting measurements become more similar to an experiment with incoherent radiation. This development can be seen by comparing the

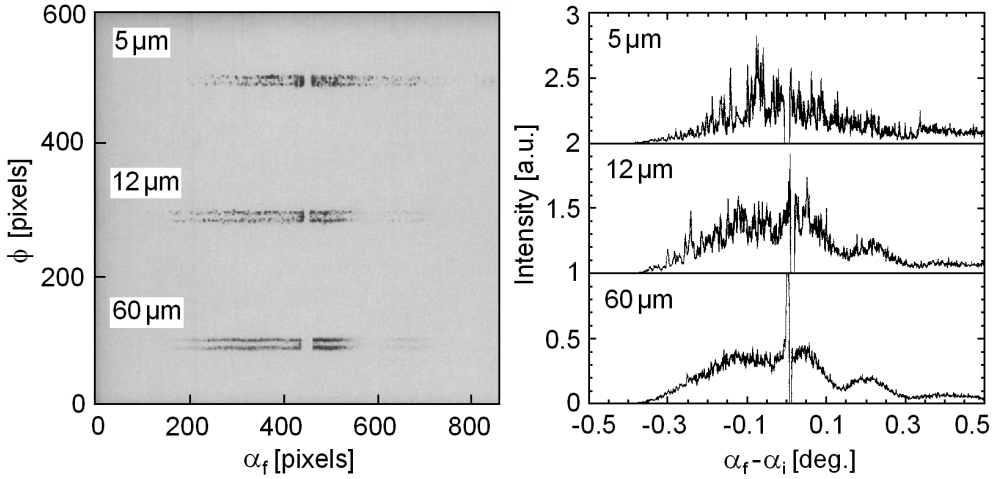

Figure 2.8: 2D Speckle patterns with corresponding line profiles from an annealed thin diblock copolymer film of PS and PMMA, coated with 200 Å gold. The collimating pinhole sizes are 5 μm (top), 12 μm (middle), and 60 μm (bottom), respectively. The images are taken from [32] and slightly modified.

top with the bottom pictures in Fig. 2.8. The scattering patterns in the left part of the figure obtained by using pinholes with 5 μm and 12 μm diameters clearly show the granular structure of the speckles, which can also be seen in the large fluctuations of the line profiles along the exit angle direction α_f on the right. Contrary to the small pinholes, for the 60 μm pinhole the fluctuations are within the statistical photon noise and the speckle pattern is lost, so only broad diffuse scattering features are still visible.

2.4.3 X-ray photon correlation spectroscopy

When (partially) coherent radiation impinges on a surface of a sample containing spatial or temporal inhomogeneities, then the scattered intensity forms a speckle pattern, i.e. bright spots whose positions and intensities are sensitive to the structure of the material. In the previous subsection only static samples were considered. However, if the sample structure is subject to temporal changes, e.g., due to aging, then the speckle pattern changes accordingly. These changes can be measured by calculating the intensity-intensity autocorrelation function, i.e. multiplying the intensity of a speckle with the intensity after a certain time delay τ, thus revealing information about the dynamics of the material.

The technique of x-ray photon correlation spectroscopy (XPCS) has been adapted from scattering with visible laser light where it is called dynamic light scattering (DLS) or photon correlation spectroscopy (PCS) [33]. Contrary to visible light scattering,

coherence is more difficult to achieve with x-rays: As discussed in the beginning of this section, the coherence lengths are proportional to λ, the brilliance is $\propto \lambda^2$, and the number of photons per coherence volume is even $\propto \lambda^3$. In spite of the challenges of using x-rays instead of laser light, the obvious advantages of x-rays consist in the possibility of studying opaque materials at length scales smaller than 200 nm. Fig. 2.9 illustrates the experimentally accessible length and time scales for XPCS measurements compared to other scattering methods. Due to the short wavelengths of x-rays, XPCS allows to study materials on shorter length scales than DLS. As the energy transfer for DLS and XPCS experiments is very small, one can describe these methods as quasi-elastic, and the detectable time scales are therefore much larger than for inelastic scattering methods.

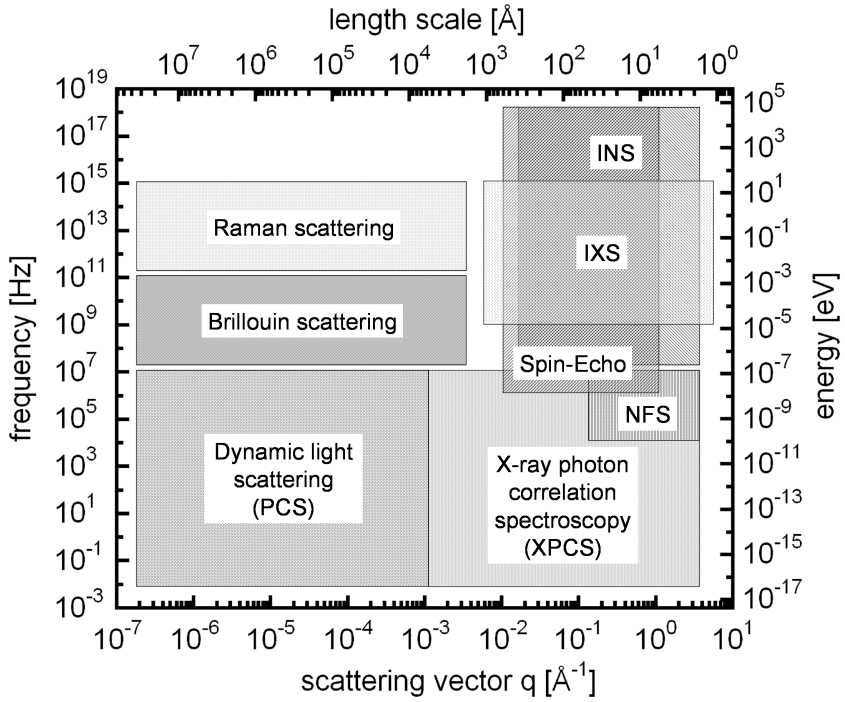

Figure 2.9: Range of applications for XPCS and complementary techniques as a function of frequency (energy) and scattering vector (length scale). INS stands for inelastic neutron scattering, IXS for inelastic x-ray scattering, and NFS is nuclear forward scattering. Figure taken from [34] and modified.

The occurrence of x-ray diffraction speckles as a general property in disordered materials has been first pointed out by K. F. Ludwig in 1988 [35]. It is also stressed there that speckles cannot typically be seen in diffraction experiments with x-rays or neutrons, because normally the scattering volume is larger than the coherence volume of the radiation, or in other words, the inverse sample size is much smaller than the q-space resolution width of the experiments. In 1991 speckles have been observed with

hard x-rays in the Bragg reflection of a single crystal of Cu_3Au [36], and in 1994 the first x-ray speckle measurements in grazing incidence geometry were performed on thin diblock copolymer films [32] as shown in the previous subsection.

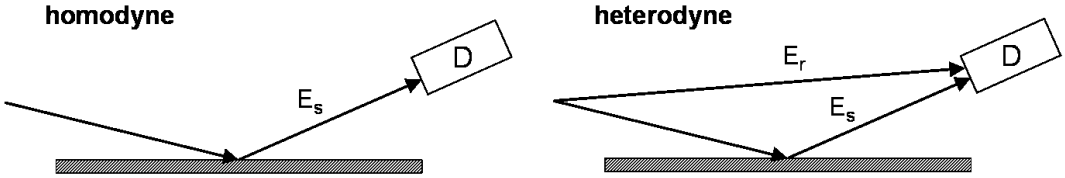

Figure 2.10: Comparison between homodyne (left) and heterodyne (right) detection schemes. For homodyne detection only the electric field scattered by the sample E_s is recorded by the detector (D), whereas for heterodyne scattering it is superposed by an additional reference field E_r.

In the following, XPCS will be explained for measuring the dynamics of liquid surfaces. If a sample changes in time, the speckle pattern reflected from the surface changes as well. One can distinguish between homodyne and heterodyne detection as pictured in Fig. 2.10. First the homodyne scattering scheme will be explained. The changes in the dynamics of the sample can be calculated by means of the temporal intensity-intensity autocorrelation function which is defined as

$$G_2(\vec{q}_1, \vec{q}_2, \tau) = \langle I(\vec{q}_1, t) I(\vec{q}_2, t+\tau) \rangle_t \tag{2.52}$$

with the scattering vectors $\vec{q}_1$ and $\vec{q}_2$ and the time interval τ between individual intensity measurements. The brackets $\langle\rangle_t$ indicate the average over all times t. G_2 is a second-order correlation function, because the intensities which are the squares of the electric fields are correlated. It can also be expressed in terms of the scattered electric fields as

$$G_2(\vec{q}_1, \vec{q}_2, \tau) = \langle E^*(\vec{q}_1, t) E(\vec{q}_1, t) E^*(\vec{q}_2, t+\tau) E(\vec{q}_2, t+\tau) \rangle_t \,. \tag{2.53}$$

On condition that the scattered electric fields are subject to Gaussian statistics and their mean value is zero, G_2 can be transformed into [7, 30]

$$G_2(\vec{q}, \tau) = \langle I(\vec{q}, t) \rangle_t \langle I(\vec{q}, t) \rangle_t + |G_1(\vec{q}, \tau)|^2 \tag{2.54}$$

$$\Rightarrow g_2(\vec{q}, \tau) = \frac{G_2(\vec{q}, \tau)}{\langle I(\vec{q}, t) \rangle_t^2} = 1 + \frac{|G_1(\vec{q}, \tau)|^2}{\langle I(\vec{q}, t) \rangle_t^2} \tag{2.55}$$

$$\Rightarrow g_2(\vec{q}, \tau) = 1 + |g_1(\vec{q}, \tau)|^2 \tag{2.56}$$

with the normalized correlation function of the electric fields

$$g_1(\vec{q}, \tau) = \frac{\langle E^*(\vec{q}, t) E(\vec{q}, t+\tau) \rangle_t}{\langle E(\vec{q}, t) \rangle_t^2}. \tag{2.57}$$

Eq. 2.56 is the so-called Siegert relation which is commonly used for the analysis of XPCS data and allows to calculate higher-order correlation functions.

However, it should be noted here that in general it cannot be taken for granted that the scattered field is subject to Gaussian fluctuations, which is the prerequisite for the application of the Siegert relation [7, 37]. An example is the case of heterogeneous dynamics as shown by A. Duri [38] who calculated higher order correlation functions for DLS measurements on slow relaxation in glassy soft matter. These non-Gaussian fluctuations occur in systems that have several regions of different dynamics, and one can show that the resulting correlation function obtained by adding up correlation functions with slightly different time scales exhibit a stretched exponential behavior, i.e. $g_2(\tau) = 1 + \beta \exp[-2(\Gamma\tau)^\alpha]$ with the relaxation rate Γ, the time constant τ and the exponent $0 < \alpha < 1$. The contrast or degree of coherence β is usually 1 in DLS experiments as long as not more than one speckle per pixel of the detector occurs.

For surface sensitive XPCS measurements the incident radiation impinges at an angle smaller than the critical angle onto the sample surface. To analyze the scattered intensity, the dependence of $g_1(\vec{q}, \tau)$ on the surface fluctuations has to be determined. It should be noted here that in general the field fluctuations do not only depend on the electron density fluctuations of the scatterer, but also on the fluctuations of the incident radiation [8]. If, under ideal conditions, effects of the detector resolution and partial coherence can be neglected, as well as the Fraunhofer scattering case can be assumed, the first-order correlation function $G_1(\vec{q}, \tau)$ is proportional to the height correlations of the liquid surface which are expressed by the normalized height-height correlation function $C(q_{||}, \tau)$. $C(q_{||}, \tau)$ is proportional to the Fourier transform of the dynamic structure factor $f(q_{||}, \tau)$ [39] with the frequency ω:

$$C(q_{||}, \tau) \propto \int_0^\infty f(q_{||}, \tau) e^{i\omega\tau} d\omega. \tag{2.58}$$

The dynamic structure factor can therefore be measured directly with surface sensitive XPCS. In the following, the correlation function is assumed to be temporally and spatially stationary, i.e. it does not depend on a special position at a certain time. As an example, the case of propagating and overdamped capillary waves as described in Tab. 3.1 will be discussed. For propagating waves on a liquid with low viscosity the dynamic structure factor $f(q_{||}, \tau)$ can be described by a Lorentzian [23]:

$$f(q_{||}, \tau) = \left(\pi\Gamma_0 \left[1 + \left(\frac{\omega - \omega_0}{\Gamma_0} \right)^2 \right] \right)^{-1}. \tag{2.59}$$

The low-viscosity damping constant is hereby given by $\Gamma_{0,\mathrm{lv}} = 2\eta q_{||}^2/\rho$ with the viscosity η and the mass density ρ of the liquid, and $\omega_0 = \sqrt{\gamma/\rho}\, q_{||}^{3/2}$ is the frequency of the

propagating waves [40]. The height-height correlation function can then be calculated as

$$C(q_{||},\tau) = g_1(q_{||},\tau) = \cos(\omega_0\tau)e^{-\Gamma_{0,\mathrm{lv}}\tau}. \tag{2.60}$$

Inserting this result into the Siegert relation (Eq. 2.56) yields the autocorrelation function of the scattered intensity

$$g_{2,\,\mathrm{low-visc.}}(q_{||},\tau) = 1 + \cos^2(\omega_0\tau)e^{-2\Gamma_{0,\mathrm{lv}}\tau}. \tag{2.61}$$

A similar calculation can be performed for overdamped capillary waves due to a high viscosity. In this case the dynamic structure factor is again described by a Lorentzian as in Eq. 2.59, but centered at $\omega = 0$. The high-viscosity damping constant is also different and given by $\Gamma_{0,\mathrm{hv}} = \gamma q_{||}/(2\eta)$ [40]. Contrary to the low-viscosity case where the damping only depends on the viscosity, it is now also affected by the surface tension γ. The intensity correlation function follows then as

$$g_{2,\,\mathrm{high-visc.}}(q_{||},\tau) = 1 + e^{-2\Gamma_{0,\mathrm{hv}}\tau}. \tag{2.62}$$

Until now, only homodyne correlation functions have been considered, for which the measured intensity only depends on the electric fields scattered by the sample. However, one has to distinguish between homodyne and heterodyne scattering as illustrated in Fig. 2.10. Contrary to the homodyne detection scheme, for heterodyne scattering the scattered field is superposed by a reference field much stronger than the radiation itself [41]. For heterodyne mixing, the detected intensity is [42]

$$\begin{aligned} I(\vec{q},t) &= [E_\mathrm{s}(\vec{q},t)E_\mathrm{r}(t)]\,[E_\mathrm{s}(\vec{q},t)E_\mathrm{r}(t)]^* && (2.63)\\ &= I_\mathrm{s}(\vec{q},t) + I_\mathrm{r}(t) + 2\Re\{E_\mathrm{s}(\vec{q},t)E_\mathrm{r}^*(t)\}, && (2.64)\end{aligned}$$

where E_s and E_r denote the electric fields of the scattered and the reference beams, respectively, and * indicates the complex conjugation. The corresponding correlation function is then calculated as [42]

$$\begin{aligned} G_2(\vec{q},\tau) &= \langle I(\vec{q},t)I(\vec{q},t+\tau)\rangle_t && (2.65)\\ &= \langle I_\mathrm{s}(\vec{q}) + I_\mathrm{r}\rangle_t^2 + 2\,\langle I_\mathrm{s}(\vec{q})\rangle_t\,\langle I_\mathrm{r}\rangle_t\,g_1(\vec{q},\tau) + \langle I_\mathrm{s}(\vec{q})\rangle_t^2\,(g_2(\vec{q},\tau)-1) && (2.66)\\ &\approx \langle I_\mathrm{r}\rangle_t^2 + 2\,\langle I_\mathrm{s}(\vec{q})\rangle_t\,\langle I_\mathrm{r}\rangle_t\,g_1(\vec{q},\tau). && (2.67)\end{aligned}$$

In the normalized form this is expressed as

$$g_2(\vec{q},\tau) \approx 1 + 2\frac{\langle I_\mathrm{s}(\vec{q})\rangle_t}{\langle I_\mathrm{r}\rangle_t}g_1(\vec{q},\tau). \tag{2.68}$$

The contrast of the correlation function can be defined as $C = 2\langle I_{\mathrm{s}}(\vec{q})\rangle_t / \langle I_{\mathrm{r}}\rangle_t$ and decreases for increasing reference intensity [8]. For heterodyne detection, the measured intensity correlation function is proportional to the electric field correlation function, and for the example of propagating capillary waves it is given by

$$g_{2,\,\mathrm{low-visc.}}(q_{||},\tau) = 1 + \cos(\omega_0\tau)e^{-\Gamma_{0,\mathrm{lv}}\tau}, \tag{2.69}$$

which can be easily distinguished from the homodyne case due to the cos versus $\cos^2$ behavior. For overdamped capillary waves this distinction is not so unequivocal, because it differs only by a factor 2 in the damping constant:

$$g_{2,\,\mathrm{high-visc.}}(q_{||},\tau) = 1 + e^{-\Gamma_{0,\mathrm{hv}}\tau}. \tag{2.70}$$

Artificial heterodyne mixing has been attempted by R. Fendt et al. by using a grating in front of the pinhole producing diffraction maxima at well-defined angles [8]. A part of the incident radiation is then deflected, and if the detector is placed close to a diffraction maximum, the detected intensity depends on the superposition of the scattered and reference field E_{s} and E_{r}, respectively. But this setup is not trivial to realize due to the small coherence lengths for x-rays. However, intrinsic heterodyne mixing, i.e. without explicitly creating a reference beam, has been observed for water [43] and glycerol [12]. This effect becomes significant for small $\vec{q}$ or for broad specular beams and can be explained with resolution effects which have been treated thoroughly by T. Ghaderi [7]. If a limited $\vec{q}$ resolution is taken into account, the dynamic structure factor gets broader and shifted to higher frequencies [8].

3 Glass transition at surfaces of polymer melts

When a liquid is cooled towards the glass transition (which strongly depends on the thermal history), one observes a dramatic increase of its viscosity η before the system is finally falling out of thermal equilibrium and forms a disordered glassy state. As will be shown in the following subsection, η increases exponentially with decreasing temperature. A most commonly used definition of the glass transition is the temperature where η exceeds the value of 10^{12} Pa·s. As a result, in the bulk of glassy materials static frozen-in density fluctuations of long wavelengths exist [44]. In thin films the glass transition temperature T_{G} changes as the film thickness is reduced, which strongly depends on the polymer-substrate interaction [45, 46, 47, 48, 49], e.g., a decrease in T_{G} is explained with an enhanced chain mobility near hard neutral walls (or air) due to a molten surface layer [48, 50, 51, 52], whereas for attractive polymer-wall interaction the chains are less mobile, thus leading to an increase in T_{G} [48].

At free surfaces and interfaces the additional boundary condition leads to new hydrodynamic modes (i.e. capillary waves) which are present only near surfaces and interfaces. Capillary waves are generated by the thermal motion of the molecules in the liquid with the surface tension acting as restoring force of the perturbed surface [53]. Hence, the amplitudes of the surface displacement which correspond to the surface roughness are inversely proportional to the square root of the surface tension. The length scales Λ of the capillary waves range from 10^{-2} m to the nanometer region and they are extending into the material underneath with a penetration depth of $2\pi\Lambda$. The capillary waves lead to a surface roughness of most liquids on the order of 1-10 Å. As discussed in subsection 2.4.3, the relaxation time τ of the dynamics in the liquid is determined by the viscosity, therefore for small η propagating waves occur on the surface which are overdamped for higher viscosities.

Surface fluctuations typically manifest themselves in a characteristic power-law dependence of the diffuse scattering [19, 54, 55, 56]. Dynamic processes on the surface can be monitored by x-ray photon correlation spectroscopy experiments, e.g., the transition

from propagating to overdamped capillary waves in water-glycerol mixtures, depending on the viscosity and the investigated length scale [57]. In thermal equilibrium the surface roughness depends only on the surface tension [58], whereas in non-equilibrium (e.g. glasses or highly viscous liquids) the surface fluctuations are expected to be partly frozen in close to the glass transition [39, 59].

In this chapter it is investigated whether an analogous effect of freezing in of fluctuations as known in the volume occurs at the free surface, i.e. how the capillary wave spectrum freezes in at the glass transition. This question has been addressed in two previous papers, however, with inconclusive results [60, 61]. X-ray scattering results on liquid glycerol have been hampered by the presence of a thin layer on top of the glycerol surface [60] and a previous study on the surface roughness on PPG showed no evidence of the glass transition because the covered temperature range was too small [61]. In this work the freezing in of the surface roughness of a polymer melt depending on the applied cooling rate is monitored. For the first time a transition in the temperature dependence of the surface roughness to a partly frozen in state is observed. The results are compared with the viscoelastic theory of the surface glass transition by Jäckle and Kawasaki [39, 59].

3.1 Theoretical background

3.1.1 Glass formation and dynamical behavior of glasses

Glasses are amorphous materials that have cooled to rigidity without crystallizing. They behave mechanically like solids, but without the periodicity of crystals. Commonly glasses are produced by supercooling a viscous liquid, i.e. cooling it fast enough to prevent crystallization [62]. Then the molecules become so slow that they cannot rearrange fast enough to form an ordered solid in the available time given by the applied cooling rate, so the system falls out of equilibrium and appears to be frozen in on the experimental time scale [1]. Apart from cooling of a liquid, glasses can be formed in various ways, by vapor condensation, particle bombardment of a crystal, or a chemical reaction of organic material followed by drying [63]. For the measurements presented in this work, only the method of cooling down a liquid is employed, therefore the other glass forming processes will not be treated here. The necessary conditions to form a glass are discussed in [62]. As a material is more stable in a crystalline than in a glassy form, crystallization during cooling of a melt can be avoided by a large cooling rate and by using a material with a small crystallization rate. A small seed density is also important, because crystal

growth is catalyzed by impurities or seed crystals of the material itself, although homogeneous nucleation without seeds is also possible. The probability of forming a crystal nucleus is less the smaller the volume of the liquid and the larger the cooling rate and the liquid-crystal interface tension are. Finally, a glass is formed more likely when the ratio between the glass transition temperature to the crystallization temperature $T_\mathrm{G}/T_\mathrm{m}$ is large [62].

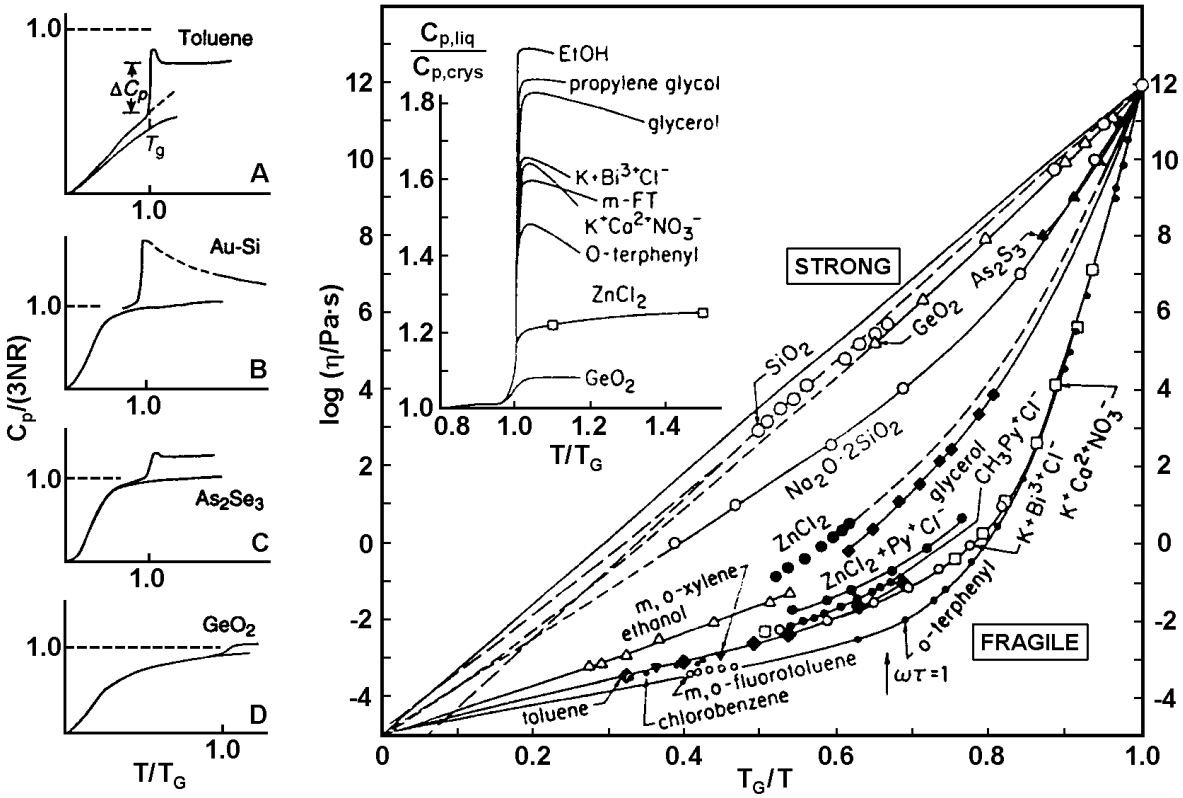

Figure 3.1: Left: normalized heat capacity C_p as a function of temperature for different materials. Right: Arrhenius plots of the viscosity η scaled by T_G for strong and fragile liquids (figures taken from [2] and modified).

The glass formation for different kinds of liquids is pictured in Fig. 3.1. The glass transition is described by a temperature region over which a system falls out of equilibrium. One can define the glass transition temperature T_G in different ways which are arbitrary due to the lack of international conventions. One definition is the temperature at which the heat capacity C_p[1] increases rapidly during heating with 10 K/min. These results obtained by differential scanning calorimetry are pictured in the left part of Fig. 3.1, where C_p divided by $3NR$ (with the number of atoms per formula unit N

[1] C_p is defined as the supplied heat dQ per temperature interval dT at constant pressure p.

and the gas constant R) is plotted versus T normalized by T_G. Usually the structural relaxation time τ, which is defined as the average time needed by one particle to move over one interparticle distance [63] (which is proportional to the shear viscosity [62]), changes between 100 s and 0.1 s during this change of C_p. With the change in the heat capacity ΔC_p plotted in part A of Fig. 3.1, T_G can be specified as the temperature where $\tau = 100$ s with a temperature scanning rate of 10 K/s [64]. Although it is not the most commonly used definition, it might be noted here that T_G can also be defined as the temperature where $\tau = 10^5$ s or about one day, i.e., a material is a solid glass when its shape is not changed during one day under the application of a small shear force [62].

The extent of the change of C_p gives information about the fragility of the liquid. In molecular systems like toluene (picture A in Fig. 3.1) ΔC_p is large, therefore they are fragile, whereas metallic or covalent systems like Au-Si (B) or As_2Se_3 (C), respectively, have a smaller ΔC_p and are less fragile, and finally open network systems like GeO_2 (D) where ΔC_p is rather small are strong liquids. This classification of liquids indicating the sensitivity to temperature changes can also be seen in the inset of the so-called Arrhenius plots in Fig. 3.1. Generally ΔC_p is large for fragile liquids which fluctuate over many different particle orientations and small for strong liquids which are resistant to structural changes, but exceptions due to hydrogen bonding exist. The slope of the viscosity in the Arrhenius plot near T_G is generally used to define the so-called fragility index m [65].

As the internal relaxation time τ is proportional to the viscosity η which increases exponentially with decreasing temperature, one can also define T_G as the point where η exceeds a value of 10^{12} Pa·s. This is pictured in the right part of Fig. 3.1. Strong liquids like SiO_2, GeO_2 or BeF_2 show an Arrhenius behavior of the viscosity:

$$\eta(T) \propto \exp\left(-\frac{A}{k_B T}\right), \tag{3.1}$$

where A is a constant, whereas fragile liquids like polymer melts behave according to the Vogel-Tammann-Fulcher law:

$$\eta(T) \propto \exp\left(-\frac{A}{T - T_0}\right), \tag{3.2}$$

with the Vogel-Tammann-Fulcher temperature T_0 which is about 50 K below T_G [66]. Therefore, in an Arrhenius plot strong liquids exhibit a mostly linear behavior whereas fragile materials show stronger deviations from this line. Strong liquids can become fragile when they are compressed. The most fragile liquids are polymers where the viscosity also depends on the molecular weight, therefore they cannot simply be inserted into Fig. 3.1. The characteristics of polymers will be discussed in subsection 4.1.1.

In dynamic light scattering (DLS) experiments the viscoelastic relaxation is probed by measuring the dynamic structure factor $f(\vec{q},\tau)$ which yields information about density correlations in the sample. A characteristic feature of $f(\vec{q},\tau)$ above T_G is its two-step decay: On timescales faster than nanoseconds a fast decay, the so-called β-relaxation, occurs from the initial value $f(\vec{q},0) = 1$ to the so-called nonergodic level f_q where it reaches a plateau [67]. This structural relaxation is associated with subsegmental relaxations such as reorientations of an ester side group [68].

Neutron spin-echo measurements performed by Frick and Richter revealed that f_q exhibits a maximum at the main peak position of the static structure factor $S(\vec{q})$ [69]. As the wavevector position of this peak corresponds to correlated distances that are preferred by the system, these correlations decay more slowly (so-called de-Gennes narrowing [70]), and the relaxation rate is minimal there.

The final decay of $f(\vec{q},\tau)$ from the plateau at f_q to zero is called the α-relaxation and corresponds to the viscoelastic relaxation of the liquid. It is associated with cooperative motion, i.e. relaxation of rearranging regions of tens to hundreds of repeated units [68]. The relaxation times for the α-relaxation are 100 s near T_G. This relaxation process is represented by a stretched exponential ($\alpha < 1$) according to

$$f(\vec{q},\tau) = f_q \exp[-(t/\tau)^\alpha]. \tag{3.3}$$

Eq. 3.3 is called the Kohlrausch-Williams-Watts function [71] and describes for example the stress in a material caused by deformation.

The two-step decay of the dynamic structure factor can be explained by the cage effect describing the confinement of particles in transient cages formed by their neighbors [72]. The initial decay of $f(\vec{q},\tau)$ is explained by particles exploring the vicinity of their cage. For solids, this decay is arrested at the nonergodic level. Thus, the Debye-Waller factor defining the average mean-squared particle displacement is also a synonym for the nonergodic level. Recently, DLS measuments performed by D. L. Sidebottom et al. indicate that the α-relaxation can be solely described by T_G and the nonergodic level f_0 for $\vec{q} \to 0$ [67].

3.1.2 Cooling rate dependence of the glass transition

In Fig. 3.2 a sketch of the specific volume V_sp (which is defined as the volume per mass) as a function of temperature is shown for a liquid which can both crystallize and form a glass. It can be clearly seen that the glass transition strongly depends on the cooling rate. For slow cooling rates the molecules in the liquid have enough time to rearrange themselves so that a more ordered structure (a crystal) can be formed. For faster cooling

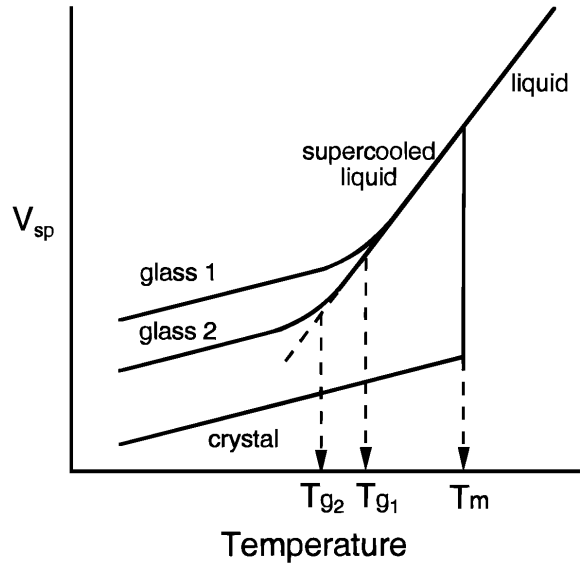

Figure 3.2: Sketch of the specific volume as a function of temperature for a liquid able to crystallize and to form a glass [73].

rates the liquid is in a supercooled state when it is cooled below the melting temperature T_{m} (also called freezing or crystallization temperature), and the molecular motion slows down [1]. In Fig. 3.2 glass 2 is formed with a faster cooling rate than glass 1. One can then define the glass transition temperatures T_{g1} or T_{g2} by extrapolating V_{sp} in the glassy state to the supercooled liquid line.

The dependence of T_{G} on the cooling rate ϕ of glass formers has been extensively investigated in the past. Measurements of the heat capacity revealed a linear relation of T_{G} with the logarithm of the heating or cooling rate [74, 75]. As this would indicate that no lower limit for T_{G} exists, later works assume a Vogel-Fulcher form [76] with $T_{\mathrm{G}} = T_{\mathrm{G}}^0 + A/\ln(B/\phi)$, where A and B are constants and T_{G}^0 represents the asymptotic limit of T_{G} for infinitely slow heating or cooling, and discuss different models for the non-equilibrium kinetics around T_{G} [77]. Strong glass formers like B_2O_3 show a more linear relationship between T_{G} and $\log\phi$, and slower cooling results in a glass with a higher density [77]. Molecular dynamics simulations on a Lennard-Jones model and silica support a Vogel-Fulcher or power law behavior for $T_{\mathrm{G}}(\phi)$, the later one originating in mode coupling theory calculations. Slower cooling rates result in a faster glass transition and a smaller T_{G} [78]. However, a more refined treatment of glassy dynamics is still needed in order to find an exact expression for $T_{\mathrm{G}}(\phi)$ [79]. It should be stressed here that in the bulk the cooling rate dependence of the glass transition temperature is typically rather weak. T_{G} changes by 3-5 K when the cooling rate is changed by an order of magnitude [73].

3.1.3 Capillary waves on liquid surfaces

Buff et al. have first attributed the temperature dependence of the interfacial width of liquids to thermally excited capillary waves [80]. On liquid surfaces fluctuations of different wavelengths exist which can be described by a dispersion relation where the phase velocity c is plotted versus the wavelength λ.

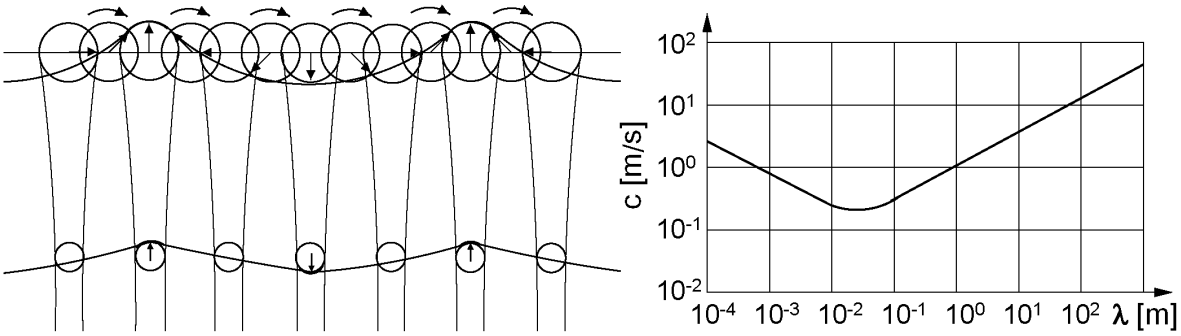

Figure 3.3: Left: Propagation of waves on a liquid surface. The arrows on top indicate the direction of the circular motion of the particles. Right: Dispersion relation (phase velocity c versus wavelength λ) for capillary waves ($c \propto \sqrt{1/\lambda}$) and gravitational waves ($c \propto \sqrt{\lambda}$) in deep water [81].

Fig. 3.3 shows a schematic representation of the wave motion on a liquid surface together with the dispersion relation for surface waves in deep water. At large wavelengths the dynamics on the surface is dominated by so-called gravitational waves, whereas for wavelengths smaller than about a centimeter down to the nanometer region capillary waves prevail. Gravitational waves are excited mechanically, e.g. by wind, and the acceleration due to gravity g is the restoring force. Their dispersion relation is given by $c_{\text{grav}} = \sqrt{g\lambda/(2\pi)}$. Capillary waves are generated by the thermal motion of the molecules in the liquid with the surface tension γ acting as restoring force of the perturbed surface, and they lead to a surface roughness of most liquids on the order of 1-10 Å. They are damped exponentially in the direction perpendicular to the surface. Their dispersion relation can also be expressed by the frequency ω as a function of the wavevector transfer q as [42]

$$\omega(q) = \sqrt{\frac{\gamma q^3}{\rho}} + i\,\frac{2\eta q^2}{\rho} \tag{3.4}$$

with the density ρ and the viscosity η. From the real part of this expression the phase velocity $c_{\text{cap}} = \omega/q$ with $q = 2\pi/\lambda$ can be calculated as $c_{\text{cap}} = \sqrt{2\pi\gamma/(\rho\lambda)}$ [81]. The macroscopic surface tension $\gamma(T)$ can be defined as the work dW needed to increase the

surface of the amount dA. Depending on the viscosity of the liquid (and therefore on the temperature), one can distinguish between propagating and overdamped capillary waves. The low and high viscosity cases are summarized in Tab. 3.1. The transition from propagating to overdamped behavior has been recently investigated for the example of a mixture of water and glycerol with a 65% weight concentration of glycerol [57].

	propagating cap. waves	overdamped cap. waves
viscosity	$\eta^2 \ll \gamma\rho/(4q)$	$\eta^2 \gg \gamma\rho/(4q)$
damping	$\Gamma = (2\eta/\rho) \cdot q^2$	$\Gamma = (\gamma/2\eta) \cdot q$
frequency	$\omega = \sqrt{\gamma/\rho} \cdot q^{3/2}$	—

Table 3.1: Low and high viscosity limits for capillary waves [82]. For propagating capillary waves the real part of the frequency is given, and overdamped waves have of course no propagation frequency. The damping constant or relaxation rate Γ is inversely proportional to the relaxation time τ.

In order to characterize the surface glass transition, the height-height correlation function $C(R) = \langle z(r+R)z(r)\rangle_r$ with $z(r)$ denoting the surface displacement from equilibrium at position r is used. According to classical hydrodynamics, the structure factor, i.e. the Fourier transform of $C(R)$ of thermal height fluctuations on liquid surfaces is [39]

$$S(q_{||}, T) = \frac{k_\mathrm{B}T}{\gamma(T)} \cdot \frac{1}{q_{||}^2 + q_\mathrm{min}^2}, \tag{3.5}$$

with the Boltzmann constant k_B, the temperature T, the wavevector transfer parallel to the surface $q_{||}$ and the wavevector cutoff q_min, which is given by gravity for the case of bulk liquids. $\gamma(T)$ denotes the temperature dependent surface tension of the liquid. By integrating over the experimentally accessible $q_{||}$ range, the square of the surface roughness σ can be calculated as [39]

$$\sigma^2(T) = \frac{1}{2\pi}\int_{q_\mathrm{min}}^{q_\mathrm{max}} S(q_{||}, T) q_{||}\, dq_{||} = \frac{k_\mathrm{B}T}{2\pi\gamma(T)} \ln\left(\frac{q_\mathrm{max}}{q_\mathrm{min}}\right). \tag{3.6}$$

q_max is on the order of $2\pi/d$ with the molecular diameter d. In an x-ray reflectivity experiment, $q_\mathrm{min} = q_z \Delta\alpha_f/2$ is determined by the detector resolution $\Delta\alpha_f$ and depends on the wavevector transfer perpendicular to the surface $q_z = (4\pi/\lambda)\sin(\alpha_i)$ with the wavelength λ and the incident angle α_i of the radiation with respect to the surface. Therefore, in the liquid state the surface roughness depends on the temperature via $\sigma^2 \propto T/\gamma(T)$ which gives rise to a peculiar bending of $\sigma^2(T)$ [61].

3.1.4 Jäckle-Kawasaski model: viscoelastic theory

The theory of fluctuations perpendicular to a liquid's surface caused by thermally induced capillary waves has been treated e.g. by Loudon who calculated the power spectrum of the fluctuations [53]. The thermodynamic variables of a system in thermal equilibrium are subject to arbitrary fluctuations. The statistical properties of these fluctuations are determined by the thermal excitation probabilities of the different states of the system. The power spectrum of the fluctuations can be calculated with the linear response theory [83] applied to the reaction of the surface to an external force using the fluctuation-dissipation theorem [84]. The surface displacement $u_z(q,t)$ due to a weak external force $F_z(q,t) = F_{z,0} \cdot \exp[i(qx - \omega t)]$ is given by [39]

$$u_z(q,t) = F_z(q,t) \cdot \chi(q,\omega) = u_{z,0} \cdot \exp[i(qx - \omega t)] \tag{3.7}$$

with the dynamic susceptibility $\chi(q,\omega)$ of the vertical surface displacement with respect to $F_z(q,t)$. According to the fluctuation-dissipation theorem the power spectrum of the thermal height fluctuations is determined by the imaginary part of $\chi(q,\omega)$. $\chi(q,\omega)$ can be calculated with hydrodynamic theory as [39]

$$\chi(q,\omega) = \frac{q/\rho}{\omega_s^2(q) - \omega^2 - \mathrm{i}\omega\Gamma(q,\omega)} \tag{3.8}$$

with the damping term

$$\Gamma(q,\omega) = 4\frac{\eta(\omega)q^2}{\rho} + \frac{\mathrm{i}}{\omega}4\frac{\eta^2(\omega)q^4}{\rho^2}\left(1 - \sqrt{1 - \frac{\mathrm{i}\omega\rho}{\eta(\omega)q^2}}\right). \tag{3.9}$$

$\eta(\omega)$ denotes the viscosity and ρ the density of the liquid. The frequency of the surface waves of an ideal incompressible liquid with infinite depth is given by

$$\omega_s(q) = \sqrt{gq + \frac{\gamma}{\rho}q^3} \tag{3.10}$$

with the acceleration due to gravity g and the surface tension γ. The static susceptibility follows as $\chi(q) = (\rho g + \gamma q^2)^{-1}$, and the static structure factor is then calculated as

$$S(q) = \frac{1}{2\pi}\int_{-\infty}^{+\infty} S(q,\omega)d\omega = k_B T\chi(q) = \frac{k_B T}{\rho g + \gamma q^2}. \tag{3.11}$$

Therefore, the square of the surface roughness follows as

$$\sigma^2 = \left\langle |u_z|^2 \right\rangle_q = \frac{1}{(2\pi)^2}\int_{q_{\min}}^{q_{\max}} S(q)d^2q = \frac{k_B T}{4\pi\gamma}\ln\left(\frac{\gamma q_{\max}^2}{\rho g}\right) \tag{3.12}$$

with the upper cut-off wavevector $q_{\max}$. With a lower cut-off wavevector of $q_{\min} = \sqrt{\rho g/\gamma}$, Eq. 3.12 is in agreement with Eq. 3.6.

A supercooled liquid with increasing viscosity is then discussed by Jäckle and Kawasaki as an incompressible viscoelastic medium with a Maxwell-Debye model for the frequency dependent viscosity [39, 59]

$$\eta(\omega) = \frac{\eta_0}{1 - i\omega\tau}. \tag{3.13}$$

η_0 denotes the temperature dependent low-frequency hydrodynamic value of the viscosity, and $\tau = \eta_0(T)\rho/G(\infty)$ is the relaxation time with the density ρ and the high-frequency shear modulus $G(\infty)$. Below a temperature T_x, when τ exceeds the relaxation time of the shear modes in the liquid, the surface spectrum becomes more complex. Besides a modified quasielastic capillary wave spectrum $\tilde{S}(q,\omega)$, Rayleigh surface waves and a continuum of bulk elastic shear waves also occur. At even lower temperatures T_f the average shear stress relaxation time τ exceeds the experimental time scale and the quasielastic part of the fluctuation spectrum is frozen in. Jäckle and Kawasaki identify T_f with the glass transition temperature [39, 59].

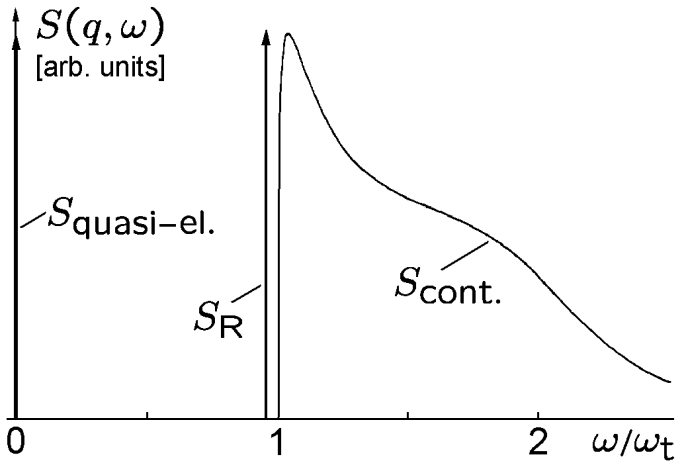

Figure 3.4: Dynamic power spectrum $S(q,\omega)$ of vertical surface height fluctuations of a viscous supercooled liquid around the glass transition [39]. The arrows indicate Lorentzians around the corresponding frequency.

After inserting the frequency dependent viscosity in Eq. 3.9, $\chi(q,\omega)$ depends apart from ω_s on a second frequency $\omega_t = \sqrt{\eta_0/\tau}q$ which is the frequency of the elastic shear modes for long relaxation times τ, i.e. $\omega_t\tau \gg 1$ (quasielastic region). The structure factor of the frozen capillary wave fluctuations is calculated as follows:

$$S(q)_{\text{frozen}} = \frac{k_{\mathrm{B}}T_f}{\gamma(T_f)} \cdot \frac{1}{q^2(1 + ql_0(T_f)/2)}, \tag{3.14}$$

with a length scale parameter $l_0 = \gamma(T_f)/G(\infty)$. The square of the surface roughness below T_f can then be expressed as a sum of a temperature independent frozen-in capillary wave spectrum and a temperature dependent part:

$$\sigma^2(T) = \frac{k_\mathrm{B}T_f}{2\pi\gamma(T_f)} \ln\left(\frac{q_\mathrm{max}(l_0 q_\mathrm{min}+2)}{q_\mathrm{min}(l_0 q_\mathrm{max}+2)}\right) + \sigma'^2(T), \tag{3.15}$$

where $\sigma'^2(T) = \mathrm{const}\cdot T$ accounts for the surface roughness due to Rayleigh surface waves and bulk elastic shear waves. This can be calculated by integrating the dynamic power spectrum of the thermal height fluctuations $S(q,\omega,T)$ (which is given in Ref. [39] for Rayleigh surface waves and bulk elastic shear waves) over all frequencies ω and then integrating over the accessible q range according to Eq. 3.6. The power spectrum $S(q,\omega)$ of the thermal height fluctuations in the quasielastic region is pictured in Fig. 3.4 as a function of ω normalized by the frequency of the elastic shear modes. The quasielastic line at $\omega = 0$ ($S_{\mathrm{quasi-el.}}$) corresponds to the frozen-in capillary waves, and the parts of the spectrum at higher frequencies correspond to Rayleigh surface waves (S_R) and a continuous part for bulk elastic shear waves (S_cont).

3.2 Experimental setup and sample preparation

3.2.1 D8 Advanced laboratory diffractometer

In order to investigate the temperature dependence of the surface roughness given by Eq. 3.15, reflectivity measurements were performed in a wide temperature range with a Bruker D8-Advanced laboratory diffractometer in theta-2theta geometry. This geometry, shown on the right side of Fig. 3.5, is mandatory for scattering on liquid surfaces, because the sample cell cannot be rotated. Therefore, the x-ray tube and the detector have to be rotated around theta (i.e. the incident angle α_i) and 2theta (i.e. incident plus exit angle $\alpha_i + \alpha_f$), respectively. The radiation is emitted from an x-ray tube with a copper anode. Reflection from a parabolically bent multilayer mirror, a so-called Göbel mirror [86], yields a nearly parallel beam with a wavelength $\lambda = 1.54$ Å, corresponding via $E[\mathrm{eV}] = 12398/\lambda[\mathrm{Å}]$ to the energy of the Cu-K$_{\alpha 1}$ line of $E = 8048$ eV. The Göbel mirror also suppresses additional contributions to the spectrum of the x-ray tube like bremsstrahlung and the Cu-K$_\beta$ line. The beam size on the sample is defined by a vertical aperture slit of 0.1 mm height and a horizontal aperture slit of 10 mm width. The primary intensity of this beam is around $I_0 \approx 5\cdot 10^7$ counts/s. An auto-absorber system consisting of four copper foils of varying thickness limits the intensity recorded by the NaI scintillation detector. Between the anti-scattering slit S_S with a vertical

aperture of 0.6 mm and the detector slit S_{D} with a height of 0.2 mm a Soller slit is placed (not shown in Fig. 3.5) which only lets pass parallel beams. The detector slit height and the distance between the detector and the middle of the sample of 300 mm lead to an angular resolution $\Delta\alpha_f = 0.7$ mrad in the scattering plane. The sample cell is placed on a sample stage that can be translated in all three directions in space which is sufficient for the analysis of liquid samples. The sample cell is shown on the diffractometer in Fig. 3.5.

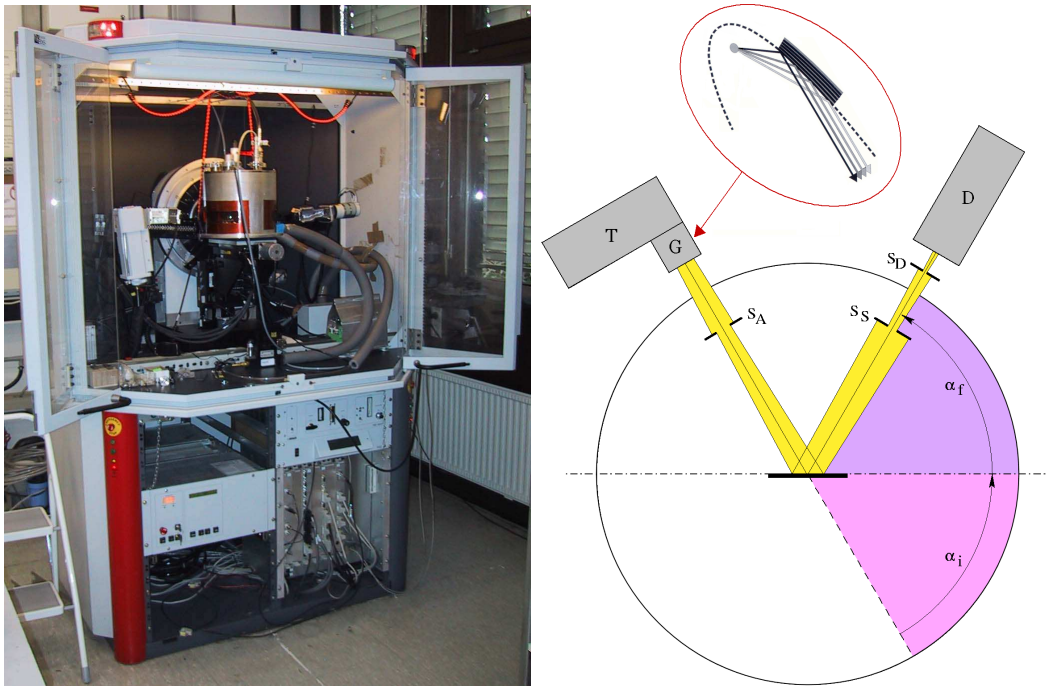

Figure 3.5: Left: Sample cell on the D8 laboratory diffractometer. Right: D8 geometry (T: tube, G: Göbel mirror, D: detector, S_{A}: aperture slits, S_{S}: anti-scattering slit, S_{D}: detector slit, α_i and α_f: incident and exit angle, respectively). The figure on the right is taken from [85, 86] and modified.

3.2.2 Sample preparation and environment

The investigated samples of PPG with an average molecular weight of 400 g/mol were purchased from Alfa Aesar (product number 040811). The chemical formula for PPG is

$$\mathrm{H} - [\,\mathrm{O} - \mathrm{C}(\mathrm{CH_3})\mathrm{H} - \mathrm{CH_2}\,]_n - \mathrm{OH} \tag{3.16}$$

with $n \approx 7$. As the number of repeated subgroups is rather low, the expression oligomer is more precise than polymer for this molecule. According to capillary viscometer

measurements, the viscosity η of PPG-400 should follow the form $\ln\eta = -10.774 + 1047.3\text{K}/(T-168.4\text{K})$, therefore at room temperature the viscosity is $\eta = 0.087$ Pa·s [87]. The surface tension γ was measured by G. T. Dee and B. B. Sauer with the Wilhelmy wetting method, leading to the expression $\gamma = 0.03431\text{N/m} - 8\cdot10^{-5}\text{N/(mK)}\cdot(T-273.15\text{K})$ which yields a surface tension of 0.033 N/m at room temperature [88]. Dielectric spectroscopy measurements for the bulk T_G value of PPG-400 result in $T_\text{G} = 196.4$ K [89].

Figure 3.6: Sample cell for reflectivity and XPCS measurements.

The sample cell used in this experiment is based on a design by T. Seydel et al. [90] and shown in Fig. 3.6. An overview of the experimental setup is outlined in Fig. 3.7. The sample cell consists of two chambers, the outer one is evacuated for thermal insulation, and the inner cell - which is also evacuated to remove residual solvents in the PPG and to minimize air scattering - contains a stainless steel trough (120 mm diameter, 0.2 mm sample height) holding the sample. The large diameter is necessary to minimize effects of surface curvature. The height of the trough is chosen in such way that (*i*) the sample is still deep enough to avoid any influence of the substrate on the surface, and (*ii*) in spite of the volume reduction during cooling, the sample surface is above the rim at all temperatures, thus allowing for measurements around the critical angle of total external reflection. The x-ray beam is penetrating the sample chamber through 50 μm thin Kapton foil windows. The complete sample chamber is placed on a rubber mat for passive vibration damping.

Homogeneous cooling of the sample is achieved by evaporating liquid nitrogen in a heat exchanger underneath the inner sample chamber with a constant flow rate, ensured

by a control valve. The nitrogen inflow for the cooling loop, made of a Delrin isolator, can be seen on the right side in Fig. 3.6 underneath the Kapton window of the outer cell. An electrical resistor connected to a Lakeshore temperature controller heats the sample, providing temperature stability of ±0.02 K. The temperature is measured by two ceramic coated platinum resistor sensors (Pt100) dipped into the liquid sample. With this setup a temperature range from 185 K to 300 K is covered. As can be seen in Fig. 3.7, due to the contact area between the nitrogen cooled inner cell and the isolator underneath, the temperature insulation is not perfect. To avoid condensation from the outside on the Kapton windows (especially at low temperatures), additional heating foils are glued to the outer cell around the Kapton window as shown in Fig. 3.6.

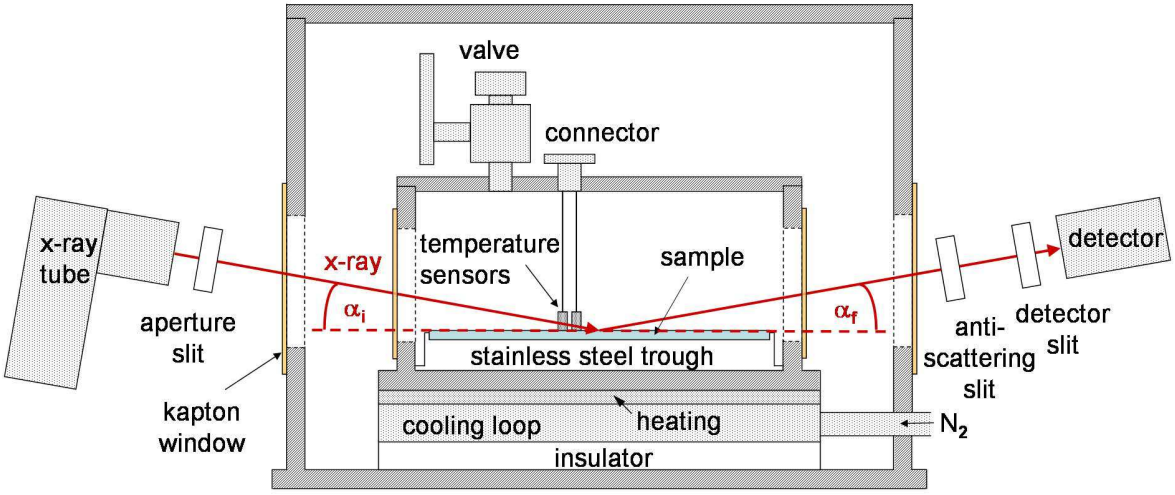

Figure 3.7: Sketch of the experimental setup.

During the reflectivity scans the pressure in the inner cell is monitored by a pressure gauge (1 mbar resolution), measuring a constant pressure of 2-3 mbar. After inserting the sample until its surface is slightly above the rim of the trough, which is possible due to the surface tension causing a meniscus with positive curvature, a waiting time of around 10 h is necessary to form a smooth surface. Then the sample is cooled at a constant rate with an accuracy of $\approx \pm 1$ K/h to the desired temperature, where the measurement is started as soon as T is constant. Due to the limited capacity of 50 l of the nitrogen dewar, at low temperatures only one measurement can be performed before refilling, because a high nitrogen flux is required. The reproducibility of the data is ensured by repeating scans at similar temperatures at later times after heating up to room temperature.

3.3 Reflectivity measurements

3.3.1 Reflectivity for highly viscous samples

As defined in Eq. 2.16, the x-ray reflectivity $R(q_z, T)$ of a liquid-vapor interface is given by [91, 19]

$$R(q_z, T) = R_{\mathrm{F}}(q_z) \exp(-\sigma^2(q_z, T) q_z^2), \tag{3.17}$$

where R_{F} is the Fresnel reflectivity of an ideally smooth surface, and the roughness σ depends apart from q_z now also on the temperature. It should be noted here that in the exact expression for $R(q_z, T)$ an additional term, the so-called incomplete Gamma function $\Gamma[(1-B)/2; A]$ with $A = 2\pi^2 q_{\mathrm{min}}^2/q_{\mathrm{max}}^2$ and $B = k_{\mathrm{B}} T q_z^2/(2\pi\gamma)$ has to be multiplied on the right side of Eq. 3.17 as calculated by T. Ghaderi [7]. It is defined as $\Gamma(x, A) = \int_A^\infty t^{x-1} e^{-t} \mathrm{dt}$ and arises from the integration of the scattering over all wavevector transfers parallel to the surface q_x [54]. However, as the Gamma function is near unity for small values of B, for small T and q_z it can be neglected in this case [7]. If the worst case is considered, i.e. for PPG at the highest investigated temperature of 300 K, the divergence in the Gamma function does not occur for $q_z < 0.67$ Å^{-1}, which is well above the accessible q_z range with a laboratory diffractometer. Thus, for the reflectivity measurements on highly viscous samples presented in this chapter the Gamma function can be set to one.

The reflectivities presented in the following are fitted with the program LSFIT based on the Parratt algorithm using a tanh profile for the index of refraction as explained in subsection 2.2.3.

3.3.2 Experimental results and data analysis

Typical reflectivities measured at the D8 laboratory diffractometer are plotted in the pictures A to E of Fig. 3.8. The solid curves are fits using the Parratt algorithm [16] for which the effective roughness $\sigma(T)$ is independent of q_z. This is a good approximation for σ because it depends only weakly on q_z. The only fit parameters are the dispersion δ and the roughness σ. The absorption β is nearly 500 times smaller than δ as shown in Tab. 2.1. Thus, small changes of β have no influence on the fit. The last picture down to the right shows the square of the roughness obtained from the fit as a function of temperature for three different cooling rates, and the letters A to E correspond to the reflectivity curves in each of the pictures A to E. The corresponding temperature scans for each reflectivity measurement are shown as insets in the pictures A to E. The reflectivity scans are performed in the plateau regions of the temperature curves.

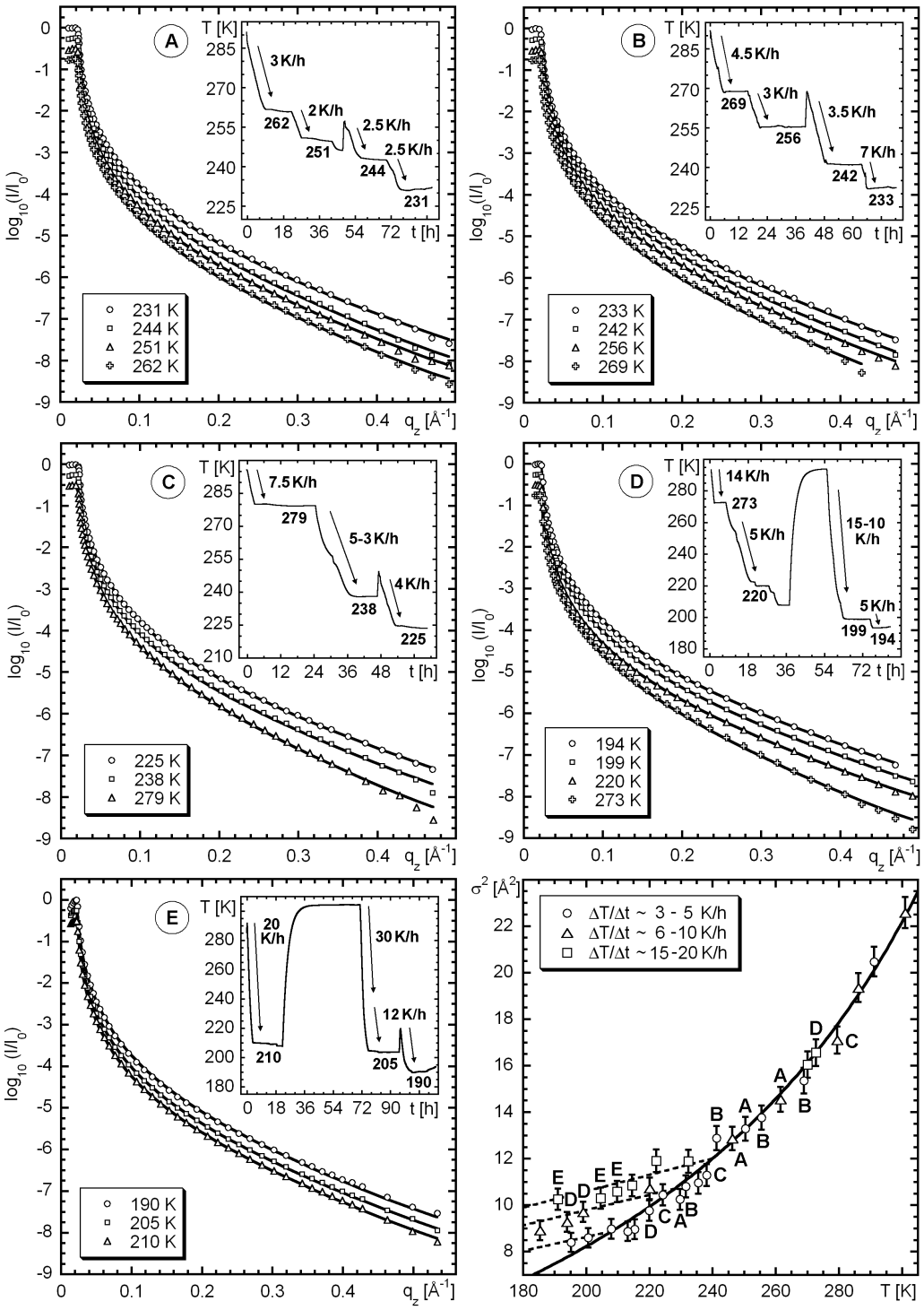

Figure 3.8: Reflectivities with temperature history as insets for different cooling rates. From picture A to E the cooling rate is increased, starting with slow cooling in picture A to slow and medium cooling in B and C, medium and fast cooling in D, and fast cooling rates in E. The last picture summarizes the squared roughnesses obtained from picture A to E as a function of T.

The increase in T after some measurements (see for example picture B of Fig. 3.8 between 256 K and 242 K) is due to refilling of nitrogen which takes about half an hour. Apart from the specular reflected measurements ($\alpha_i = \alpha_f$), additional scans with a constant angular detector offset of 0.1° are subtracted from the reflectivity scans to remove the diffuse background. A typical reflectivity measurement with offset scan is recorded within 6-8 h. In Fig. 3.8 it can be seen that normally three to four measurements at different temperatures are performed during one cooling cycle. Afterwards the sample is heated up again to room temperature in order to achieve thermal equilibrium (see picture D between 220 K and 199 K, or picture E between 210 K and 205 K). This allows to apply a different cooling rate in the following scans because the previous thermal history is erased. It is also important to note that the roughness obtained from the fits can be well reproduced at the same temperature when the same cooling rate is applied after having heated the sample up to room temperature. Furthermore, for temperatures down to around 240 K no difference in the roughness within the error bars can be observed when a reflectivity is repeated after reheating and use of another cooling rate. Hence, the system is still in equilibrium, and at higher temperatures faster cooling rates can be applied in order to save some time. Of this fact could be taken advantage as shown in picture E of Fig. 3.8 where for the second measurement at 205 K a very high cooling rate was applied at the beginning.

Reflectivities for fast cooling rates (for $T \lesssim 240$ K) ranging from around 15 K/h to 20 K/h are summarized in Fig. 3.9 for eight different temperatures. For the highest temperatures also slower cooling rates are included, because the system is still in equilibrium. The solid curves in part A of Fig. 3.9 represent fits using the Parratt algorithm. The curves are shifted vertically for reasons of clarity. It is interesting to note that with decreasing T region for angles smaller than the critical angle (see part B of Fig. 3.9) is not a plateau from the beginning, but decreases for smaller angles due to the volume reduction. This causes the footprint, i.e. the angle under which the planar part of the surface is completely illuminated by the incident beam, to increase. Part C of Fig. 3.9 shows the $\ln R/R_\mathrm{F}$ versus q_z^2 plots of the same data. For this presentation of the data, the square of the roughness can be directly obtained from the slope of the linear fit. For the other cooling rates, similar plots could be obtained.

The temperature dependent square of the roughness is plotted in Fig. 3.10 for all cooling rates. The solid line represents the square of the surface roughness according to Eq. 3.6 assuming a temperature dependence of the surface tension $\gamma(T) = \gamma_0 - A\,(T - 273.15\ \mathrm{K})$ as predicted by Dee and Sauer [88] while the dashed lines represent the expression according to Eq. 3.15. Although the data points for $T > 240$ K in Fig. 3.10

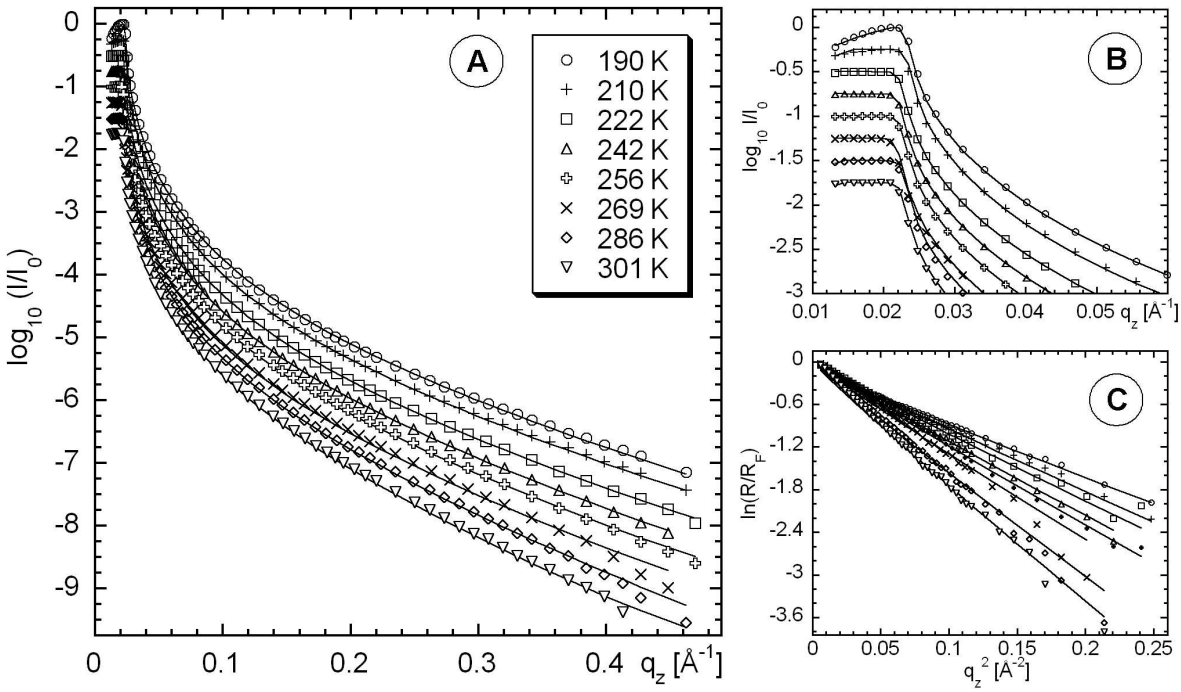

Figure 3.9: (A) Normalized intensity versus q_z for fast cooling rates. The curves are shifted vertically for reasons of clarity. (B) Magnification of the region around the critical angle α_c. (C) Natural logarithm of the same data normalized by the Fresnel reflectivity as a function of q_z^2.

belong to different cooling rates, one single fit is applied, because for $T \gtrsim 240$ K the relaxation is fast enough that no change in the roughness due to different cooling rates can be observed. For low cooling rates the surface roughness follows a liquid-like behavior until close to the bulk T_G value of 196 K. This is in accordance with previous findings from Ref. [61]. However, with increasing cooling rates the temperature dependence of the surface roughness changes. Below a temperature T_f the roughness for high cooling rates is larger than predicted by capillary wave theory. At this temperature the surface fluctuations are falling out of equilibrium and parts of them are frozen in. It should be noted that the surface roughness below T_f still depends on T, i.e. the fluctuations do not freeze completely, even for very high cooling rates. This is in good agreement with the predictions from Jäckle et al. (Eq. 3.15) which are presented as dashed lines in Fig. 3.10. Thus, in the following T_f will be identified as the glass transition temperature T_G.

The glass transition temperature where the surface fluctuations freeze in is estimated from Fig. 3.10. For slow cooling rates the frozen-in state is reached at $T \approx 208$ K whereas at faster cooling rates the glass transition occurs already at higher temperatures

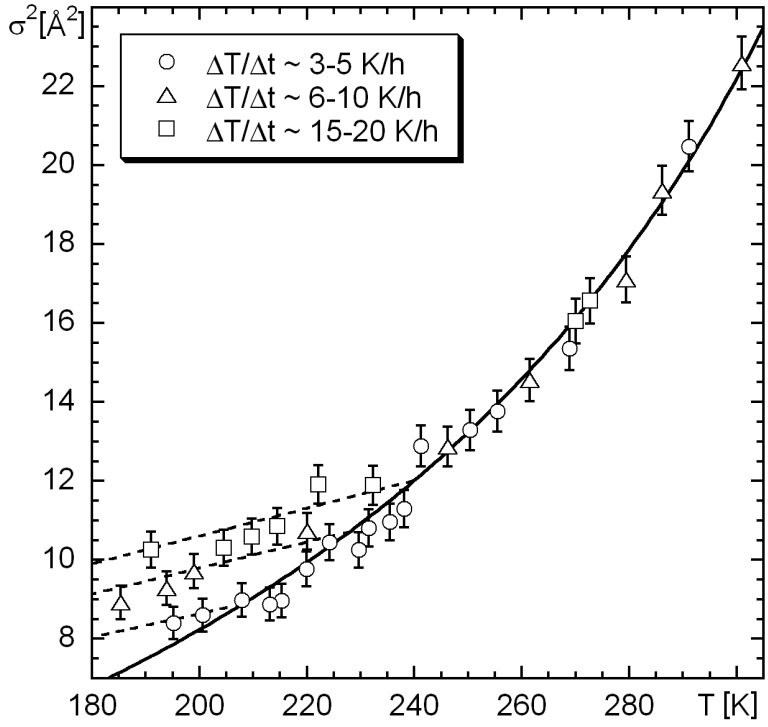

Figure 3.10: Square of the surface roughness as a function of temperature for fast (15-20 K/h, squares), medium (6-10 K/h, triangles) and slow (3-5 K/h, circles) cooling rates. The solid line represents a fit according to Eq. 3.6 for $T >$ 240 K and is extrapolated to smaller T. The dashed lines are calculations according to Eq. 3.15 with a length scale parameter $l_0 = (2000 \pm 1000)$ Å.

($T \approx 228$ K for medium and 240 K for fast cooling). The error in the determination of T_G is estimated as ± 5 K. For the slowest cooling rate it should be noted that due to the limited amount of data points T_G is not well defined, however. Also the error for $l_0 = (2000 \pm 1000)$ Å is rather large, because a small deviation in the slope of the dashed lines results in a large change of l_0. According to Ref. [39], l_0 should be on the order of 1-10 Å. However, x-ray photon correlation spectroscopy measurements on PPG (not yet published) result in similar high values of l_0 of several thousand Å, indicating that $G(\infty)$ may indeed be about a factor 1000 smaller, i.e. on the order of 10^5 Pa, than expected from rheological measurements. This phenomenon will be discussed in the following subsection. It is still a current topic of research if the Maxwell-Debye model used in Ref. [39] is valid or might have to be modified in order to explain the small values of $G(\infty)$ [92].

For the first time, this strong dependence of the glass transition temperature on the cooling rate could be observed on the surface. T_G changes in a broad range, reaching up

to 240 K for the fastest cooling rate compared to 196.4 K in the bulk [89]. In the bulk, the dependence of T_G on the cooling rate is typically rather weak, as it changes only by 3-5 K for a cooling rate variation by an order of magnitude [1, 73]. Mode coupling theory calculations predict a change of T_G of 5 K per decade of the cooling rate [78], which is in good agreement with experiments, e.g. for B_2O_3 in Ref. [77].

It should be stressed here that a complete freezing in of the surface fluctuations cannot explain the data presented in this work. In this case the resolution cutoff q_{min} would depend on an additional summand $q_{visc} = 2\eta(T)/(\gamma(T) \cdot \tau)$ for viscous liquids as calculated in [40, 93]. Due to the exponential increase of the viscosity with decreasing temperature, q_{min} would increase sharply, i.e. more and more smaller length scales would be frozen in. To explain the observed shift of T_G to around 240 K, τ would have to increase enormously. When the glass transition is approached, the viscosity increases so much that the lower wavevector cutoff q_{min} would become larger than the value given by the detector resolution, therefore more and more larger q values would be frozen in. One can then calculate the square of the surface roughness iteratively during cooling of the sample as a sum of a frozen-in part and a still propagating part, where the frozen-in part is composed of a sum of a frozen-in part and a still propagating part at a previous, higher temperature. When this calculation is performed for different relaxation times τ, one finds that in order to reproduce the measured results for the fast cooling rate (with the assumption of complete freezing in of all surface fluctuations) very small values of τ in the ms region are needed. However, x-ray reflectivity measurements at high q values (which are most sensitive to changes in σ) take about 1 h at a laboratory diffractometer, therefore any faster changes cannot be detected. Moreover, as τ is proportional to η, another definition for T_G is the temperature where $\tau = 100$ s which is also much larger than 1 ms. This confirms the observations of a partly freezing of capillary waves which agree with calculations by Jäckle and Kawasaki.

3.3.3 Comparison with x-ray photon correlation spectroscopy

As mentioned in the previous subsection, the length scale parameter l_0 is found to be much larger than expected from theory. However, this phenomenon also occurs in XPCS data measured on PPG with a molecular weight of 4000 g/mol (PPG-4000) with a number of monomer units $n \approx 69$. The measurements were performed by T. Seydel, A. Madsen, C. Caronna, D. Lietz and H. Sternemann and are not published yet. A part of the data has been analyzed within the scope of this work and will be presented now. The two-dimensional XPCS data analysis will be treated in more detail in subsection 4.3.2. The measurements were performed in grazing incidence geometry ($\alpha_i = 0.12°$) with large

exit angles in the plane of incidence at the ID10A beamline of the ESRF at a photon energy of 8 keV (corresponding to a wavelength of $\lambda = 1.55$ Å). The same sample cell as described earlier in subsection 3.2.2 was utilized, and the scattered intensity was recorded by a direct-illumination Princeton CCD camera with 1242×1152 pixels (pixel size of 22.5×22.5 μm^2) at a distance of 2.215 m from the sample. For a temperature of $T = 213$ K, obtained after rather fast cooling[2] to 218 K and then to 216 K, 18000 frames were taken with an exposure time of 0.3 s (plus readout time of about 0.29 s). Fig. 3.11 shows an image extracted from XPCS data of PPG-4000 measured at 213 K. Due to the coherent beam and the short accumulation time, speckles become visible, reflecting the dynamics at the surface. As for an accumulation of only 10 frames the dynamics is still slower than the total accumulation time, the speckles are distinct and not smeared out.

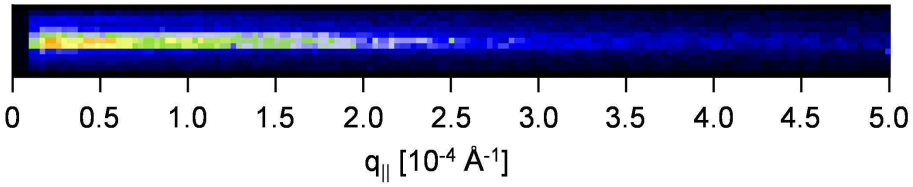

Figure 3.11: CCD images of the coherently scattered intensity from PPG-4000 at 213 K, resulting from adding up 10 frames of 0.3 s accumulation time per frame.

The correlation functions for PPG-4000 at 213 K are presented in Fig. 3.12. Details of the calculation will be described in subsection 4.3.2. As explained in subsection 2.4.3 one has to distinguish between homodyne and heterodyne detection. Normally for small in-plane wavevector transfers $q_{||} = q_x$ on the order of 10^{-4} Å^{-1}, as in the present case, heterodyne detection is expected, which was demonstrated by C. Gutt et al. for propagating capillary waves on water [43]. However, as on highly viscous PPG only overdamped capillary waves occur, it cannot be distinguished between homodyne and heterodyne correlation functions, because they only differ by a factor of two in the relaxation rate Γ. The intensity autocorrelation function for heterodyne detection is given by

$$g_2(q_{||}, \tau) = 1 + \beta(q_{||}) \exp[-\Gamma\tau], \tag{3.18}$$

with the q-dependent contrast $\beta(q_{||})$ in surface XPCS experiments [94]. The decrease of the contrast with increasing $q_{||}$ is clearly visible in Fig. 3.12. For homodyne detection Γ has to be replaced by 2Γ. For the investigated sample of PPG one might argue that the literature values for the temperature dependent surface tension $\gamma(T)$ and viscosity $\eta(T)$ match the slope of the capillary wave model in Eq. 3.19 for small $q_{||}$ better (see dashed line in Fig. 3.13) if heterodyne correlation functions are assumed [92].

[2]Unfortunately, the exact cooling rate was not determined here.

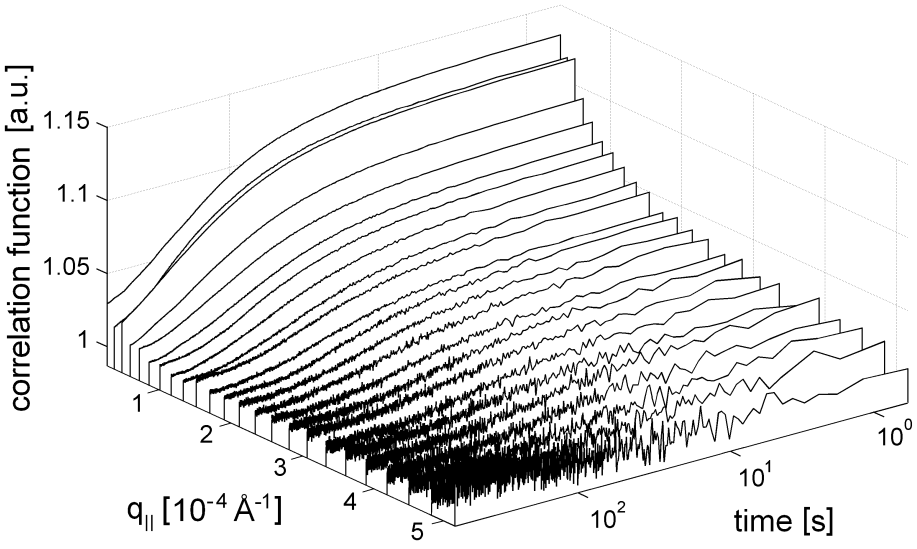

Figure 3.12: Calculated correlation functions $g_2(\tau)$ for PPG-4000 at 213 K.

According to the capillary wave model as summarized in Tab. 3.1, the relaxation rate Γ is proportional to the lateral wave vector transfer $q_{||}$:

$$\Gamma = \frac{\gamma(T)}{2\eta(T)} \cdot q_{||}. \tag{3.19}$$

The viscoelastic theory utilized by Jäckle and Kawasaki [39] predicts the dispersion relation as

$$\Gamma = \frac{\gamma(T)}{2\eta(T)} \cdot \frac{1}{1 + \frac{\gamma(T) q_{||}}{2G(\infty)}} \cdot q_{||}. \tag{3.20}$$

With $l_0 = \gamma(T)/G(\infty)$ and $\tau = \eta(T)/G(\infty)$ this expression can be transformed into

$$\Gamma = \frac{1}{2\tau} \cdot \frac{q_{||} l_0}{1 + \frac{1}{2} q_{||} l_0}. \tag{3.21}$$

The dispersion relation can therefore be fitted with the two parameters l_0 and τ. Fig. 3.13 presents the relaxation rate Γ as a function of the lateral wave vector transfer $q_{||}$. Only for small $q_{||}$ the data might be represented by the linear capillary wave model as indicated by the dashed line. A much better description of the data is given by the viscoelastic theory applied by Jäckle and Kawasaki. The resulting fit parameters are $l_0 = (6200 \pm 700)$ Å and $\tau = (77 \pm 4)$ s. It might be noted that one definition of the glass transition is the temperature at which τ exceeds a value of 100 s. Thus, with this definition the liquid should not have reached the glassy state yet. Nevertheless, the length scale parameter l_0 is on the same order of magnitude as obtained from reflectivity scans which confirms the measurements presented in the previous subsection.

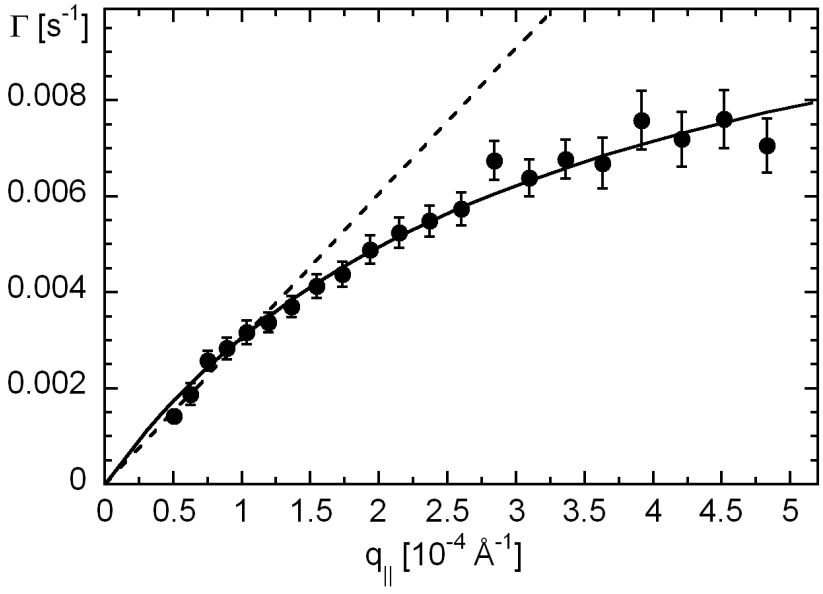

Figure 3.13: Dispersion relation (relaxation rate Γ versus $q_{||}$) for PPG-4000 at 213 K. The dashed line is a linear fit of the first six data points, whereas the solid line represents a fit according to the theory of Jäckle and Kawasaki.

3.4 Summary and discussion

To summarize, in section 3.3 cooling rate dependent x-ray reflectivity measurements performed on PPG with a molecular weight of $M_w = 400$ g/mol are discussed to determine if overdamped capillary waves still occur on the surface or if they are frozen in around the glass transition and how they are influenced by the cooling rate. A strong dependence of the roughness on the cooling rate is observed, indicating that capillary waves are partly frozen in already at higher temperatures than for slow cooling. From this frozen-in roughness the glass transition temperature at the surface can be estimated. A high shift from the bulk T_G value of 196.4 K up to around 240 K at the surface for fast cooling rates is observed. It could be shown that in-situ determination of the surface tension of highly viscous liquids is possible, which is difficult with standard techniques due to long relaxation times. The theory of viscoelasticity used by Jäckle and Kawasaki to calculate the spectrum of thermal height fluctuations on the surface of supercooled liquids is well suited to describe the reflectivity data [39, 59]. An essential point in this chapter is the cooling rate dependence of the glass transition, which is known in the bulk, but has never before been seen at the surface. This fundamental result is also of practical interest, as it is now possible to predict a specific cooling rate which will be acceptable for a desired roughness.

Another interesting phenomenon is that much larger values for the length scale parameter l_0 on the order of several thousand Å compared to viscoelastic theory (1-10 Å) are found, which is confirmed by XPCS measurements on PPG-4000. As a result, the high-frequency elastic shear modulus $G(\infty) \propto l_0^{-1}$ is several orders of magnitude smaller than the macroscopic value obtained from rheology measurements. This indicates that the simple Maxwell-Debye model for the frequency dependent viscosity as introduced in Eq. 3.13 might have to be modified in order to fully describe the data. Furthermore, additional XPCS experiments performed by A. Madsen et al. on PPG-2000 (unpublished yet) indicate that a linear progression of the dispersion relation $\Gamma(q_{||})$ is already at smaller $q_{||}$ values than for PPG-4000 not valid anymore. The form of the dispersion relation and its theoretical description are currently not understood.

It should also be stressed here that the glass transition at the surface exhibits important differences to the one in the volume. The dynamics of glass-forming liquids in the bulk are typically characterized by α- and β-relaxation processes. The glass transition temperature can be defined by the value $\tau = 100$ s of the relaxation time of the α-relaxation. Another prominent feature in the volume is the existence of a nonergodic level f_q in the correlation functions as explained in subsection 3.1.1: The dynamic structure factor is found to decay not completely to zero, but to a plateau f_q. However, these properties are not known at the surface. The correlation functions at the surface as observed by XPCS always decorrelate completely. One might argue that with XPCS a kind of surface-α-relaxation can be observed, but this is not a real analogon to the bulk because at surfaces new hydrodynamic modes like capillary waves exist. Furthermore, for XPCS measurements only partial coherence is available, therefore the contrast is smaller than one. This can be seen in Fig. 3.12 where the maximal contrast is only about 0.13. Thus, it is difficult to determine whether the initial value of the correlation function is determined by a possible nonergodic level or solely due to the contrast. However, R. Bandyopadhyay et al. have shown that the de-Gennes narrowing (see subsection 3.1.1), connecting a minimum of the relaxation rate with the maximum of the static structure factor (which is also associated with a maximum of f_q), is not observed for laponite clay systems [95]. This insensitivity of τ to the interparticle correlations is a clear indication that the slow dynamics which are observed by XPCS are not connected with collective diffusion in bulk glassy systems.

To summarize, within the scope of this chapter it could be demonstrated that a substantial difference consists between the freezing in of density fluctuations in the bulk and at the surface. For the first time, a much larger shift of the glass transition temperature than known in the volume could be probed at the surface.

4 Two-dimensional dynamics of metal-polymer nanocomposites

Composite systems of metallic nanoparticles dispersed in and on polymeric materials are of great interest from both technological and fundamental aspects, as their fine control and design lead to the fabrication of materials with novel electronic, magnetic or catalytic properties [96]. These composite materials are often formed out of equilibrium inducing ordering and coalescence processes of the metal clusters [97, 98]. As the technological properties of these materials depend on the structure and ordering of the metal nanoparticles a detailed understanding of the dynamic processes involved is desirable. Moreover, nonequilibrium systems often display dynamics which are more complex than, e.g., the simple Brownian diffusion. Currently, there is considerable interest in nonequilibrium bulk soft matter systems like, e.g., clay suspensions [95], colloidal gels [99], or concentrated emulsions [100], which all show aging phenomena and a peculiar universal form of the dynamic structure factor. In two dimensions, particle motion only occurs within a layer parallel to the surface. This 2D case, which often displays rich physical phenomena, is more difficult to study as it requires a surface sensitive technique able to probe the dynamics at the nanometer scale. In this context, x-ray photon correlation spectroscopy (XPCS) is a well-suited technique [101, 94]. The main advantage of using x-rays instead of methods like scanning probe microscopy is that averaged statistical information over the whole sample surface is obtained, which is essential for the analysis of aging effects. This chapter presents studies of the dynamic structure factor $f(q_{||}, \tau)$ with the relaxation time τ at lateral wave vector transfers $q_{||}$ using grazing-incidence enhanced-intensity XPCS at the maximum of the static scattering factor. With this technique for the first time 2D surface dynamics of colloids at nanometer length scales could be probed. The obtained results are supported by a recent publication of S. Narayanan et al. in which the same behavior of $f(q_{||}, \tau)$ is found for a similar system [102].

4.1 Theoretical background

4.1.1 Characteristics of amorphous polymers

A polymer is a macromolecule consisting of many chemically identical covalent bonded units, so-called monomers. The polystyrene molecule $[C_8H_8]_n$ employed in this work is shown in Fig. 4.1. If the monomer units are considered in three dimensions, one notices that the phenyl side groups can be ordered in many different ways along the chain direction. If all side groups extend in the same direction, the steric order is defined as isotactic, whereas for an atactic polymer the side groups are ordered arbitrary. Alternating regularly ordered side groups form a syndiotactic polymer [103]. For the measurements presented in this work, atactic polystyrene has been used which cannot crystallize.

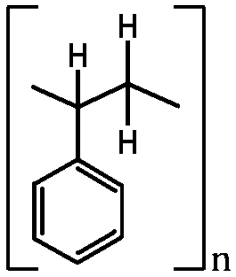

Figure 4.1: The polymer polystyrene (PS). n denotes the number of monomer units.

The fabrication of polymers produces chains with different lengths and therefore different molecular weights of the polymers. The variation of the chain lengths is described by a molecular weight distribution. Depending on the fabrication process these distributions have different shapes and widths, which strongly influences the thermal and mechanical properties of the polymer. For radical polymerization very broad distributions (Schulz-Flory distribution) arise, whereas for anionic polymerization the narrower Poisson distribution is obtained [103]. The polymerization processes are described in detail in Ref. [103]. Depending on the reaction mechanism, a different molecular weight distribution $p(M)$ with the mass M of a chain molecule occurs. With the normalization $\int p(M)dM = 1$ one obtains the number average

$$M_{\mathrm{n}} = \int M p(M)\, dM \tag{4.1}$$

and the weight average

$$M_{\mathrm{w}} = \frac{1}{M_{\mathrm{n}}} \int M^2 p(M)\, dM. \tag{4.2}$$

With the so-called inconsistency value

$$U = \frac{M_\mathrm{w}}{M_\mathrm{n}} - 1 \tag{4.3}$$

information about the molecular mass distribution is obtained. Normally, industrial polymers possess a broad mass distribution with $10 \lesssim U \lesssim 50$, whereas $U \approx 0.02$ for anionic polymerization, which is the case for the polystyrene employed for this work [103].

It is also of interest to determine the size of a polymer molecule. If the detailed structure of the molecule can be neglected when probing a larger length scale, the polymer can be described by a long, winding chain. Depending on the structure of the molecule, single chain segments are not completely flexible, but exhibit a certain rigidity due to side groups inhibiting the motion. The rotatability of the chemical bonds allows for a variety of conformations. The most probable one is a clew structure [104]. This structure can be characterized by the mean end-to-end distance R defined by [104]

$$\langle R \rangle^2 = C_\infty \cdot N a_b^2 \tag{4.4}$$

with a bond length a_b between the atoms of the main chain and the number N of C-C bonds in the main chain, i.e. for polystyrene two times the number of monomer units. C_∞ is the so-called characteristic proportion, experimentally determined as 10.2 for polystyrene. For large N a simple relation between R and the radius of gyration R_g can be found [105]:

$$R_\mathrm{g}^2 = \frac{1}{6} R^2. \tag{4.5}$$

R_g describes the square root of the mean squared distance of all main chain atoms from the center of mass of the molecule. For a molecular weight of $M_\mathrm{w} = 34.4$ kg/mol, the number of monomer units and the radius of gyration are given as $n \approx 330$ and $R_\mathrm{g} = 51.6$ Å, and for $M_\mathrm{w} = 220$ kg/mol they are $n \approx 2115$ and $R_\mathrm{g} = 130.6$ Å [106].

According to the classification of glasses introduced in section 3.1.1, polymers are the most fragile liquids, therefore their viscosity behaves according to a Vogel-Tammann-Fulcher law as defined in Eq. 3.2. For polymers the viscosity η also depends on the shear rate $\dot{\gamma}$ and the molecular weight M_w as illustrated in Fig. 4.2. For Newtonian liquids the shear stress s is proportional to the shear rate $\dot{\gamma}$ (i.e., $s = \eta\dot{\gamma}$). However, for polymers this behavior is not valid, and the viscosity depends on the shear rate as shown in the left part of Fig. 4.2. For small $\dot{\gamma}$ the viscosity remains constant: $\eta = \eta_0$, but when a certain shear rate is exceeded, η decreases. This phenomenon is due to the chain structure of the molecules. For sufficiently long chains, loops and entanglements can occur in the polymer melt, and for large shear rates they can be untied which reduces the viscosity.

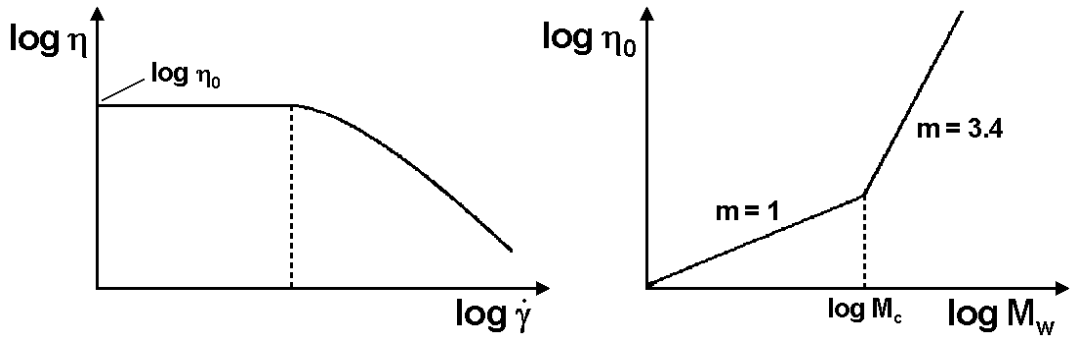

Figure 4.2: Dependence of the viscosity on the shear rate (left) and the molecular weight (right). η_0 denotes the viscosity for low shear rates. Figure taken from [106].

These entanglements are also responsible for the dependence of η_0 on the molecular weight M_w, scaling as $\eta_0 \propto M_\mathrm{w}^m$, which is displayed in the right part of Fig. 4.2. Below a critical molecular weight M_c the polymer chains are too short for entanglements. For $M_\mathrm{w} > M_\mathrm{c}$, the fluidity of the molecules is strongly inhibited, manifested by a faster increase of η_0. At the so-called entanglement molecular weight $M_\mathrm{e} \approx 18$ kg/mol [107] the polystyrene chain is long enough for the two ends to touch each other, but only after reaching the critical molecular weight $M_\mathrm{c} \approx M_\mathrm{e} \approx 35$ kg/mol [108] entanglement effects occur [109].

Another important parameter for the characterization of polymers in the context of x-ray scattering is the surface tension γ. The temperature dependence of the surface tension can be calculated in the context of the molecular field approximation for a lattice model of the liquid as $\gamma(T) \propto (1 - T/T_\mathrm{c})^\kappa$ with the exponent $\kappa \approx 1.25$ derived from experiments [106, 110]. Therefore, γ decreases to zero according to a power law when the critical temperature T_c is approached. C. I. Poser and I. C. Sanchez expanded this theory for polymers and found for atactic polystyrene with long chains [111, 112]:

$$\frac{\gamma(T)}{0.109\,\mathrm{N/m}} = 0.6109 - 0.6725\,\frac{T}{735\,\mathrm{K}} + 0.1886\left(\frac{T}{735\,\mathrm{K}}\right)^2. \tag{4.6}$$

In the region between room temperature and 420 K the surface tension for polystyrene decreases nearly linearly from 0.04 N/m to 0.03 N/m.

4.1.2 Polymer-metal interfaces

For the evaporation of metal on polymer surfaces Volmer-Weber growth is the dominating process [113] as long as the deposited amount of metal is small enough [106]. However, no typical values for the amount of material are given in Ref. [113] to illustrate how small is small, but it is known that the surface tension of gold is almost two

orders of magnitude higher than that of polystyrene. Therefore, the interaction between Au/Au is much larger than that of Au/PS. Thus, the metal atoms rearrange themselves as small islands and in the ideal case spherical clusters form. To understand the embedding process, the reduction of the Gibbs free energy due to embedding of a metal cluster with the radius r_c into the depth d is considered as illustrated in Fig. 4.3 [106].

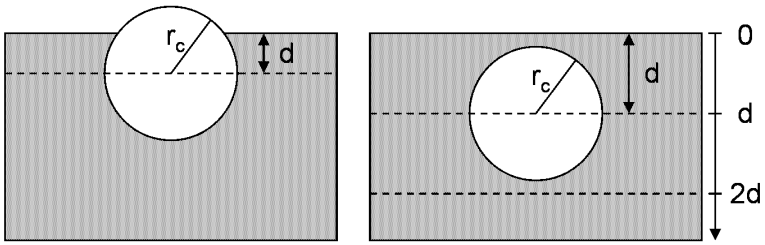

Figure 4.3: Schematic representation of a spherical gold cluster with the radius r_c being partially (left) or completely embedded (right) into the polymer. d denotes the embedding depth with respect to the cluster center.

It has to be noted here that the associated experimental works by G. J. Kovacs and P. S. Vincett show clusters on the size of several hundred nm [114, 115, 116], whereas the samples investigated in this work contain much smaller gold clusters with a radius of around 2 nm. Although it has not been proven yet whether the model explained in the following is also valid for such small clusters, the considerations of R. Weber, who also investigated nanometer sized clusters, will be pursued in the following [106].

Apart from the contribution of the free polymer surface, the cluster contributes an additional proportion $G_c(d)$ to the free energy due to the interface [106]:

$$G_c(d) = \underbrace{2\pi r_c(r_c + d)\gamma_{mp}}_{\text{embedded cluster part}} + \underbrace{2\pi r_c(r_c - d)\gamma_m}_{\text{protruding part}} - \underbrace{\pi(r_c^2 - d^2)\gamma_p}_{\text{surface reduction}} \tag{4.7}$$

for partial embedding of the cluster $|d| \leq r_c$. The first summand describes the contribution of the embedded part of the cluster with the interface tension γ_{mp} between the metal and the polymer, the second summand accounts for the contribution of the part of the cluster which protrudes out of the polymer with the surface tension of the metal γ_m. The last summand includes the reduction of the polymer surface due to the presence of the cluster with the surface tension of the polymer γ_p. The surface tension for solids can be understood as a surface energy per area. For a completely embedded cluster ($d > r_c$) this expression has to be constant according to $G_c = G_c(r_c) = 4\pi r_c^2 \gamma_{mp}$, and for a cluster which is outside the polymer ($d < r_c$) it follows as $G_c = G_c(-r_c) = 4\pi r_c^2 \gamma_m$. The interface fraction of the Gibbs free energy is therefore constant for $|d| \leq r_c$ and parabolic for the intermediate region. For gold clusters on polystyrene, $\gamma_m > \gamma_p$, therefore at

least a partial embedding of the clusters is expected. Complete embedding occurs if the inequality [115, 116]

$$\gamma_{\mathrm{m}} > \gamma_{\mathrm{p}} + \gamma_{\mathrm{mp}} \tag{4.8}$$

holds. In this case, $G_{\mathrm{c}}(d)$ is strictly monotonic decreasing in the parabolic region. G. J. Kovacs and P. S. Vincett have found that only a few organic materials exhibit partial embedding, whereas for all metals complete embedding is energetically preferred [115, 116].

The surface tension of polystyrene can be calculated according to Eq. 4.6, and the surface tension of gold is given by [117]

$$\gamma_{\mathrm{Au}} = 1.185\,\frac{\mathrm{N}}{\mathrm{m}} - 2.5 \cdot 10^{-4}\,\frac{\mathrm{N}}{\mathrm{mK}}(T - T_{\mathrm{m,Au}}) \tag{4.9}$$

with the melting temperature of gold $T_{\mathrm{m,Au}} = 1337$ K. The interface tension between gold and polystyrene was estimated by F. M. Fowkes as [118]

$$\gamma_{\mathrm{mp}} = \gamma_{\mathrm{m}} + \gamma_{\mathrm{p}} - 2\sqrt{\gamma_{\mathrm{m}}^{\mathrm{d}}\gamma_{\mathrm{p}}^{\mathrm{d}}}. \tag{4.10}$$

According to [118] the surface tension of a metal is expressed by two summands, $\gamma_{\mathrm{m}} = \gamma_{\mathrm{m}}^{\mathrm{d}} + \gamma_{\mathrm{m}}^{\mathrm{m}}$, where $\gamma_{\mathrm{m}}^{\mathrm{d}}$ denotes the so-called dispersion part and $\gamma_{\mathrm{m}}^{\mathrm{m}}$ a metallic contribution, whereas polymers only possess a contribution due to dispersion forces $\gamma_{\mathrm{p}}^{\mathrm{d}} = \gamma_{\mathrm{p}}$. If the temperature dependence of the surface tension is neglected, the dispersion part of the surface tension can be estimated for gold according to $\gamma_{\mathrm{m}}^{\mathrm{d}} = A/(24\pi r_{\mathrm{Au}}^2)$ [106] with the Hamaker constant $A = 4 \cdot 10^{-19}$ J [119] and the atomic radius $r_{\mathrm{Au}} = 1.44$ Å. One obtains $\gamma_{\mathrm{m}}^{\mathrm{d}} \approx 0.26$N/m which can be inserted in Eq. 4.10. For complete embedding of a gold cluster the gold-polystyrene system gains an energy of

$$\Delta G_{\mathrm{c}} = G_{\mathrm{c}}(-r_{\mathrm{c}}) - G_{\mathrm{c}}(r_{\mathrm{c}}) = 4\pi r_{\mathrm{c}}^2(\gamma_{\mathrm{m}} - \gamma_{\mathrm{mp}}). \tag{4.11}$$

For gold clusters with a radius of $r_{\mathrm{c}} = 10$ Å the energy gain is $\Delta G_{\mathrm{c}} = 13$ eV per cluster while for $r_{\mathrm{c}} = 25$ Å one obtains $\Delta G_{\mathrm{c}} = 81$ eV per cluster [106].

After complete embedding of a gold cluster, the surface tension has no influence on reducing the Gibbs free energy anymore. However, the free energy of the system can be influenced by weaker effects. According to [114], apart from the large free energy change ΔG_{c}, two smaller contributions occur which vary with the depth of the cluster below the surface. The first one, ΔG_{VdW}, represents the Van-der-Waals attraction between the metal sphere and the half-space of the polymer which pulls the cluster deeper into the polymer. As shown in the right part of Fig. 4.3, due to geometrical reasons, the Van-der-Waals forces in a layer between the polymer surface and the plane indicated

by the dashed line at $z = 2d$ cancel out each other. Only the forces in the half-space below yield a non-vanishing contribution. The second contribution, the entropic energy $-T\Delta S$, tends to reject the clusters. It should be noted that gravitational effects can be neglected for the complete embedding process. The total change of the Gibbs free energy is therefore given by [114]

$$\Delta G = \Delta G_{\mathrm{c}} + \Delta G_{\mathrm{VdW}} - T\Delta S. \tag{4.12}$$

Taking into account all contributions for different cluster sizes and temperatures, the gold clusters do not penetrate deep into the polymer, but remain in a near surface region. Due to the attractive Van-der-Waals interaction between the clusters, the gold layer is stabilized in a narrow height region. It can be shown theoretically and experimentally that the density distribution of the gold particles follows a Gaussian form in z direction [106]. R. Weber has measured the density profile for gold clusters on polystyrene with molecular weights between 3.7 kg/mol and 212 kg/mol with nominal thicknesses of the gold layer between 4 Å and 16 Å. The gold clusters stay at a depth of around 40 Å below the surface with a distribution width of around ±10 Å. During heating up to around 420 K for small clusters this depth increases to about 50 Å and the width of the distribution also increases slightly. However, large clusters with nominal thicknesses of 16 Å are found to stay in the same surface region for all temperatures. This absence of embedding is explained by the high gold coverage for which more agglomerates than isolated clusters are expected [106].

4.1.3 Aging phenomena in out-of-equilibrium systems

Aging is a quite general phenomenon which happens in a wide variety of materials which are out of equilibrium such as glasses, colloidal gels, clay suspensions, or concentrated emulsions [95, 99, 100]. It affects mechanical, magnetic, rheological, and other properties of materials. Apart from potential industrial applications, it is of great scientific interest to understand the principal mechanisms for aging.

Aging can be most directly assessed by measuring the change in the sample dynamics. For aging systems it is typical that the dynamic structure factor $f(q_{||}, \tau)$ of the cluster motion exhibits a faster than exponential decay: $f(q_{||}, \tau) \propto \exp[-(\Gamma\tau)^{\alpha}]$ with the relaxation rate Γ and the exponent $\alpha > 1$. L. Cipelletti et al. proposed a model for this peculiar form of the dynamic structure factor [99, 100, 120] which is based on long ranging displacement fields induced by the particle motion. The movement of particles causes a strain field in the surrounding polymer matrix which enables also other particles

to move. This behavior represents a ballistic (or hyperdiffusive) instead of diffusive particle motion. J.-P. Bouchard and E. Pitard showed that this model leads to an exponent $\alpha = 3/2$ and a dispersion $\Gamma \propto q_{||}$ under the condition that the experimental time scale is much smaller than the typical coalescence time. They explain the form of the dynamic structure factor with localized microcollapses (due to the relaxation of randomly distributed, internal stress sources) which create a long-range elastic deformation field that is responsible for the behavior of the dynamic structure factor with an exponent of $\alpha = 3/2$ [121].

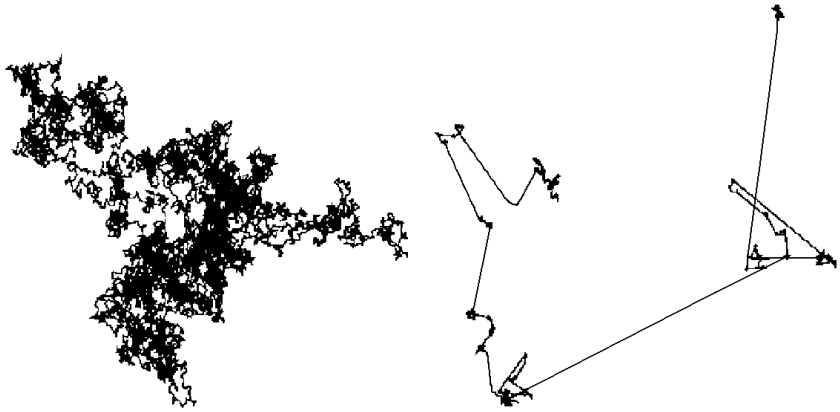

Figure 4.4: Brownian motion (left) and ballistic motion due to Lévy flights (right) [122]. The lines represent the path of a particle.

Moreover, aging systems typically display a power law distribution of the particle velocities, in contrast to the normal Gaussian distribution for diffusion. In Fig. 4.4 the difference between ordinary diffusion and hyperdiffusive or ballistic motion is shown. The picture shows on the left side ordinary random walk or Brownian motion, and on the right a Lévy flight trajectory typical for ballistic motion. For Brownian motion, the relaxation rate Γ (defined as the inverse relaxation time τ) is proportional to q^2, whereas for Lévy flights the relaxation rate depends linearly on q, and the jumps of the particles are distributed according to a power law. The distance $X(t)$ after the time t for ordinary diffusion is proportional to $t^{1/2}$. For a Lévy flight it is given by $X(t) \propto t^{1/\beta}$ with $0 < \beta < 2$.

Lévy flights are random processes that can be described by a probability distribution with long tails. Therefore, jumps over large distances have a rather high probability compared to the normal Gaussian distribution. Lévy flights model dynamics that involve a lot of small steps which are occasionally interrupted by very large steps. Examples are hide-and-seek games [123] or foraging paths of some deer, because in complex ecosystems there are normally some large areas without food, and to avoid spending too much time

there, the animals have developed search strategies including larger paths. Another example is given by human travel which has been recently analyzed by the circulation of bank notes in the USA [122]. For the measurements presented in this work, the dynamics is due to stress relaxation. Here a good example is given by earthquakes where suddenly large relaxations can occur while over years or centuries only small motions are registered.

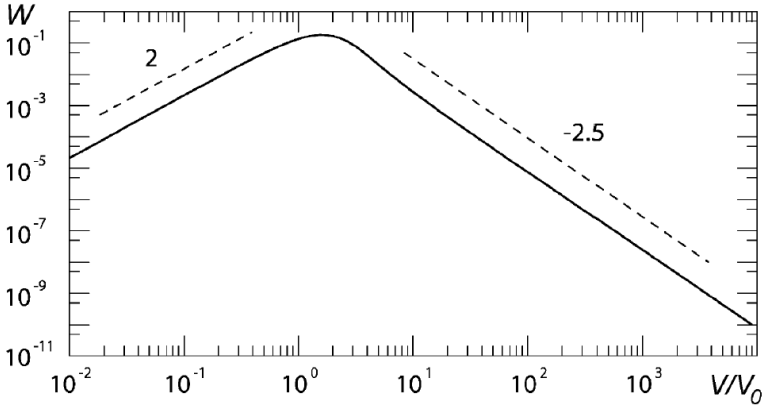

Figure 4.5: Velocity distribution $W(v)$ calculated from the Lévy law $L_{\alpha,0}(v/v_0)$ for a compressed exponent $\alpha = 3/2$ [100]. For velocities v much larger than the mean particle velocity v_0, $W(v) \propto (v/v_0)^{-2.5}$ as indicated by the dashed line on the right, whereas for $v < v_0$ the velocity distribution follows as $W(v) \propto (v/v_0)^2$.

A connection between ballistic motion due to Lévy flights and the particle velocity v is given in [120, 100]. For ballistic motion the final decay of the dynamic structure factor $f(q_{||}, \tau)$ solely depends on the product $x = q_{||} \cdot \tau$ (not on $q_{||}$ and τ separately) and on $\Gamma \propto q_{||}$. $f(q_{||}, \tau) = f(x)$ can then be expressed by $f(x) = \exp[-(xv_0)^\alpha]$ with a mean particle velocity $v_0 = \Gamma/q_{||}$. The linear dispersion relation $\Gamma \propto q_{||}$ rules out diffusion, because in this case Γ would depend on $q_{||}^2$. The shape of $f(x)$ depends on the velocity distribution function $P(\vec{v})$ of the moving particles in three dimensions via [41]

$$f(x) = \int \vec{v} P(\vec{v}) \exp(i\vec{x} \cdot \vec{v}) d^3\vec{v}. \tag{4.13}$$

By using polar coordinates and integrating over the angular variables, one obtains

$$f(x) = \int_0^\infty 4\pi v^2 P(\vec{v}) \frac{\sin(xv)}{xv} dv = \int_0^\infty W(v) \frac{\sin(xv)}{xv} dv. \tag{4.14}$$

The probability distribution for the modulus of the particle velocity $W(v)$ can then be calculated by a Fourier sine transformation as

$$W(v) = \frac{2v}{\pi} \int_0^\infty x f(x) \sin(xv) dx. \tag{4.15}$$

This equation has been long known in literature, e.g., for measuring the velocity distribution of E. Coli bacteria where $f(x)$ is also called the intermediate scattering function [124]. $f(x)$ is the Fourier transform of the Lévy stable law $L_{\alpha,0}$ defined by [125]

$$L_{\alpha,0}\left(\frac{v}{v_0}\right) = \frac{v_0}{\pi}\int_0^\infty f(x)\cos(xv)dx. \tag{4.16}$$

A comparison of the two last equations shows that $W(v)$ is proportional to the derivative of $L_{\alpha,0}$:

$$W(v) = -\frac{2v}{v_0}\frac{d}{dv}L_{\alpha,0}\left(\frac{v}{v_0}\right). \tag{4.17}$$

As the Lévy stable law is characterized for large velocities by a power-law distribution of the particle velocities, $L_{\alpha,0}(v/v_0) \propto (v/v_0)^{-(\alpha+1)}$, the velocity distribution function follows as

$$W(v) \propto \left(\frac{v}{v_0}\right)^{-(\alpha+1)} \tag{4.18}$$

as plotted in Fig. 4.5. From measurements of the dispersion relation, i.e. the relaxation rate Γ as a function of the lateral wavevector transfer $q_{||}$, the mean particle velocity for which $W(v)$ exhibits a maximum can be calculated as $v_0 = \Gamma/q_{||}$.

4.2 Experimental layout and sample preparation

4.2.1 Experimental station ID01 at the ESRF

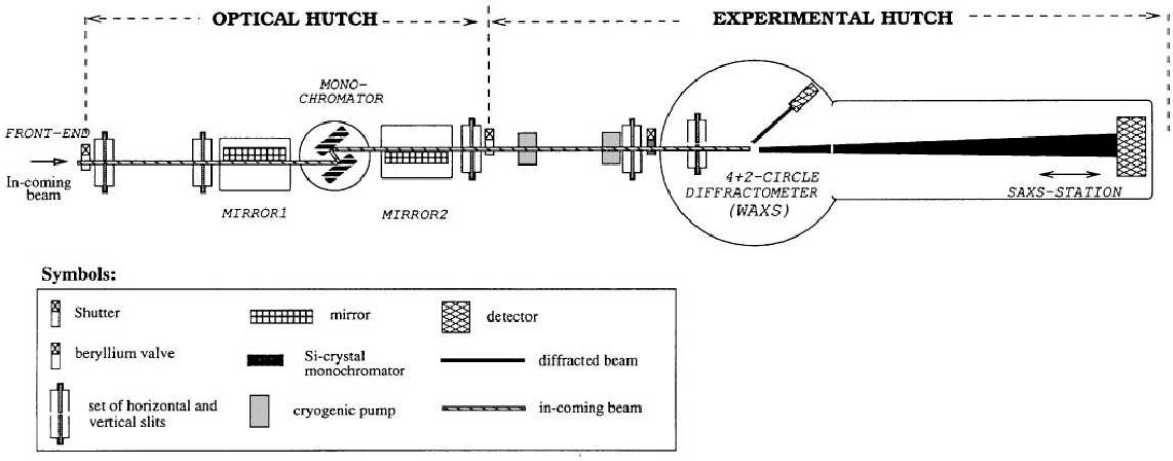

Figure 4.6: Schematic layout of the ID01 beamline [126].

Grazing incidence small angle x-ray scattering experiments were performed by V. Chamard et al. at the ID01 beamline at the European Synchrotron Radiation Facility (ESRF) in Grenoble. The ID01 is specialized for anomalous scattering experiments, i.e. diffuse scattering experiments near an element's absorption edge. The setup of the beamline is presented in Fig. 4.6.

The insertion device positioned in a straight section of the ESRF storage ring consists of a wiggler with a magnetic period of 70 mm and an undulator with a 42 mm period length [127]. In the optical hutch an Si(111)-double-crystal monochromator (cooled with liquid nitrogen) is located between two mirrors. The x-ray beam coming from the source passes through primary and secondary slits before being deflected by a cooled mirror, creating an almost parallel beam. Then the double-crystal monochromator provides a fixed-exit monochromatic beam and maintains a constant focal spot during energy tuning. The available photon energy range between 2.1 keV and 35 keV with an energy resolution of $\Delta E/E = 10^{-4}$ allows to probe the emission lines of a large number of different chemical elements. A beam-stop after the monochromator intercepts the white beam and the bremsstrahlung. Afterwards a second mirror focuses the monochromatized beam meridional and rejects the higher harmonics. After passing another pair of slits, the beam enters the experimental hutch through a shutter.

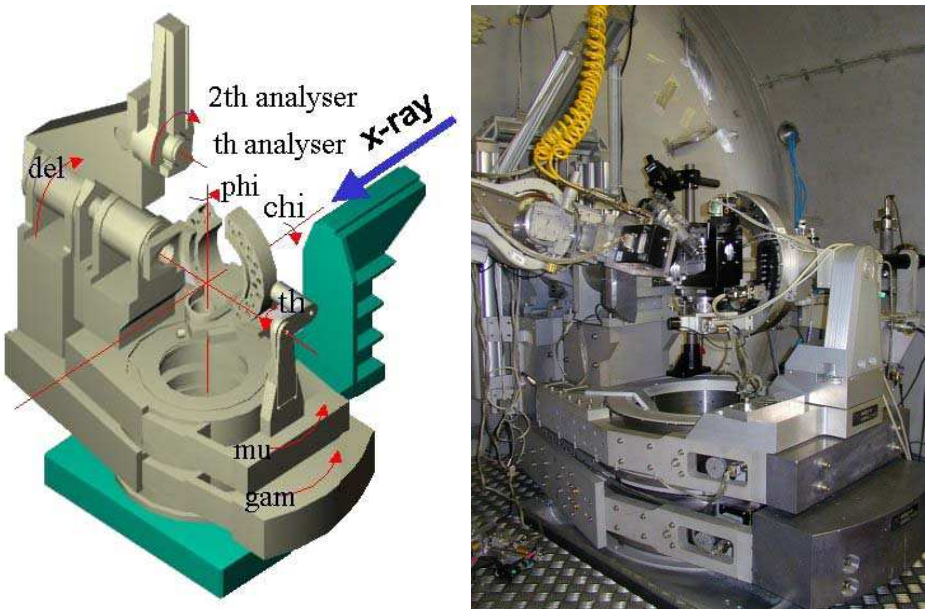

Figure 4.7: Diffractometer at the beamline ID01 [128].

The 2+4-circle diffractometer with the 2-circle analyzer stage in the experimental hutch is shown in Fig. 4.7. It is located in a large evacuable vessel (3.4 m diameter) for vertical or horizontal bulk or surface scattering experiments. The detector can move

in the vertical plane (angle "del") and horizontal plane (angle "gam"). A detailed description of the other motors shown in Fig. 4.7 is given in [128]. For the incoherent GISAXS measurements presented in this chapter a 2D undirect-illumination CCD detector is placed on the track. The distance between the CCD and the sample can be varied between 1.2 m and 3 m (and could be increased to 4.5 m if necessary). The sample is mounted horizontally in a furnace which will be described in subsection 4.2.4.

4.2.2 Layout of the beamline ID10A at the ESRF

X-ray photon correlation spectroscopy experiments were performed at the beamline ID10A of the ESRF. ID10A is one of the three experimental stations at the insertion device ID10, also called Troïka beamline. The schematics are shown in Fig. 4.8.

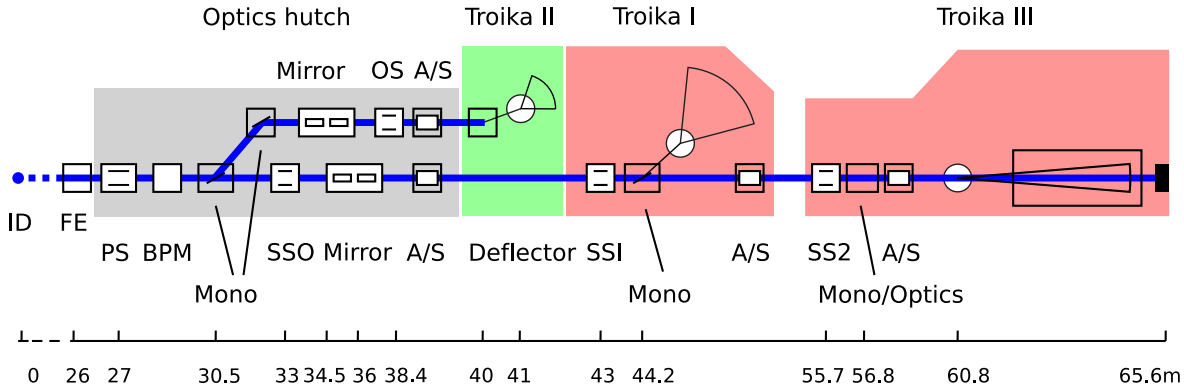

Figure 4.8: Schematic layout of the Troïka beamline (ID10). Figure taken from [8], based on [129].

The insertion device (ID) providing the radiation consists of three undulators, one with a 27 mm period (U27), one 35 mm undulator (U35), and a revolver unit which carries both U27 and U35 undulators. Therefore, a 2×U27+U35 or 2×U35+U27 setup can be provided, depending on the energy requirements. The undulators are installed in series in a high-β straight section, i.e., the source size (full width at half maximum, FWHM) is rather large (928 μm horizontal × 23 μm vertical) for the benefit of a small divergence of the electron beam (24 μrad horizontal × 9 μrad vertical). The frontend (FE), at 26 m distance from the insertion device, connects the beamline to the storage ring and contains the main beam shutter. The radiation coming from the undulators then passes through the optics hutch with the primary slits (PS) and the beam position monitor (BPM). Independent operation of the ID10B branch ("Troïka II") from the other two branches is achieved by splitting the white beam with a diamond(111) monochromator

crystal into a transmitted white beam and a monochromatic beam which is deflected into the ID10B hutch.

The transmitted white beam passes through a pair of secondary slits (SS0), a double mirror in vertical reflection geometry and an absorber/shutter module (A/S) before traversing the ID10B hutch through a shielded pipe and entering into the ID10A ("Troïka I") experimental station. There it passes through a secondary slit module (SS1), a multi-crystal monochromator (containing four single-bounce crystals), and another absorber/shutter module (A/S) at the hutch exit. Finally, a transfer pipe can guide the beam into the ID10C ("Troïka III") station, equipped with a secondary slit module (SS2) and a Si(111) channel-cut monochromator.

The multi-crystal monochromator in horizontal scattering geometry, located at 44.2 m from the source (see Fig. 4.8), contains diamond(111), diamond(220), and silicon(111) crystals and can operate at energies between 7.5 keV and 20 keV. The intrinsic energy resolution $\Delta E/E$ is between $0.2 \cdot 10^{-4}$ for diamond(220) and $1.4 \cdot 10^{-4}$ for silicon(111), leading to a photon flux I_0 at the sample of about $5 \cdot 10^{13}$ photons/s/mm^2 at 100 mA electron beam current at 8 keV. The coherent intensity for a 10×10 μm^2 beamsize is then larger than 10^9 photons/s for 100 mA. Collimation of monochromatic x-rays - provided by a Si(111) monochromator - and pinhole apertures (with a typical diameter of 10 μm at a distance $R_s = 46$ m from the source with the size d_s) yield partially coherent x-rays with a transverse coherence length of $\xi_t = \lambda R_s/(2d_s) \approx 10$ μm, and the energy bandpass of the monochromator leads to a longitudinal coherence length of $\xi_l = \lambda^2/(2\Delta\lambda) \approx 1$ μm for 8 keV radiation [129].

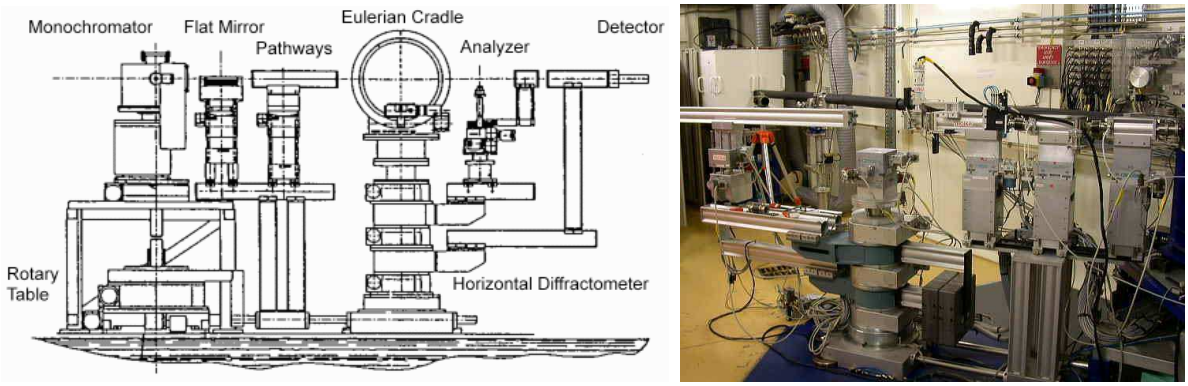

Figure 4.9: Diffractometer at the beamline ID10A [129].

The sample cell is placed into a 6-circle high-resolution diffractometer that can be used in horizontal and vertical scattering geometry as shown in Fig. 4.9. The incident

radiation is coming from the left in the sketch and from the right in the photo. For the measurements presented in this work, the Eulerian cradle was replaced by an x-y translation assembly and a double tilt stage (range of $\pm 20°$), because for the x-ray beam to hit the sample at a fixed, shallow angle the full four-circle capacity of the Eulerian cradle is not necessary. The scattering angle is defined by two horizontal turntables. A third one can carry additional detectors or support pathways for the scattered radiation. For measurements at different energies, the diffractometer is mounted on a platform that can be moved on air-cushions on a circular path by connecting it to the rotary table underneath the monochromator, flat mirror and pathways. A pinhole is placed in front of the sample cell to reduce the scattering volume to a value comparable to the coherence volume of the radiation, allowing for partially coherent illumination of the sample. The Fraunhofer fringes caused by the pinhole are suppressed by a set of guard slits behind the pinhole. Scintillation counters, avalanche photo diodes or charged coupled device (CCD) detectors can be used for data acquisition. For the measurements presented in this work, a deep-depletion direct-illumination CCD detector is used.

4.2.3 Preparation of polymer-metal composites

The metal/polymer sample was prepared by spincoating polystyrene solved in toluene onto a polished silicon wafer cleaned with ethanol and distilled water without removing the native oxide layer. To extract residual toluene, the film was annealed under vacuum conditions at about 10^{-6} mbar for 12 h at 30 K above the glass transition temperature of the bulk polymer (T_G between 353 K and 371 K, depending on the molecular weight) and then cooled down slowly to 300 K at a rate of about 20 K/h.

The gold clusters are produced in a high-vacuum chamber (see Fig. 4.10) by thermal evaporation of gold from a molybdenum crucible onto the polymer surface with a deposition rate of about 0.5 Å/min, while the polymer surface is held at room temperature. The vacuum level during deposition is about $10^{-8} - 10^{-9}$ mbar. As the thermal energy of a gold atom hitting the polymer surface is only about 10% of the energy of the polymer C-C and C-H bonds, respectively, the adsorption of the gold particles can scarcely damage the polymer [130]. As the metal-metal interaction is much stronger than the metal-polymer one, the gold atoms diffuse on the polymer surface during the evaporation until they nucleate or eventually desorb again [131]. The low evaporation rate causes a formation of relatively few clusters [132], and the condition $T < T_G$ for the polymer surface during the deposition leads to a confinement of the clusters in a narrow surface region [133]. As the surface tension of the metal is almost two orders of magnitude higher than that of the polymer, spherical, almost monodispersive clusters

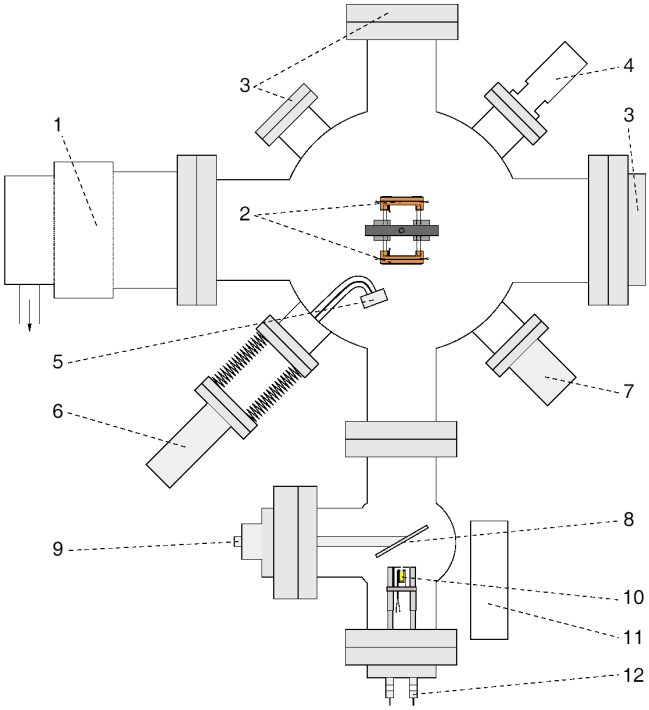

Figure 4.10: Schematic view of the evaporation chamber: (1) turbo molecular pump, (2) sample holder, (3) windows for observation, (4) current feedthrough for heating and temperature control, (5) oscillating crystal, (6) manipulator for oscillating crystal, (7) pressure gauge, (8) shutter for screening the sample holder, (9) shutter manipulator, (10) molybdenum crucible with gold supply, (11) fan, (12) current feedthrough for the evaporator; distance between evaporator and sample holder $\approx$ 31 cm. Picture taken from [106].

form for nominal gold layer thicknesses smaller than $\approx$10 Å [134]. The gold clusters stay in the near surface region of the polymer even at temperatures above the glass transition [134].

Two samples were used for the experiments. Sample A consists of an 800 Å thick polystyrene film (molecular weight M_w = 34.4 kg/mol, $T_G \approx$ 353 K) with a nominal gold layer thickness of d_n = 8 Å, which leads to a cluster coverage of about 33% of the polymer surface and an average cluster radius of $r_c \approx$ 18.5 Å. The nominal thickness describes the thickness that a layer of gold would have if the amount of gold that in reality forms clusters appeared as a smooth layer. By comparison between the nominal gold thickness measured by the oscillatory crystal in the evaporator and the electron density profile perpendicular to the surface obtained from x-ray reflectivity measurements, a model of the cluster arrangement (monodisperse and on the surface) was established, leading to an empirical formula for calculating the gold coverage f from the nominal

gold thickness [106]:

$$f = 1.52 + 4.75\, d_\mathrm{n} - 0.11\, d_\mathrm{n}^2 = \frac{3}{4}\frac{d_\mathrm{n}}{r_\mathrm{c}}. \tag{4.19}$$

Sample B has a polymer film thickness of 1000 Å (M_w = 220 kg/mol, $T_\mathrm{G} \approx 371$ K and a nominal gold layer thickness of $d_\mathrm{n} = 16$ Å, resulting in a coverage of 49% and a cluster radius of $r_\mathrm{c} \approx 24.3$ Å. The static structure of similar systems has been studied by x-ray scattering [130] and transmission electron microscopy [135] methods. The glass transition temperature for the two samples is estimated by an empirical formula based on measurements by R. Weber [106]:

$$T_\mathrm{G} \approx 349.5\,\mathrm{K} + 0.0983\,\mathrm{K\,mol/kg} \cdot \mathrm{M_w}. \tag{4.20}$$

4.2.4 Sample environment

The layout of the furnace containing the samples during the XPCS experiments was developed by M. Krämer and is described in detail in his diploma thesis [136]. A temperature range from room temperature to around 500 K has to be covered and kept stable during the measurements, and vacuum conditions (10 mbar) are required to prevent oxidation of the polymer at high temperatures. For this work, a similar furnace with small modifications was constructed as shown in Fig. 4.11.

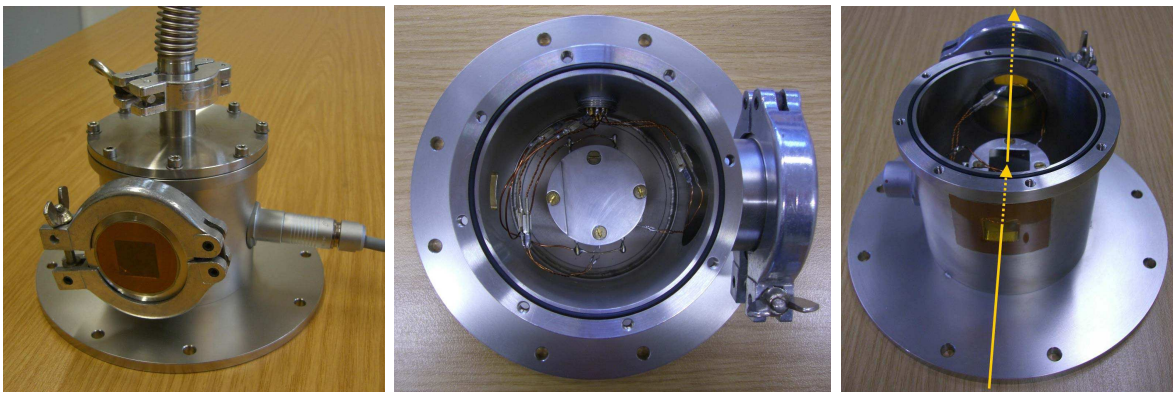

Figure 4.11: Furnace for metal-polymer samples. Left: furnace from the outside (on top: evacuation flange; on the right: connector for heating resistor and temperature sensors; in front: exit Kapton window for the beam). Middle: view of the interior of the sample cell. Right: furnace with beam path.

The sample is positioned on an aluminium block in the center of the furnace which is heated by a resistor. To prevent steaming, the electrical connections are maintained

by a varnish wire. Temperature isolation is achieved by a Macor insulator underneath the heating block, and T is controlled by two ceramic coated platinum sensors (Pt100) connected to a Lakeshore 340 controller. With optimal control parameters for this furnace ($P = 70$, $I = 28$, $D = 90$ [136]) an accuracy of $\Delta T = \pm 5$ mK can be accomplished. An exit-window size of 20×20 mm^2 and a sample diameter of 80 mm lead to a maximal exit angle of around 14° when the sample is positioned in the middle of the height of the window, which is sufficient for the experiments presented in this work. The exit window can be removed to connect the furnace to a flight tube to minimize air scattering.

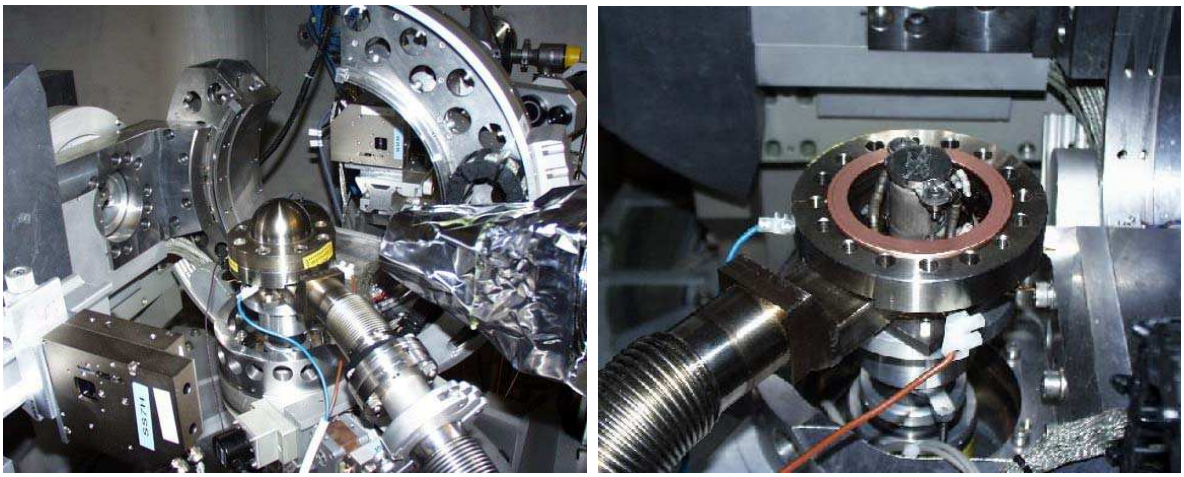

Figure 4.12: Furnace at the ID01. Left: Furnace with mounted beryllium dome on the ID01 diffractometer. Right: Inside of the furnace with removed Be dome. Pictures taken from [128].

For the incoherent GISAXS measurements at ID01 the beryllium dome furnace provided by the beamline is used as depicted in Fig. 4.12. The heating and temperature control is very similar to the furnace described before. The sample is heated by a resistance inside an evacuable Be hemisphere. This Be dome is ideally suited for small or wide angle scattering experiments in reflection geometry on flat samples. The temperature is controlled by a thermocouple in direct contact with the sample support, connected to a Eurotherm temperature controller. A temperature stability of around 0.5 K is maintained, and $T \approx 900$ K can be achieved in a vacuum of 10^{-8} mbar. For the measurements presented here, a pressure of 10^{-6} mbar is sufficient.

4.3 Experimental results and interpretation

4.3.1 Incoherent measurements of the static structure

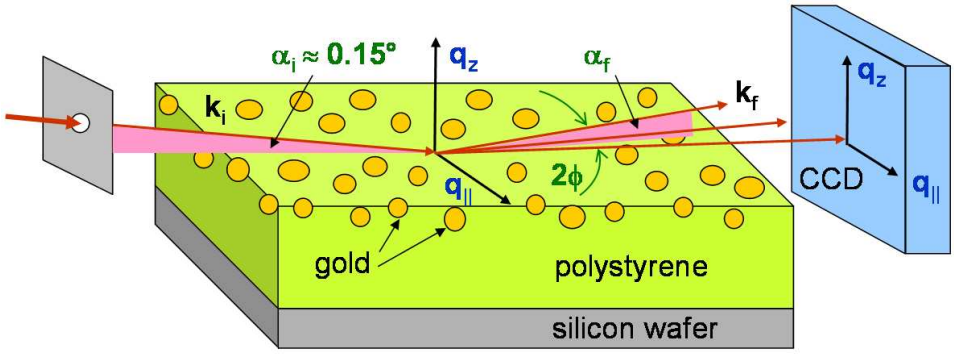

Figure 4.13: Schematic view of the scattering setup in GISAXS geometry with a sketch of the sample structure; the incident and exit wavevectors are denoted as k_i and k_f, $\alpha_i = 0.15°$ and α_f are the incident and exit scattering angles, respectively, and ϕ is the exit angle out of the plane of incidence.

The temperature evolution of the static structure of the cluster assembly has first been studied by incoherent grazing incidence small angle x-ray scattering (GISAXS) [137] at the ID01 beamline (ESRF). The scattering geometry is depicted in Fig. 4.13. In principle, it is exactly the same scheme as for coherent GISAXS presented in the following subsection. Only in the present case, the beam passes through an entrance slit, where for coherent GISAXS a pinhole is placed. The monochromatic x-ray beam (wavelength $\lambda = 0.69$ Å) then impinges on the sample surface with an incidence angle $\alpha_i = 0.15°$, allowing for an enhancement of the near surface scattered intensity with regards to scattering from the bulk. The wavelength corresponds to a rather high photon energy of 18 keV which is necessary to prevent radiation damage. The diffuse scattered intensity, recorded by a Princeton CCD with a pixel size of 60×60 μm^2, is mostly governed by the gold scattering, allowing for a precise monitoring of the cluster size and distribution. Within the distorted-wave Born approximation, the incoherently scattered intensity in the grazing incidence geometry is proportional to $\tilde{t}(\alpha_i)P(q)f(q_{||})\tilde{t}(\alpha_f)$, where $\tilde{t}(\alpha_{i/f})$ are the transmission functions for the incident and exit beams, $P(q)$ is the form factor of a single spherical particle (i.e., the squared modulus of the Fourier transform of a sphere whose size presents a Gaussian distribution) and $f(q_{||})$ is the static structure factor, accounting for the lateral ordering of the clusters on the surface ($q_{||}$ denoting the

wavevector transfer parallel to the surface). It is given by [98]

$$f(q_{\parallel}) = \frac{1 - \exp(-2q_{\parallel}^2\sigma_{\mathrm{d}}^2)}{1 - 2\exp(-q_{\parallel}^2\sigma_{\mathrm{d}}^2)\cos(q_{\parallel}d) + \exp(-2q_{\parallel}^2\sigma_{\mathrm{d}}^2)} \tag{4.21}$$

where d is the mean inter-particle distance with a dispersion σ_{d}. Two $q_{\parallel}$ scans taken at 300 and 450 K are presented on the inset of Fig. 4.14 together with their best fits. Due to the large wavevector transfers $q_{||}$, the GISAXS measurements are sensitive to the electron density contrast on very small lateral length scales $l = 2\pi/q_{||}$ of 20 Å to 300 Å.

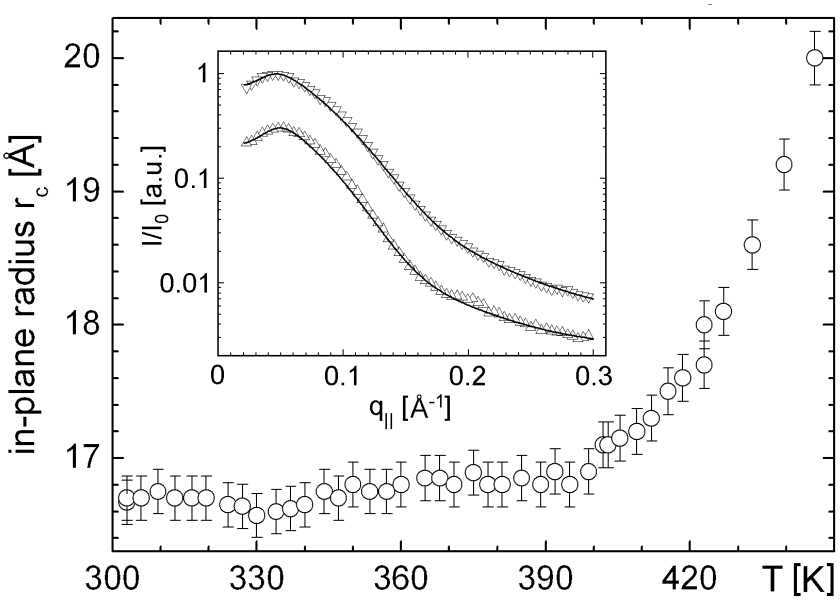

Figure 4.14: Average in-plane radius of the gold clusters as a function of temperature as extracted from the incoherent GISAXS data. The inset presents two $q_{\parallel}$ scans taken at 300 and 450 K (down and up triangles, respectively) together with their best fits.

Fig. 4.14 shows the averaged lateral radius r_{c} of the gold clusters of the sample as a function of temperature. A typical mean value of about $r_{\mathrm{c}} = (16.5 \pm 0.2)$ Å is obtained at room temperature, in agreement with previous observations [130, 135]. At $T = 400$ K, a strong increase of the mean gold cluster radius is observed. The evolution of the integrated scattered intensity shows that the total number of scatterers (i.e. the gold atoms) remains constant in the near surface region. Thus, the increase of the radius is related to the coalescence of the clusters. The driving force for this non-equilibrium dynamics is the attractive Van-der-Waals interaction between the gold clusters, which ultimately leads to their coalescence. Together with the radius, the mean particle distance of about $d = (77 \pm 2)$ Å is extracted. The variations of the static structure factor $f(q_{||}, \tau)$ with temperature are within the experimental uncertainties.

4.3.2 Two dimensional x-ray photon correlation spectroscopy measurements and data analysis

XPCS experiments have been performed in the same grazing incidence geometry as at the ID01 beamline using the coherent beam of the ID10A beamline (ESRF) with $\lambda = 1.16$ Å, corresponding to a photon energy of 10.64 keV which is still rather high in order to minimize beam damage. A schematic view of the experimental setup is shown in Fig. 4.13. A pinhole with a diameter of 20 μm is placed upstream of the sample in order to obtain a collimated and transversely coherent beam. The beam is tilted vertically by a mirror onto the sample surface with $\alpha_i = 0.15°$. The measurements are performed around the region of total external reflection of the sample where the penetration depth of the evanescent wave is a few nm, allowing for the surface sensitivity. A temperature range from 290 K - well below T_G - to 440 K is investigated, but due to the limited dynamic range of the detector, decaying correlation functions can only be observed in the temperature interval between 400 K and 440 K. The effects of possible beam damage are further reduced by acquiring each data set at a new sample surface position. The scattered intensity is recorded by a direct-illumination Princeton CCD camera with 1242 $\times$ 1152 pixels (pixel size of 22.5 $\times$ 22.5 μm^2) at a distance of 1.3 m from the sample. For each temperature, 400 images are taken with an exposure time of 10 s (plus readout time of about 2.5 s). This kind of acquisition allows to further monitor possible beam damages by controlling the average intensity of each picture. From the recorded images the intensity autocorrelation function $g_2(q_{||}, \tau)$ is calculated for each pixel. The final correlation function is obtained by averaging correlation functions with the same wave vector transfer, a so-called multiple-speckle analysis.

With XPCS experiments, the desired correlation function is not directly measured, but has to be calculated from the intensity measured at different times. In case of a point detector, a hardware-based autocorrelator yields this information automatically, but the advantage of a CCD consists in measuring simultaneously over a large q region. In this case there are several gigabyte of data which have to be stored first. H. Sternemann has developed a Matlab program for calculating the correlation functions from CCD pictures taken at the ESRF which is described in his diploma thesis [92]. An overview is presented in Fig. 4.15. From the input file containing geometrical information about the scattering geometry and the sample a CCD mask and a $q_{||}$ mask are created. The CCD mask rules out areas with damaged pixels or shadowed by the beamstop, whereas the $q_{||}$ mask contains domains with similar $q_{||}$ values. On the averaged background images (dark images taken with closed beam shutter) and the sample images the CCD mask and the $q_{||}$ mask are applied. After the averaged background is subtracted from the sample

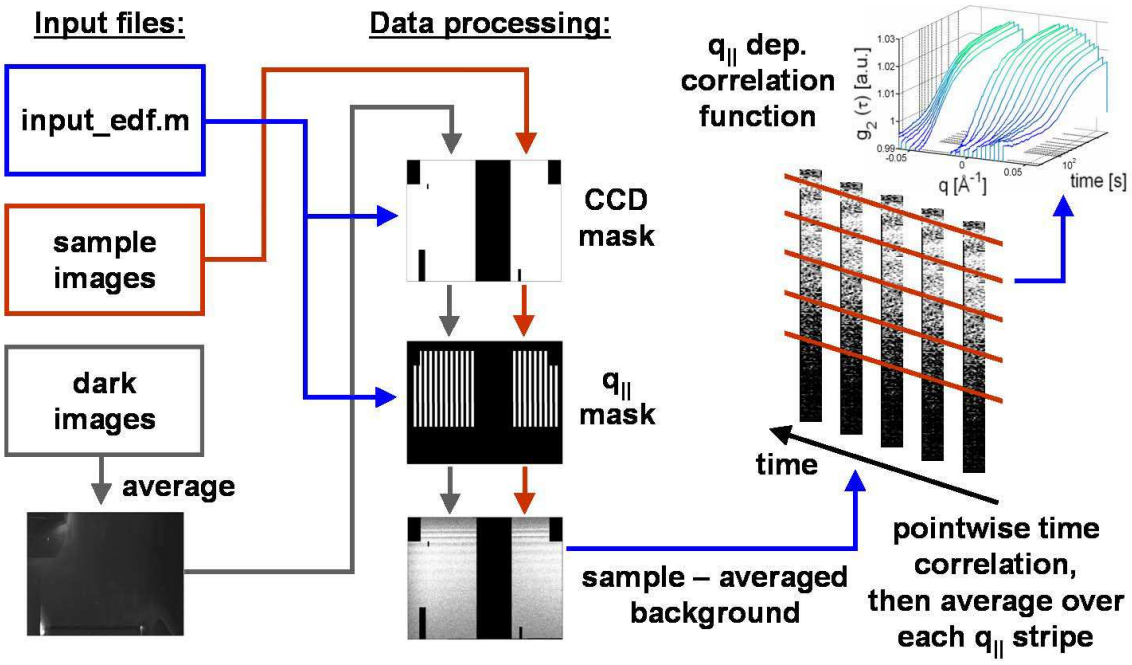

Figure 4.15: Scheme of the data processing routine for Matlab.

pictures, for each pixel the intensity-intensity correlation function is calculated over all pictures that are defined in the input file of the computation program. Afterwards the correlation functions are averaged over each $q_{||}$ stripe in order to improve the statistics. As a result $q_{||}$ dependent correlation functions are obtained. A more detailed description can be found in [92].

4.3.3 Sample A: low gold coverage

Fig. 4.16 shows two images extracted from coherent GISAXS data measured on sample A at temperatures of 290 K (left, below the glass transition temperature of the polymer) and 420 K (right, above T_G). From the q_z and $q_{||}$ values in the pictures the typical length scales being probed are determined as 90 Å to 300 Å perpendicular to the sample's surface and 100 Å to 1000 Å parallel to the surface. Because of the use of a coherent x-ray beam, a grainy pattern with intensity fluctuations much larger than the fluctuations induced by the intensity statistics is visible. It is called a speckle structure and it reflects the exact positions and shapes of the cluster assembly. Interference between the polymer film and the silicon substrate leads to the well pronounced sheets of intensity oscillating along the q_z direction. A broad maximum of the scattering factor is observed at $q_{||}$ values around 0.020 Å^{-1} - 0.025 Å^{-1}, related to the lateral (nonperfect) order of the gold particles and the mean particle size. A comparison of the image measured from the

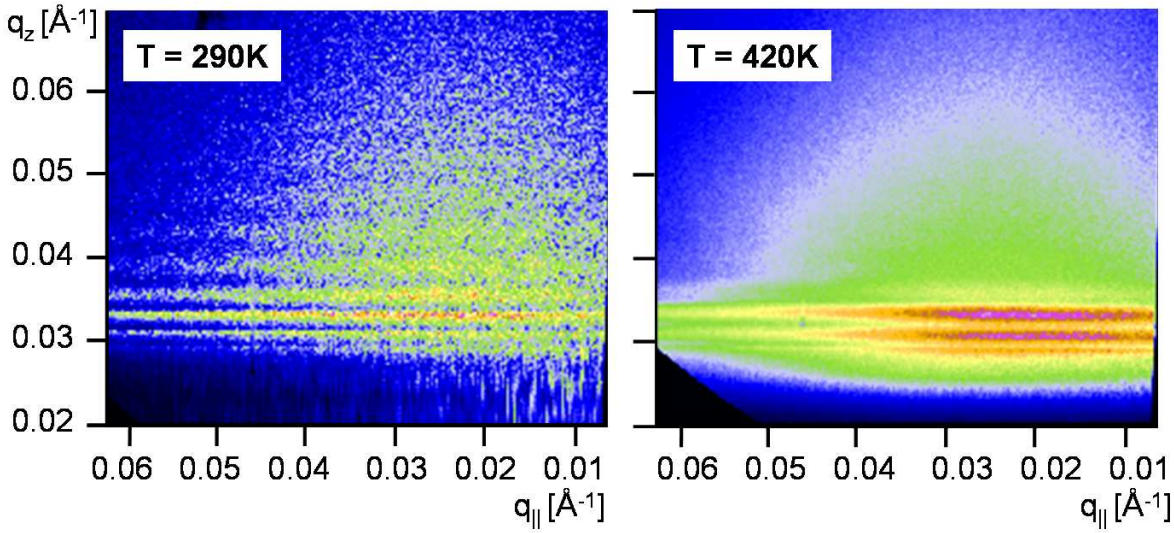

Figure 4.16: CCD images of the coherent GISAXS patterns of sample A. The left picture is taken well below and the right above T_G, each one resulting from an accumulation of 400 frames of 10 s for a single image frame.

as-prepared sample at 290 K with the high-temperature situation shows that the onset of the particle dynamics manifests itself by a blurring of the speckle pattern as the time scales of the dynamics become faster than the total acquisition time.

Details of the dynamic processes accompanied by the gold cluster coalescence can be revealed by calculating the intensity autocorrelation function from the images measured at different sample ages. For this purpose, each data set is divided into subsets of 100 images, each covering a time window of about 20 minutes. By use of the Siegert relation (see also Eq. 2.56) g_2 and the dynamic structure factor $f(q_\parallel, \tau)$ are connected via $g_2(q_\parallel, \tau) = 1 + \beta(q_\parallel)|f(q_\parallel, \tau)|^2/|f(q_\parallel, 0)|^2$, which leads to the intensity autocorrelation function of

$$g_2(q_\parallel, \tau) = 1 + \beta(q_\parallel) \exp[-2(\Gamma\tau)^\alpha], \tag{4.22}$$

with $\beta(q_\parallel)$ accounting for the q-dependent contrast in surface XPCS experiments [94]. The assumption of homodyne scattering for the use of the Siegert relation is valid because so far heterodyne scattering has been observed in surface scattering geometry only for very small in-plane wavevectors around 10^{-5} Å^{-1} within the resolution element of the setup. For coherent GISAXS measurements at large wavevector transfers heterodyne mixing is not expected and it is also not observed in small angle x-ray scattering geometry at similar wavevector transfers.

The autocorrelation functions are shown in Fig. 4.17. The decay below 1 is due to the small observed time window and the average over pixels with similar $q_{||}$ values [138]. At

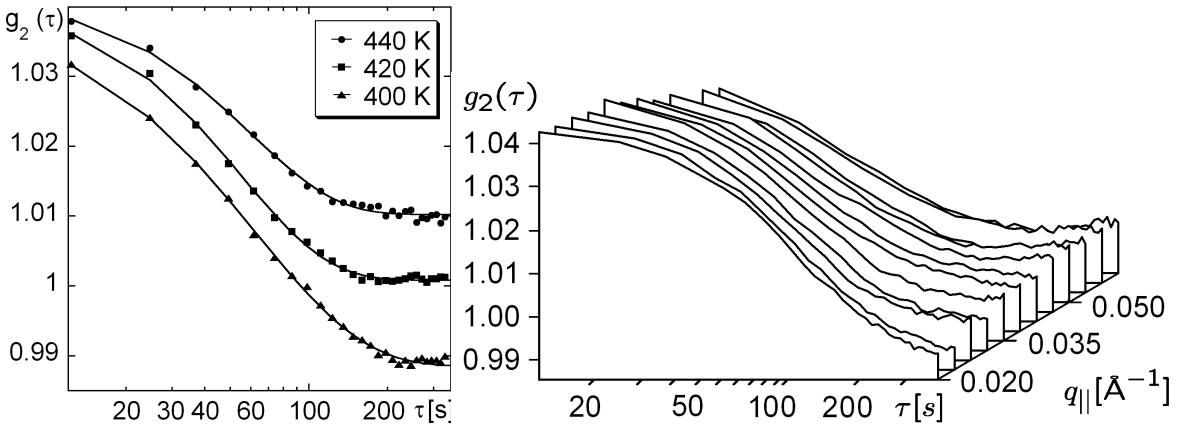

Figure 4.17: Left: correlation functions $g_2(\tau)$ measured at 440 K (circles), 420 K (squares) and 400 K (triangles), respectively, for $q_{||} = 0.051$ Å and a sample age of 2462-3693 s. The curves are shifted vertically for reasons of clarity. The solid lines represent the fits according to Eq. 4.22. Right: $g_2(\tau)$ for all measured wavevector transfers $q_{||}$ at 420 K for the same sample age.

room temperature the typical decay time is considerably larger than 20 minutes, thus showing no decay of $g_2(q_{||}, \tau)$, as the polymer matrix is still in a glassy state. Above the polymer glass transition the autocorrelation function decays faster with increasing temperature. Hence, the viscosity of the surrounding polymer matrix determines the mobility of the gold clusters.

time [s]	α (400 K)	α (420 K)	α (440 K)
0 - 1231	0.69±0.10	0.72±0.16	1.49±0.17
1231 - 2462	0.99±0.09	1.00±0.15	1.55±0.11
2462 - 3693	0.99±0.10	1.33±0.15	1.33±0.12

Table 4.1: Exponent α for sample A for different T and sample ages. As α is independent of $q_{||}$, the mean values of α over 15-20 $q_{||}$ values are given here together with the standard deviation.

The refinement of the data with Eq. 4.22 yields the following behavior of the exponent α as a function of sample age: at 400 K the exponent increases from a starting value of 0.7 ± 0.1 up to 1.0 ± 0.1, i.e., the form of the dynamic structure factor is evolving as a function of sample age from a stretched exponential at early times to a simple exponential behavior at later times. At 420 K α increases from 0.7 ± 0.2 to 1.3 ± 0.2, corresponding to a transition from stretched to compressed exponential behavior. At 440 K the exponent has a nearly constant value of 1.5 ± 0.2 (see Tab. 4.1).

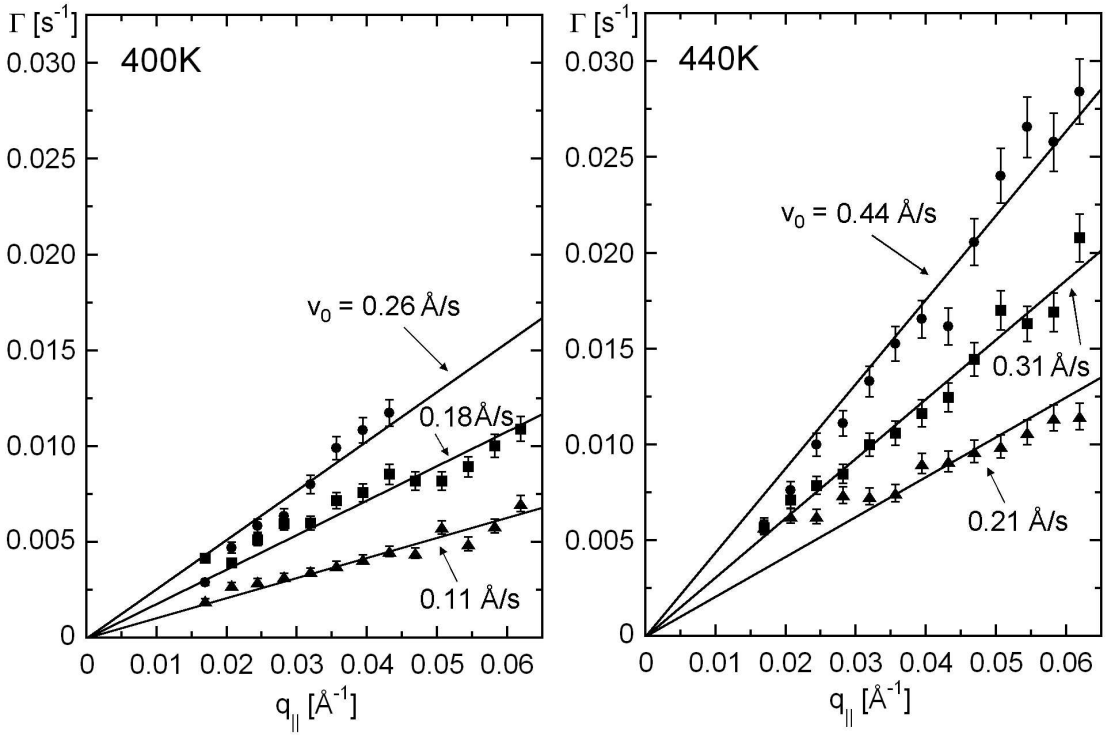

Figure 4.18: Dispersion relations (relaxation rate Γ versus $q_{||}$) at 400 K (left) and 440 K (right) presented for three different ages: 0-1231 s (circles), 1231-2462 s (squares), and 2462-3693 s (triangles). The solid lines are linear fits to the data. Each line is labeled with the mean particle velocity $v_0 = \Gamma/q_{||}$.

The relaxation rate $\Gamma(q_{||})$ is found to vary linearly with $q_{||}$, i.e., $\Gamma \sim q_{||}$ (Fig. 4.18) for all sample ages. As the linear fits represent a dispersion relation, they have to go through the origin. One might argue that there might be additional effects on length scales larger than $2\pi/(0.02\ \text{Å}^{-1}) \approx 300$ Å that might cause an offset, but within the experimental accessible q range such effects are not visible. Therefore, the simplest model consistent with the data was chosen. Accompanied with the evolution of the exponent α as a function of sample age, the value of the relaxation rates Γ also changes with age (see also Fig. 4.18). The characteristic relaxation time $t_c = \Gamma^{-1}$ is increasing with sample age; i.e., the system is slowing down with time, a behavior which has frequently been found in 3D colloidal suspensions showing hyperdiffusive dynamics. The gold cluster dynamics is clearly distinct from the simple Brownian motion for which Γ is proportional to $q_{||}^2$.

It might be noted here that overdamped capillary waves also lead to a linear dependence of Γ as a function of $q_{||}$. However, they cannot explain the existence of a stretched or compressed exponential or aging. Moreover, the data were measured at the maximum of the scattering factor of the gold clusters which is out of the scattering plane.

Therefore, the scattering intensity of capillary waves on the polymer surface is several orders of magnitude lower than the signal from the gold clusters and can be neglected. Moreover, capillary waves would be observed at much higher frequencies. As can be seen in Fig. 4.18, the relaxation rates are between around 0.005 s^{-1} and 0.030 s^{-1}. If one assumes overdamped capillary waves[1], the relaxation rate is calculated as $\Gamma = \gamma q_{||}/(2\eta)$ (see Tab. 3.1). With the surface tension $\gamma = 0.03$ N/m and the viscosity $\eta = 4 \cdot 10^5$ Pa s for 420 K (see e.g. Ref. [101]) and a typical $q_{||}$ value of 0.05 $Å^{-1}$ the relaxation rate follows as $\Gamma \approx 20$ s^{-1}, i.e., it would be three orders of magnitude larger. For all these reasons capillary wave theory cannot be used to explain the observed correlation functions.

A model for this peculiar form of the dynamic structure factor [99] has been described in section 4.1.3. Two gold clusters attracting each other through Van-der-Waals forces produce a strain field in the surrounding polymer matrix causing other particles also to move. This strain field model leads to the exponent $\alpha = \frac{3}{2}$ and the form $\Gamma \sim q_{||}$ [121] when the experimental time scale is considerably smaller than the typical coalescence time. This condition should be verified here, where the static structure factor determined from measurements at the ID01 beamline does not show any change within a 10 min time scale. While these models are usually discussed in a 3D framework, our experiment clearly shows that the same dynamic structure factor is observed in 2D motion on a free surface. This type of ballistic motion can be described by a power-law velocity distribution of the particles which is determined by the derivative of the Lévy stable law [120]. The mean particle velocity within this theory is $v_0 = \Gamma/q_{||}$, and we find typical values of v_0 ranging from around 0.26 Å/s in the beginning to 0.11 Å/s at later times for 400 K, and from around 0.44 Å/s at early times to 0.21 Å/s at the end for 440 K. This shows that (*i*) the mean particle velocity increases with temperature, and (*ii*) due to aging, the particles slow down to around 40% - 50% of their initial mean velocity. Within our observed time scale of around 10 min, the gold clusters move over distances of $v_0 t \approx 160$ Å in the first time region at 400 K, then slow down and move ≈ 60 Å, whereas at 440 K they cover larger length scales of around 270 Å in the beginning and 130 Å in the end. As the distances covered by the clusters are larger than the mean cluster-cluster distance of about 80 Å, it is likely that the coalescence does not occur between first neighbors, but that the particle has to further move through the polymer fiber network.

[1] Due to the high viscosity in the system the surface waves are damped so much that propagating modes become unstable and do not occur.

4.3.4 Sample B: high gold coverage

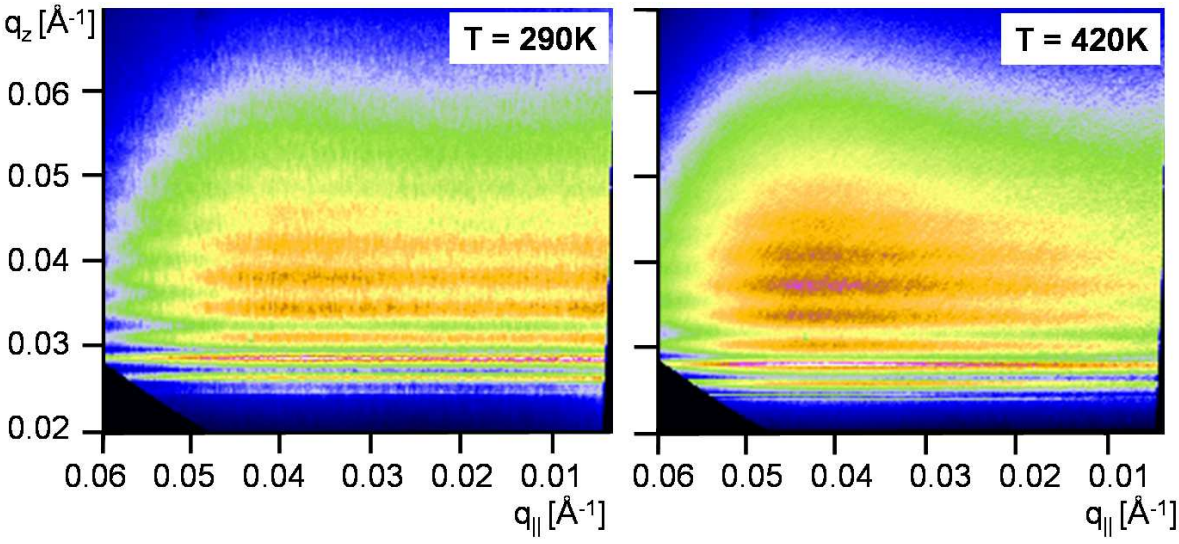

Figure 4.19: CCD images of the coherent GISAXS patterns of sample B. As for sample A, the left picture was taken well below and the right above T_G of polystyrene, each one resulting from an accumulation of 400 frames of 10 s for a single image frame.

Figure 4.19 shows two images extracted from coherent GISAXS data of sample B measured at temperatures of 290 K (left) and 420 K (right). Again the interference fringes from the polymer film and the speckle structure for the low temperature picture are visible. However, the intensity is higher than for sample A because of the larger gold coverage (d_n = 16 Å compared to d_n = 8 Å for sample A). Moreover, the broad maximum of the scattering factor is observed at $q_{||}$ values around 0.04 Å^{-1} which is about twice as large as for sample A. Therefore, the mean cluster-cluster distance is smaller here. This is due to the fact that a higher amount of gold was evaporated on sample B than on sample A, causing the formation of larger clusters. As sample B is decorated with more and larger clusters compared to sample A, the mean particle distance is likely to decrease.

For sample B the same procedure for obtaining the correlation functions as for sample A was applied. Sample B with a higher molecular weight and a higher gold coverage exhibits a different behavior than sample A. The dynamic structure factor is found to be a compressed exponential at all sample ages, with values of α ranging between 1.3 ± 0.1 and 1.9 ± 0.1 as shown in Tab. 4.2. Moreover, no systematic dependence of the exponent on the temperature could be observed. One might assume a slight increase of α with the sample age, but for 400 K this is within the error bars, and for 420 K the last time region

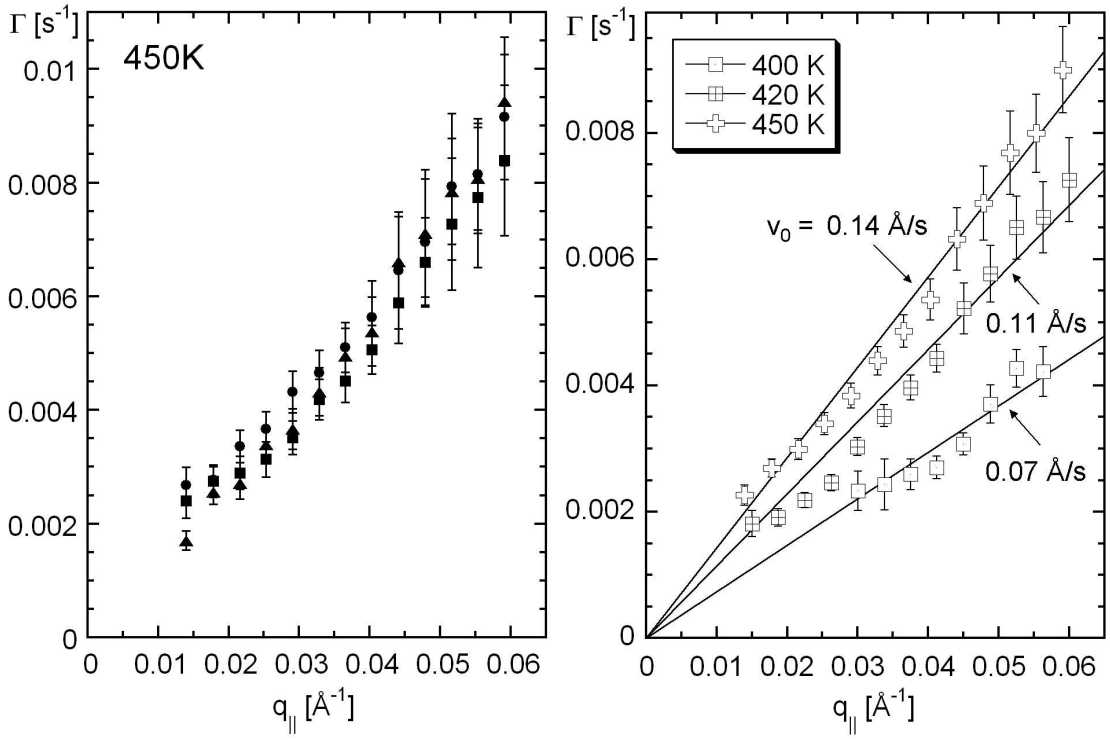

Figure 4.20: Left: Dispersion relations (relaxation rate Γ as a function of $q_{||}$) at 450 K presented for three different sample ages: 0-1253 s (circles), 1253-2506 s (squares), and 2506-3759 s (triangles). Right: Averaged dispersion relations for the complete time interval 0-3759 s for three different temperatures. The solid lines with the slopes $v_0 = \Gamma/q_{||}$ are linear fits to the data.

shows again a smaller exponent. Apart from the highest temperature at 450 K where this increase is more pronounced, the compressed exponent remains therefore nearly constant within each temperature interval.

The dispersion relations for sample B are depicted in Fig. 4.20. The left part of Fig. 4.20 shown for 450 K is representative for all temperatures for this sample. As for sample A, the relaxation rates also increase linearly with $q_{||}$. Thus, the gold cluster motion is again of hyperdiffusive or ballistic nature. But the dispersion relation does not change systematically with time, as it is the case for the other sample, therefore aging processes have to be ruled out. This might be connected with the exponent which also does not exhibit any distinct time dependence. Thus, in this case the statistics for a single dispersion relation can be improved by averaging over all frames taken at a certain temperature. Moreover, the mean particle velocity v_0 ranges only between 0.07 Å/s for 400 K and 0.14 Å/s for the highest temperature of 450 K. v_0 is therefore about a factor 2 smaller for sample B compared to the mean particle velocity for sample

time [s]	α (400 K)	α (420 K)	α (450 K)
0 - 1253	1.55±0.13	1.80±0.12	1.26±0.11
1253 - 2506	1.56±0.18	1.90±0.13	1.42±0.13
2506 - 3759	1.60±0.21	1.72±0.15	1.56±0.14

Table 4.2: Exponent α for sample B for different temperatures and ages. Again, the mean values of α over 15-20 $q_{||}$ values are presented together with the standard deviation.

A averaged over all sample ages. Although there is not any clear explanation concerning the absence of aging, it might involve the differences in the radius size of the gold clusters and the molecular weight of the polymer, which are both larger here. It is likely that the clusters have formed agglomerates which cannot move as freely as before, as expected by R. Weber [106] and indicated by the smaller mean particle velocities. Hence, it might be necessary to measure over much larger time scales to detect a systematical dependence of the exponent on the sample age as well. Moreover, as mentioned in subsection 4.1.1, starting at molecular weights of $M_w \approx 35$ kg/mol entanglement effects of the polymer chains increase strongly, therefore for sample B the cluster motion is inhibited by the polymer chains much more than for sample A. However, as the ballistic motion of the particles and the linear dispersion relation are found for this sample as well, the important features typical for out-of-equilibrium systems are in agreement with the results obtained from sample A.

4.4 Conclusions

The two-dimensional dynamics of gold clusters on thin polystyrene films were measured on nanometer length scales. The method of XPCS is uniquely suited for investigating these slow dynamics at large wavevector transfers. At temperatures above the polymer matrix glass transition the gold clusters start to move. These cluster dynamics are caused by attractive Van-der-Waals interactions between the nanoparticles which ultimately lead to coalescence. The dynamic structure factor of this dynamics, $f(q_{||}, \tau)$, has been measured. Its peculiar form, which is proportional to $\exp[-(\Gamma\tau)^\alpha]$ with exponents $\alpha \approx 1.5$, indicates a 2D hyperdiffusive or ballistic motion of the gold clusters.

For sample A with $M_w = 34.4$ kg/mol and a gold layer of $d_n = 8$ Å, aging phenomena as typical for out-of-equilibrium systems and a transition from a stretched to a compressed exponential form of the dynamic structure factor could be observed. Sample B with a higher molecular weight of $M_w = 220$ kg/mol and a gold layer twice as large as for

sample A does not exhibit any clear aging effects and the exponent is found to be of a compressed form ($\alpha > 1$) for all temperatures and times. A possible explanation for the absence of aging might be due to two effects: (*i*) the larger size of the clusters, and (*ii*) the longer polymer chains, hence the particle motion might be more hindered at the observed time scales.

One may argue that the size polydispersity of the gold clusters plays a role for the variation of the exponent α, at least for $\alpha < 1$: It is likely that size polydispersity leads to different relaxation times, i.e. that the smaller clusters exhibit a slightly faster motion than the larger ones. In this case one would expect a stretched exponent ($\alpha < 1$). This has been known for a long time in literature, e.g., in Refs. [139, 140] (compare also subsection 2.4.3). For Brownian motion in colloidal suspensions the diffusion constant D is known to be inversely proportional to the radius and $\Gamma = D \cdot q^2$. However, as the dependence of the relaxation rate Γ on the cluster radius is unknown for ballistic motion, it cannot be argued quantitatively for the data presented in this work how the influence of possible small-sized clusters is manifested. In addition, it is important to mention that capillary waves cannot explain the dynamics observed here: (*i*) a stretched or compressed exponential and (*ii*) the fact that the data were taken at the maximum of the structure factor of the gold clusters where the scattering signal from the polymer surface is very low and small motions of the polymer surface can be neglected compared to the large jumps of the clusters, are both strong arguments to reject the capillary wave scenario. Furthermore, the linear dependence of Γ as a function of $q_{||}$ rules out Brownian diffusive motion.

The results presented in this chapter are the first experiments concerning dynamics at nanometer length scales in surface geometry, allowing for the investigation of aging effects and hyperdiffusive motion.

The results of the present work are confirmed by recently published measurements performed by S. Narayanan et al. on gold-polystyrene systems, where a similar form of the dynamic structure factor is observed [102]. In order to generate x-ray standing waves to study XPCS on nanometer length scales, they introduce an additional palladium layer on top of a chromium buffer layer placed between the silicon substrate and the polystyrene. The samples described in Ref. [102] are of similar polystyrene thickness, but of different molecular weights (30, 65 and 120 kg/mol compared to 34.4 and 220 kg/mol in this work) and with a smaller nominal thickness of gold of 4 Å. On the one hand, with $0.01\ \text{Å} < q_z < 0.10\ \text{Å}^{-1}$ Narayanan et al. were able to measure at slightly higher q_z values as in the experiments performed within the scope of this work ($0.02\ \text{Å} < q_z < 0.07\ \text{Å}^{-1}$), but this does not affect the general results. On the other hand, their correlation functions

were taken at a single temperature of 453 K, whereas in this investigation a temperature range from 400 K to 450 K was covered. Finally, in this work photons of higher energies (10.64 and 18 keV) than in Ref. [102] (7.35 keV) were used in order to minimize radiation damage. For the analysis of the incoherent GISAXS measurements in subsection 4.3.1, a spherical particle form is assumed, whereas in [102] the gold particles are found to have a nearly twice as large lateral than vertical size which is attributed to possible clustering during the deposition process. However, as no information concerning the evaporation process is given, these results are difficult to compare with this work.

The most important difference between the study of [102] and the experiments presented in this work consists in the behavior of the dispersion relation and the exponent α of the dynamic structure factor. Here, for both samples a linear dependence of the relaxation rate on the lateral wavevector transfer could be observed, whereas in Ref. [102] this is only the case for the two highest molecular weights, and the sample with $M_\mathrm{w} = 30$ kg/mol exhibits a steeper dependence according to $\Gamma \propto q_{||}^{1.6}$. This is explained with the low molecular weight resulting in less entanglement. Therefore, the gold clusters should encounter less resistance from the polymer chains. As this effect could not be observed for sample A (34.4 kg/mol), the boundary at which entanglement effects begin to play a role defined by the critical molecular weight $M_\mathrm{c} \approx 35$ kg/mol introduced in subsection 4.1.1 seems to be rather sharp, and sample A seems to be already fully entangled.

Moreover, no aging could be observed in Ref. [102], even over measured times of several hours. This is attributed to the two-dimensional distribution of the gold clusters which diminishes the number of local stress points compared to a 3D distribution. These stress points are supposed to originate in the reduced available volume for the polymer chains due to the presence of the gold clusters. This would indicate that for the measurements in this work the gold clusters in sample A (for which aging effects could be observed) might be subject to a broader depth distribution, leading to more contact points between clusters and polymer chains than in sample B. From intuitive considerations it also seems to be obvious that sample B with the longest polymer chains and the largest gold clusters should exhibit a narrower depth distribution of the gold particles, as they are more strongly hindered to sink deeper into the polymer. However, it is difficult to understand why such a narrow distribution of the particles should also occur in the samples described in Ref. [102] where the molecular weight and the cluster size are much smaller. Another possible explanation for the fact that no aging was observed in [102] might be that the measurements were performed after the aging had already occurred, which might be plausible as only one temperature was investigated.

Furthermore, the exponent α is found to be of a compressed form between 1.4 and 1.7 for the 120 kg/mol sample, and of a stretched form between 0.5 and 0.9 for the lower molecular weight samples in Ref. [102]. Hence, the compressed exponent together with the linear dispersion relation for the 120 kg/mol sample as typical for out-of-equilibrium systems is in good agreement with the results presented in this work. For sample A at early sample ages and low temperatures of 400 K and 420 K, a compressed exponent is also found, whereas at 420 K a transition from a stretched to a compressed form occurs, and at 440 K only a compressed exponent remains. Thus, it might be interesting to see whether at higher temperatures the low-M_w samples of Ref. [102] also exhibit a compressed exponential form. Finally, good agreement is achieved concerning the mean particle velocity v_0: For the 120 kg/mol sample $v_0 = 0.15$ Å/s which is in good accordance with the velocity of 0.14 Å/s found for the same temperature for sample B (which as well does not exhibit any aging effects).

To summarize, the work of Narayanan et al. is complementary to the work presented in this chapter, as different molecular weights and a smaller gold coverage are investigated with a slightly different technique. However, the questions of the occurrence of aging and the transition from a stretched to compressed exponent in the dynamic structure factor remain open and would justify to further investigate the Au/PS system, with different temperatures and cluster sizes. Nevertheless, the general phenomenon of stress relaxation in out-of-equilibrium systems yields a good explanation for the results obtained in both studies.

5 Conclusions and future research

5.1 Summary

In the first part of this work, cooling rate dependent x-ray reflectivity measurements were performed on poly(propylene glycol) (PPG) with a molecular weight of $M_w = 400$ g/mol in order to determine how the propagation of capillary waves is influenced by the glass transition and the cooling rate. For the first time, a strong dependence of the glass transition temperature on the cooling rate could be observed at the surface. T_G changes in a broad range, reaching up to 240 K for the fastest cooling rate compared to 196.4 K in the bulk. In the bulk, typical changes of T_G are on the order of 3-5 K per decade of the cooling rate. It is interesting to note that the surface roughness σ below T_G still depends on T, i.e. the fluctuations do not freeze in completely, even for very high cooling rates. This is in good agreement with the predictions from the viscoelastic theory used by Jäckle and Kawasaki. Although the cooling rate dependence of the glass transition has been known in the bulk for a long time, it should be stressed that it has never before been seen at the surface.

Furthermore, the length scale parameter l_0 which is inversely proportional to the high-frequency shear modulus $G(\infty)$ is found to be on the order of several thousand Å, whereas viscoelastic theory with a Maxwell-Debye model for the frequency dependent viscosity $\eta(\omega)$ predicts values between 1 Å and 10 Å. This discrepancy is also confirmed by x-ray photon correlation spectroscopy (XPCS) measurements on PPG-4000. Apart from this high value, the theory introduced by Jäckle and Kawasaki is very well suited to describe the static and dynamic measurements of PPG around the glass transition, where the classical capillary wave model is not valid anymore.

It should be noted that typical dynamical features like α- and β-relaxation, the de-Gennes narrowing typical for collective dynamics in the volume and the existence of a nonergodic level are well-known properties in the bulk of glassy systems. However, these characteristics have presently not been observed at surfaces. At surfaces new hydrodynamic modes occur which are distinct from density fluctuations in the volume, and the slow dynamics observed by XPCS do not seem to be connected with collective

diffusion in the bulk.

To conclude the second part of this thesis, surface dynamics of gold clusters on thin polymer films around the glass transition were observed at nanometer length scales. At temperatures above the glass transition temperature of the surrounding polymer matrix the gold clusters start to move. This dynamics is caused by the attractive Van-der-Waals interaction between the clusters which ultimately leads to coalescence. The dynamic structure factor of this dynamics has been measured, its peculiar form $f(q_{||}, \tau) \propto \exp[-(\Gamma\tau)^{\alpha}]$ with a compressed exponent $\alpha > 1$ is reflecting a 2D hyperdiffusive or ballistic motion of the gold clusters. This is typical for systems out of equilibrium, where the dynamics is due to stress relaxation. Two gold clusters attracting each other through Van-der-Waals forces create a strain field in the surrounding polymer which causes the movement of other particles. This leads to an exponent $\alpha \approx 1.5$ and a dispersion $\Gamma \propto q_{||}$ as observed here.

For sample A with $M\mathrm{w} = 34.4$ kg/mol and a gold layer thickness of $d_{\mathrm{n}} = 8$ Å, aging phenomena which are typical for systems out of equilibrium could be observed, and a transition from a stretched to a compressed exponential form of the dynamic structure factor is found. For sample B with $M\mathrm{w} = 220$ kg/mol and $d_{\mathrm{n}} = 16$ Å no aging was found, and the exponent is of a compressed form ($\alpha > 1$). This absence of aging might be explained by the larger gold clusters forming agglomerates and being more entangled in longer polymer chains which hinders the particle motion at the observed time scales.

5.2 Outlook

X-ray reflectivity and XPCS measurements on PPG with molecular weights of $M_{\mathrm{w}} = 400$ g/mol and 4000 g/mol both result in a value of $G(\infty)$ that is several orders of magnitude smaller than the bulk value. It still has to be theoretically investigated if perhaps the simple Maxwell-Debye model used by Jäckle and Kawasaki for the viscosity has to be modified. Moreover, other XPCS experiments performed by A. Madsen et al. on PPG-2000 yield a more shallow course of the dispersion relation, i.e., a linear dependence of the relaxation rate on the wavevector transfer is already at smaller q values than for PPG-4000 not valid anymore. The form of the dispersion relation and its theoretical description are still not understood. From the experimental side it would be interesting to investigate a greater variety of molecular weights to examine whether a systematic dependence of the form of the dispersion relation on M_{w} exists.

The XPCS experiments on gold-polystyrene systems presented in chapter 4 are a pioneering work concerning the small length scales in combination with the surface

sensitivity. In future it is planned to improve this kind of experiments, which relies a lot on the development of new 2D CCD detectors and synchrotron sources, in order to cover a larger dynamical range for the data acquisition.

Furthermore, a recent study by S. Narayanan et al. is complementary to the results presented in this work, as different molecular weights and a smaller gold coverage are probed with a slightly different technique. However, it still has to be addressed under what conditions (such as sample composition and temperature or time ranges) aging effects and a transition from a stretched to a compressed exponent in the dynamic structure factor are produced. Thus, a further investigation of the Au/PS system would be of interest, concerning different temperatures and gold cluster sizes. Nevertheless, the results obtained from the analysis of the nanoparticle motion in a polymer matrix are well explained by stress relaxation which is a typical phenomenon in a wide variety of out-of-equilibrium systems.

Bibliography

[1] P. G. Debenedetti and F. H. Stillinger, *Supercooled liquids and the glass transition*, Nature **410**, 259 (2001).

[2] C. A. Angell, *Formation of glasses from liquids and biopolymers*, Science **267**, 1924 (1995).

[3] P. Jenniskens and D. F. Blake, *Structural transitions in amorphous water ice and astrophysical implications*, Science **265**, 753 (1994).

[4] J. Jordan, K. I. Jacob, R. Tannenbaum, M. A. Sharaf, and I. Jasiuk, *Experimental trends in polymer nanocomposites − a review*, Mater. Sci. Eng. A **393**, 1 (2005).

[5] R. A. Narayanan, P. Thiyagarajan, S. Lewis, A. Bansal, L. S. Schadler, and L. B. Lurio, *Dynamics and internal stress at the nanoscale related to unique thermomechanical behavior in polymer nanocomposites*, Phys. Rev. Lett. **97**, 075505 (2006).

[6] A. Bansal, H. Yang, C. Li, K. Cho, B. C. Benicewicz, S. K. Kumar, and L. S. Schadler, *Quantitative equivalence between polymer nanocomposites and thin polymer films*, Nature Mat. **4**, 693 (2005).

[7] T. Ghaderi, *X-ray intensity correlation spectroscopy from fluid surfaces*, Ph.D. thesis, University Dortmund (2006).

[8] R. Fendt, *Coherent x-ray scattering from soft-matter surfaces*, Ph.D. thesis, University Dortmund (2006).

[9] M. Tolan, *X-ray scattering from soft-matter thin films*, Springer, Berlin (1999).

[10] J. Als-Nielsen, *Elements of modern x-ray physics*, Wiley, New York (2001).

[11] Berkeley Lab, *X-ray interactions with matter*, `http://www-cxro.lbl.gov/optical_constants/getdb2.html`

[12] T. Seydel, A. Madsen, M. Tolan, G. Grübel, and W. Press, *Capillary waves in slow motion*, Phys. Rev. B **63**, 073409 (2001).

[13] M. Born and E. Wolf, *Priciples of optics*, Cambridge University Press, New York, seventh edition (2006).

[14] Y. Yoneda, *Anomalous surface reflection of x-rays*, Phys. Rev. **131**, 2010 (1963).

[15] F. Abelès, *Recherches sur la propagation des ondes électromagnétiques sinsoïdales dans les milieux stratifiés. Application aux couches minces.*, Ann. Physique (Paris) **5**, 596 (1950).

[16] L. G. Parratt, *Surface studies of solids by total reflection of x-rays*, Phys. Rev. **95**, 359 (1954).

[17] O. H. Seeck, *Reference guide for LSFIT*.

[18] H. Kiessig, *Interferenz von Röntgenstrahlen an dünnen Schichten*, Annalen der Physik **10**, 769 (1931).

[19] A. Braslau, P. S. Pershan, G. Swislow, B. M. Ocko, and J. Als-Nielsen, *Capillary waves on the surface of simple liquids measured by x-ray reflectivity*, Phys. Rev. A **38**, 2457 (1988).

[20] M. Paulus, *Röntgenstreuung an Flüssigkeits-Gas Grenzflächen*, Ph.D. thesis, University Dortmund (2006).

[21] S. K. Sinha, E. B. Sirota, S. Garoff, and H. B. Stanley, *X-ray and neutron scattering from rough surfaces*, Phys. Rev. B **38**, 2297 (1988).

[22] R. K. Heilmann, M. Fukuto, and P. S. Pershan, *Quenching of capillary waves in composite wetting films from a binary vapor: An x-ray reflectivity study*, Phys. Rev. B **63**, 205405 (2001).

[23] I. N. Bronstein, K. A. Semendjajew, G. Musiol, and H. Mühlig, *Taschenbuch der Mathematik*, fouth printing, Harri Deutsch, Frankfurt am Main (1999).

[24] S. Mora, J. Daillant, K. Mecke, D. Luzet, A. Braslau, M. Alba, and B. Struth, *X-ray synchrotron study of liquid-vapor interfaces at short length scales: Effect of long-range forces and bending energies*, Phys. Rev. Lett. **90**, 216101 (2003).

[25] G. H. Vineyard, *Grazing-incidence diffraction and the distorted-wave approximation for the study of surfaces*, Phys. Rev. B **26**, 4146 (1982).

[26] I. K. Robinson, J. A. Pitney, J. L. Libbert, and I. A. Vartanyants, *Surface morphology by reflectivity of coherent x-rays*, Physica B **248**, 387 (1998).

[27] B. Lengeler, *Coherence in x-ray physics*, Naturwissenschaften **6**, 88 (2001).

[28] S. K. Sinha, M. Tolan, A. Gibaud, *Effects of partial coherence on the scattering of x-rays by matter*, Phys. Rev. B **57**, 2740 (1998).

[29] G. J. Williams, H. M. Quiney, A. G. Peele, and K. A. Nugent, *Coherent diffractive imaging and partial coherence*, Phys. Rev. B **75**, 104102 (2007).

[30] L. Mandel and E. Wolf, *Optical coherence and quantum optics*, Cambridge University Press, New York (1995).

[31] K. A. Nugent, *Partially coherent diffraction patterns and coherence measurement*, J. Opt. Soc. Am. **8**, 1574 (1991); K. A. Nugent and J. E. Trebes, *Coherence measurement technique for short-wavelength light sources*, Rev. Sci. Instr. **63**, 2146 (1992).

[32] Z. H. Cai, B. Lai, W. B. Yun, I. McNulty, K. G. Huang, and T. P. Russell, *Observation of x-ray speckle by coherent scattering at grazing incidence*, Phys. Rev. Lett. **73**, 82 (1994).

[33] B. Chu, *Laser light scattering: Basic principles and practice*, Academic Press, Inc., Boston, second edition (1991).

[34] G. Grübel, *Korrelationsspektroskopie mit kohärenter Röntgenstrahlung*, Phys. Bl. **54**, 1036 (1998).

[35] K. F. Ludwig, Jr., *Comment on "Speckle in the diffraction patterns of Hendricks-Teller and icosahedral glass models"*, Phys. Rev. Lett. **61**, 1526 (1988).

[36] M. Sutton, S. G. J. Mochrie, T. Greytak, S. E. Nagier, L. E. Berman, G. A. Held, and G. B. Stephenson, *Observation of speckle by diffraction with coherent x-rays*, Nature **352**, 608 (1991).

[37] L. Mandel, *Correlation properties of light scattered from fluids*, Phys. Rev. **181**, 75 (1969).

[38] A. Duri, *Dynamique spatialement et temporellement hétérogène dans la relaxion lente de la matière molle vitreuse*, Ph.D. thesis, Université de Montpellier II (2006).

[39] J. Jäckle and K. Kawasaki, *Intrinsic roughness of glass surfaces*, J. Phys.: Cond. Mat. **7**, 4351 (1995).

[40] V. G. Levich, *Physicochemical Hydrodynamics*, Prentice-Hall, Englewood Cliffs, NJ, 1962.

[41] B. J. Berne and R. Pecora, *Dynamic light scattering*, Wiley, New York (1976).

[42] J. C. Earnshaw, *Surface light scattering: a methodological review*, Appl. Opt. **36**, 7583 (1997).

[43] C. Gutt, T. Ghaderi, V. Chamard, A. Madsen, T. Seydel, M. Tolan, M. Sprung, G. Grübel, and S. K. Sinha, *Observation of heterodyne mixing in surface x-ray photon correlation spectroscopy experiments*, Phys. Rev. Lett. **91**, 076104 (2003); Erratum, Phys. Rev. Lett. **91**, 179902 (2003).

[44] N. Laberge, V. Vasilescu, C. Montrose, and P. Macedo, *Equilibrium compressibilities and density fluctuations in K_2OSiO_2 glasses*, J. Am. Ceram. Soc. **56**, 506 (1973).

[45] J. L. Keddie, R. A. L. Jones, and R. A. Cory, *Size-dependent depression of the glass transition temperature in polymer films*, Europhys. Lett. **27**, 59 (1994).

[46] W. E. Wallace, J. H. van Zanten, and W. L. Wu, *Influence of an impenetrable interface on a polymer glass-transition temperature*, Phys. Rev. E **52**, R3329 (1995); J. H. van Zanten, W. E. Wallace, and W. L. Wu, *Effect of strongly favorable substrate interactions on the thermal properties of ultrathin polymer films*, Phys. Rev. E **53**, R2053 (1996).

[47] J. A. Forrest, K. Dalnoki-Veress, J. R. Stevens, and J. R. Dutcher, *Effect of free surfaces on the glass transition temperature of thin polymer films*, Phys. Rev. Lett. **77**, 2002 (1996); **77**, 4108 (1996).

[48] J. A. Forrest, K. Dalnoki-Veress, and J. R. Dutcher, *Interface and chain confinement effects on the glass transition temperature of thin polymer films*, Phys. Rev. E **56**, 5705 (1997).

[49] J. S. Sharp and J. A. Forrest, *Free surfaces cause reductions in the glass transition temperature of thin polystyrene films*, Phys. Rev. Lett. **91**, 235701 (2003).

[50] J. A. Forrest, J. Mattsson, *Reductions of the glass transition temperature in thin polymer films: Probing the length scale of cooperative dynamics*, Phys. Rev. E **61**, R53 (2000).

[51] S. Herminghaus, R. Seemann, and K. Landfester, *Polymer surface melting mediated by capillary waves*, Phys. Rev. Lett. **93**, 017801 (2004).

[52] F. L. Pratt, T. Lancaster, M. L. Brooks, S. J. Blundell, T. Prokscha, E. Morenzoni, A. Suter, H. Luetkens, R. Khasanov, R. Scheuermann, U. Zimmermann, K. Shinotsuka, and H. E. Assender, *Surface dynamics of a thin polystyrene film probed by low-energy muons*, Phys. Rev. B **72**, 121401(R) (2005).

[53] R. Loudon, *Theory of thermally induced surface fluctuations on simple liquids*, Proc. R. Soc. Lond. A **372**, 275 (1980).

[54] M. K. Sanyal, S. K. Sinha, K. G. Huang, and B. M. Ocko, *X-ray-scattering study of capillary-wave fluctuations at a liquid surface*, Phys. Rev. Lett. **66**, 628 (1991).

[55] A. K. Doerr, M. Tolan, W. Prange, J.-P. Schlomka, T. Seydel, W. Press, D. Smilgies, and B. Struth, *Observation of capillary waves on liquid thin films from mesoscopic to atomic length scales*, Phys. Rev. Lett. **83**, 3470 (1999).

[56] C. Fradin, A. Braslau, D. Luzet, D. Smilgies, M. Alba, N. Boudet, K. Mecke, and J. Daillant, *Reduction in the surface energy of liquid interfaces at short length scales*, Nature **403**, 871 (2000).

[57] A. Madsen, T. Seydel, M. Sprung, C. Gutt, M. Tolan, and G. Grübel, *Capillary waves at the transition from propagating to overdamped behavior*, Phys. Rev. Lett. **92**, 096104 (2004).

[58] S. Mora and J. Daillant, *Height and density correlations at liquid surfaces; Application to x-ray scattering*, Eur. Phys. J. B **27**, 417 (2002).

[59] J. Jäckle, *The spectrum of surface waves on viscoelastic liquids of arbitrary depth*, J. Phys.: Cond. Mat. **10**, 7121 (1998).

[60] T. Seydel, M. Tolan, B. M. Ocko, O. H. Seeck, R. Weber, E. DiMasi, and W. Press, *Freezing of capillary waves at the glass transition*, Phys. Rev. B **65**, 184207 (2002).

[61] M. Sprung, T. Seydel, C. Gutt, R. Weber, E. DiMasi, A. Madsen, and M. Tolan, *Surface roughness of supercooled polymer melts*, Phys. Rev. E **70**, 051809 (2004).

[62] D. Turnbull, *Under what conditions can a glass be formed?* Contemp. Phys. **10**, 473 (1969).

[63] C. A. Angell, *Relaxation in liquids, polymers and plastic crystals – strong/fragile patterns and problems*, J. Non-Cryst. Sol. **131-133**, 13 (1991).

[64] C. T. Moynihan, P. B. Macedo, C. J. Montrose, P. K. Gupta, M. A. DeBolt, J. F. Dill, B. E. Dom, P. W. Drake, A. J. Easteal, P. B. Elterman, R. P. Moeller, H. Sasabe, and J. A. Wilder, *Structural relaxation in vitreous materials*, Ann. N.Y. Acad. Sci. **279**, 15 (1976).

[65] R. Böhmer, K. L. Ngai, C. A. Angell, and D. J. Plazek, *Nonexponential relaxations in strong and fragile glass formers*, J. Chem. Phys. **99**, 4201 (1993).

[66] U. Buchenau, *Physik der Polymere*, in: *Physik der Polymere*, Vorlesungsmanuskripte des 22. IFF-Ferienkurses vom 25.2. bis 8.3.1991 im Forschungszentrum Jülich (1991).

[67] D. L. Sidebottom, B. V. Rodenburg, and J. R. Changstrom, *Connecting structure and dynamics in glass forming materials by photon correlation spectroscopy*, Phys. Rev. B **75**, 132201 (2007).

[68] R. D. Priestley, C. J. Ellison, L. J. Broadbelt, and J. M. Torkelson, *Structural relaxation of polymer glasses at surfaces, interfaces, and in between*, Science **309**, 456 (2005).

[69] B. Frick and D. Richter, *The microscopic basis of the glass transition in polymers from neutron scattering studies*, Science **267**, 1939 (1995); D. Richter, B. Frick, and B. Farago, *Neutron-spin-echo investigation on the dynamics of polybutadiene near the glass transition*, Phys. Rev. Lett. **61**, 2465 (1988).

[70] P. G. de Gennes, *Liquid dynamics and inelastic scattering of neutrons*, Physica **25**, 825 (1959).

[71] R. Kohlrausch, *Theorie des elektrischen Rückstandes in der Leidener Flasche*, Ann. Phys. Chem. **91**, 179 (1854); G. Williams and D. C. Watts, *Non-symmetrical dielectric relaxation behavior arising from a simple empirical decay function*, Trans. Faraday Soc. **66**, 80 (1970).

[72] E. R. Weeks and D. A. Weitz, *Properties of cage rearrangements observed near the colloidal glass transition*, Phys. Rev. Lett. **89**, 095704 (2002).

[73] M. D. Ediger, C. A. Angell, and S. R. Nagel, *Supercooled liquids and glasses*, J. Phys. Chem. **100**, 13200 (1996).

[74] G. S. Grest and M. H. Cohen, *Liquid-glass transition: Dependence of the glass transition on heating and cooling rates*, Phys. Rev. B **21**, 4113 (1980).

[75] C. T. Moynihan, A. J. Easteal, J. Wilder, and J. Tucker, *Dependence of the glass transition temperature on heating and cooling rate*, J. Phys. Chem. **78**, 2673 (1974).

[76] R. Brüning and K. Samwer, *Glass transition on long time scales*, Phys. Rev. B **46**, 11318 (1992).

[77] R. Brüning and M. Sutton, *Volume of B_2O_3 at the glass transition*, Phys. Rev. B **49**, 3124 (1994).

[78] K. Vollmayr, W. Kob, and K. Binder, *How do the properties of a glass depend on the cooling rate? A computer simulation study of a Lennard-Jones system*, J. Chem. Phys. **105**, 4714 (1996); *Cooling-rate effects in amorphous silica: A computer-simulation study*, Phys. Rev. B **54**, 15808 (1996).

[79] J. Buchholz, W. Paul, F. Varnik, and K. Binder, *Cooling rate dependence of the glass transition temperature of polymer melts: Molecular dynamics study*, J. Chem. Phys. **117**, 7364 (2002).

[80] F. P. Buff, R. A. Lovett, and F. H. Stillinger, Jr., *Interfacial density profile for fluids in the critical region*, Phys. Rev. Lett. **15**, 621 (1965).

[81] C. Gerthsen and H. Vogel, *Physik*, Springer, Berlin, Heidelberg (1995).

[82] T. Seydel, *Glasoberflächen: Einfrieren von Kapillarwellen?*, Ph.D. thesis, University Kiel (2000).

[83] R. Zwanzig, *Time-correlation functions and transport coefficients in statistical mechanics*, Ann. Rev. Phys. Chem. **16**, 67 (1965).

[84] L. Landau, E. Lifshitz, *Statistical physics*, Pergamon, Oxford (1969).

[85] R. Fendt, *Strukturuntersuchungen an dünnen Flüssigkeitsfilmen*, Diploma thesis, University Dortmund (2003).

[86] U. Pietsch, V. Holý, and T. Baumbach, *High-resolution x-ray scattering*, Springer, New York (2004).

[87] J. Cochrane, G. Harrison, J. Lamb, and D. W. Phillips, *Creep, creep recovery and dynamic mechanical measurements of a poly(propylene glycol) oligomer*, Polymer **21**, 837 (1980).

[88] G. T. Dee and B. B. Sauer, *The molecular weight and temperature dependence of polymer surface tension: Comparison of experiment with interface gradient theory*, J. of Coll. and Interf. Sc. **152**, 85 (1992).

[89] J. Schüller, Yu. B. Mel'nichenko, R. Richert, and E. W. Fischer, *Dielectric studies of the glass transition in porous media*, Phys. Rev. Lett. **73**, 2224 (1994).

[90] T. Seydel, A. Madsen, M. Sprung, M. Tolan, G. Grübel, and W. Press, *Setup for in situ surface investigations of the liquid/glass transition with (coherent) x-rays*, Rev. Sci. Instrum. **74**, 4033 (2003).

[91] A. Braslau, M. Deutsch, P. S. Pershan, A. H. Weiss, J. Als-Nielsen, and J. Bohr, *Surface roughness of water measured by x-ray reflectivity* , Phys. Rev. Lett. **54**, 114 (1985).

[92] H. Sternemann, *Fluktuationen von Polymeroberflächen, 2D-XPCS in Oberflächengeometrie*, Diploma thesis, University Dortmund (2005).

[93] M.-A. Bouchiat and J. Meunier, *Spectrum of thermal fluctuations of the free surface of a simple liquid*, J. Phys. (France) **32**, 561 (1971).

[94] A. Madsen, T. Seydel, M. Tolan, and G. Grübel, *Grazing-incidence scattering of coherent x-rays from a liquid surface*, J. Synchr. Rad. **12**, 786 (2005).

[95] R. Bandyopadhyay, D. Liang, H. Yardimci, D. A. Sessoms, M. A. Borthwick, S. G. J. Mochrie, J. L. Harden, and R. L. Leheny, *Evolution of particle-scale dynamics in an aging clay suspension*, Phys. Rev. Lett. **93**, 228302 (2004).

[96] W. A. Lopes and H. M. Jaeger, *Hierarchical self-assembly of metal nanostructures on diblock copolymer scaffolds*, Nature **414**, 735 (2001).

[97] M. S. Kunz, K. R. Shull, and A.J. Kellock, *Morphologies of discontinuous gold films on amorphous polymer substrates*, J. Appl. Phys. **72**, 4458 (1992).

[98] S. Narayanan, D. R. Lee, R. S. Guico, S. K. Sinha, and J. Wang, *Real-time evolution of the distribution of nanoparticles in an ultrathin-polymer-film-based waveguide*, Phys. Rev. Lett. **94**, 145504 (2005).

[99] L. Cipelletti, S. Manley, R. C. Ball, and D. A. Weitz, *Universal aging features in the restructuring of fractal colloidal gels*, Phys. Rev. Lett. **84**, 2275 (2000).

[100] L. Cipelletti, L. Ramos, S. Manley, E. Pitard, D. A. Weitz, E. E. Pashkovski, and M. Johansson, *Universal non-diffusive slow dynamics in aging soft matter*, Faraday Discuss. **123**, 237 (2003).

[101] H. Kim, A. Rühm, L. B. Lurio, J. K. Basu, J. Lal, D. Lumma, S. G. J. Mochrie, and S. K. Sinha, *Surface dynamics of polymer films*, Phys. Rev. Lett. **90**, 068302 (2003).

[102] S. Narayanan, D. R. Lee, A. Hagman, X. Li, and J. Wang, *Particle dynamics in polymer-metal nanocomposite thin films on nanometer length scales*, Phys. Rev. Lett. **98**, 185506 (2007).

[103] R. Hempelmann, *Grundbegriffe, Polymerisationsreaktionen, Molekulargewichte*, in: *Physik der Polymere*, Vorlesungsmanuskripte des 22. IFF-Ferienkurses vom 25.2. bis 8.3.1991 im Forschungszentrum Jülich (1991).

[104] P. J. Flory, *Statistical mechanics of chain molecules*, Interscience, New York (1969).

[105] K. Sturm, *Konformationen*, in: *Physik der Polymere*, Vorlesungsmanuskripte des 22. IFF-Ferienkurses vom 25.2. bis 8.3.1991 im Forschungszentrum Jülich (1991).

[106] R. Weber, *Oberflächenempfindliche Röntgenstreuung an Polymer-Metall-Grenzflächen: Strukturelle Eigenschaften und thermisches Verhalten*, Ph.D. thesis, University Kiel (2002).

[107] J. Bandrup, E. H. Immergut, and E. A. Grulke (Eds.), *Polymer Handbook*, Wiley, New York (1999).

[108] H.-G. Elias, *An introduction to polymer science*, VCH, Weinheim (1997).

[109] L. J. Fetters, D. J. Lohse, S. T. Milner, and W. W. Graessley, *Packing length influence in linear polymer melts on the entanglement, critical, and reptation molecular weights*, Macromolecules **32**, 6847 (1999).

[110] M. A. Bouchiat and J. Meunier, *Light scattering from surface waves on carbon dioxide near the critical point*, Phys. Rev. Lett. **23**, 752 (1969).

[111] C. I. Poser and I. C. Sanchez, *Surface tension theory of pure liquids and polymer melts*, J. Coll. Int. Sci. **69**, 539 (1979).

[112] I. C. Sanchez, *Physics of polymer surfaces and interfaces*, Butterworth-Heinemann, Boston (1992).

[113] M. Volmer and A. Weber, *Keimbildung in übersättigten Gebilden*, Z. Phys. Chem. **119**, 277 (1926).

[114] G. J. Kovacs and P. S. Vincett, *Formation and thermodynamic stability of a novel class of useful materials: Close-packed monolayers of submicron monodisperse spheres just below a polymer surface*, J. Coll. Int. Sci. **90**, 335 (1982).

[115] G. J. Kovacs and P. S. Vincett, *Subsurface particulate film formation in softenable substrates: Present status and possible new applications*, Thin Solid Films **100**, 341 (1983).

[116] G. J. Kovacs and P. S. Vincett, *Subsurface particle monolayer and film formation in softenable substrates: Techniques and thermodynamic criteria*, Thin Solid Films **111**, 65 (1984).

[117] D. L. Lide (Ed.), *Handbook of chemistry and physics*, CRC Press, Boca Raton, 73rd Ed. (1992).

[118] F. M. Fowkes, *Attractive forces at interfaces*, Ind. Eng. Chem. **56**, 40 (1964).

[119] V. A. Parsegian and G. H. Weiss, *Spectroscopic parameters for computation of Van der Waals forces*, J. Coll. Int. Sci. **81**, 285 (1981).

[120] L. Ramos and L. Cipelletti, *Ultraslow dynamics and stress relaxation in the aging of a soft glassy system*, Phys. Rev. Lett. **87**, 245503 (2001).

[121] J.-P. Bouchaud and E. Pitard, *Anomalous dynamical light scattering in soft glassy gels*, Eur. Phys. J. E **6**, 231 (2001).

[122] D. Brockmann, L. Hufnagel, and T. Geisel, *The scaling laws of human travel*, Nature **439**, 462 (2006).

[123] Lévy flights: `http://classes.yale.edu/fractals/RandFrac/Levy/Levy.html`

[124] R. Nossal, S.-H. Chen, and C.-C. Lai, *Use of laser scattering for quantitative determinations of bacterial motility*, Opt. Commun. **4**, 35 (1971).

[125] J.-P. Bouchaud and A. Georges, *Anomalous diffusion in disordered media: Statistical mechanisms, models and physical applications*, Phys. Rep. **195**, 127 (1990).

[126] M. J. Capitan, D. Thiaudiere, L. Goirand, R. Taffut, and S. Lequien, *The ID01 beamline at the E.S.R.F.: The diffuse scattering technique applied to surface and interface studies*, Physica B **283**, 256 (2000).

[127] K. Wille, *Physik der Teilchenbeschleuniger und Synchrotronstrahlungsquellen*, Teubner, Stuttgart (2002).

[128] Beamline description ID01: `http://www.esrf.eu/UsersAndScience/Experiments/SurfaceScience/ID01/equipment.html`

[129] Beamline description ID10: `http://www.esrf.eu/UsersAndScience/Experiments/SCMatter/ID10A/BeamlineDescription`

[130] R. Weber, K.-M. Zimmermann, M. Tolan, J. Stettner, W. Press, O. H. Seeck, J. Erichsen, V. Zaporojtchenko, T. Strunskus, and F. Faupel, *X-ray reflectivity study on the surface and bulk glass transition of polystyrene*, Phys. Rev. E **64**, 061508 (2001).

[131] A. Thran, M. Kiene, V. Zaporojtchenko, and F. Faupel, *Condensation coefficients of Ag on polymers*, Phys. Rev. Lett. **82**, 1903 (1999).

[132] R. Smithson, D. McClure, and D. Evans, *Effects of polymer substrate surface energy on nucleation and growth of evaporated gold films*, Thin Solid Films **307**, 110 (1997).

[133] T. Strunskus, M. Kiene, R. Willecke, A. Thran, C. von Bechtolsheim, and F. Faupel, *Chemistry, diffusion and cluster formation at metal-polymer interfaces*, Mater. Corros. **49**, 180 (1998).

[134] R. Weber, I. Grotkopp, J. Stettner, M. Tolan, and W. Press, *Embedding of gold nanoclusters on polystyrene surfaces: Influence of the surface modification on the glass transition*, Macromolecules **36**, 9100 (2003).

[135] V. Zaporojtchenko, T. Strunskus, J. Erichsen, and F. Faupel, *Embedding of noble metal nanoclusters into polymers as a potential probe of the surface glass transition*, Macromolecules **34**, 1125 (2001).

[136] M. Krämer, *Struktur und Dynamik von Gold-Clustern auf dünnen Polymer-Filmen: Untersuchungen mit kohärenter Röntgenstrahlung*, Diploma thesis, University Dortmund (2003).

[137] H. Dosch, *Critical phenomena at surfaces and interfaces: Evanescent x-ray and neutron scattering*, Springer Tracts in Modern Physics Vol. 126, Springer, Berlin (1992).

[138] D. Lumma, L. B. Lurio, S. G. J. Mochrie, and M. Sutton, *Area detector based photon correlation in the regime of short data batches: Data reduction for dynamic x-ray scattering*, Rev. Sci. Instr. **71**, 3274 (2000).

[139] E. Helfand, *On inversion of the WilliamsWatts function for large relaxation times*, J. Chem. Phys. **78**, 1931 (1983).

[140] F. H. Stillinger, *Relaxation behavior in atomic and molecular glasses*, Phys. Rev. B **41**, 2409 (1990).

Publications

- S. Streit, M. Sprung, C. Gutt, and M. Tolan: "The surface roughness of water/glycerol mixtures investigated by x-ray reflectivity", Physica B **357**, 110-114 (2005).
- C. Sternemann, J. A. Soininen, M. Volmer, A. Hohl, G. Vank, S. Streit, and M. Tolan: "X-ray Raman scattering at the Si LII,III-edge of bulk amorphous SiO", Journal of Physics and Chemistry of Solids **66**, 2277-2280 (2005).
- S. Streit, C. Gutt, V. Chamard, A. Robert, M. Sprung, H. Sternemann, and M. Tolan, "Two dimensional dynamics of metal nanoparticles on the surface of thin polymer films studied with coherent x rays", Phys. Rev. Lett. **98**, 047801 (2007).
- S. Streit, C. Gutt, M. Paulus, and M. Tolan, "Glass transition at surfaces of polymer melts", submitted to Phys. Rev. Lett. (2007).
- F. Lehmkühler, M. Paulus, S. Streit, and M. Tolan, "Determination of microscopic interaction constants with unprecedented accuracy", submitted to Phys. Rev. Lett. (2007).

Acknowledgements

First of all I would like to thank my supervisor Prof. Dr. Metin Tolan for offering me the opportunity to work in his group and for his encouragement and expertise. Despite my distaste for drinking coffee and my affection for the French language, he still allowed me to finish my thesis. :-) I also thank Prof. Dr. Roland Böhmer for taking the time to act as a second referee for my thesis.

I would like to thank Christian Gutt for his extensive support and many invaluable discussions. Even though he has moved from Dortmund over San Diego to Hamburg during my thesis, I could always address him with any problems and questions that occurred during my work. Apart form Christian, Virginie Chamard and Aymeric Robert have supported me during the measurements at ID10A and helped with many useful discussions concerning the XPCS data analysis.

I am also indebted to Michael Sprung who was my tutor during my diploma thesis. Although he moved to Chicago at the beginning of my thesis, he also helped me with useful discussions. Henning Sternemann has developed together with him the very useful Matlab program for 2D XPCS data analysis.

I am very grateful to Michael Paulus, Virginie Chamard, Henning Sternemann, Christian Sternemann, Christian Gutt, and Thomas Nierobisch for the critical reading of (at least parts of) the manuscript. Furthermore, I would like to thank all other people from EIa which are not named explicitly here for the wonderful working atmosphere.

I thank Susanne Fricke and her staff members from the mechanical workshop for the skillful construction of the sample environments, and Klaus Widynski for the kindly provision of liquid nitrogen.

Special thanks go to Thomas Nierobisch for his love, support and understanding during the last time-consuming weeks of finishing this work. Also our cat Schmusi has tolerated my longer absences in the evening very patiently.

I would like to dedicate this thesis to my father Hagen Streit who had always supported me throughout my life and sadly cannot witness the completion of this work.